6-8-2018

Highly Ordered Titanium and Titanium Dioxide Nanotubes Electrode Development and Electrochemical Application

Xiang Li

R·I·T

Highly Ordered Titanium and Titanium Dioxide Nanotubes Electrode Development and Electrochemical Application

by

Xiang Li

A dissertation submitted in partial fulfillment of the requirements
for the degree of Doctorate of Philosophy in Microsystems Engineering

Microsystems Engineering Program
Kate Gleason College of Engineering

Rochester Institute of Technology
Rochester, New York
June 08, 2018

Highly Ordered Titanium and Titanium Dioxide Nanotubes Electrode Development and Electrochemical Application
by
Xiang Li

Committee Approval:

We, the undersigned committee members, certify that we have advised and/or supervised the candidate on the work described in this dissertation. We further certify that we have reviewed the dissertation manuscript and approve it in partial fulfillment of the requirements of the degree of Doctor of Philosophy in Microsystems Engineering.

____Patricia Taboada-Serrano_____08/25/2021_____
Patricia Taboada-Serrano Date
Associate Professor - RIT

____ Blanca Lapizco-Encinas _____08/25/2021_____
Blanca Lapizco-Encinas Date
Associate Professor - RIT

_____ Jiandi Wan _____08/25/2021_____
Jiandi Wan Date
Associate Professor - RIT

_____ Costas Tsouris _____08/25/2021_____
Costas Tsouris Date
Senior Research Scientists - ORNL

_____
Typed Committee member's name Date
Title

Certified by:

_____ Bruce Smith _____08/25/2021_____
Bruce Smith Date
Director, Microsystems Engineering Program

_____ Doreen Edwards _____08/25/2021_____
Doreen Edwards Date
Dean, Kate Gleason College of Engineering

ABSTRACT

Kate Gleason College of Engineering
Rochester Institute of Technology

Degree: Doctor of Philosophy **Program**: Microsystems Engineering

Authors Name: Xiang Li

Advisors Name: Dr. Patricia Taboada-Serrano

Dissertation Title: Highly Ordered Titanium and Titanium Dioxide Nanotubes Electrode Development and Electrochemical Application

Titanium dioxide (TiO_2) is one of the most extensively studied compounds in materials science. Since the first successful fabrication of highly ordered TiO_2 nanotubes (TiO_2-NTs) arrays via electrochemical anodization in '90s, thousands of publications have focused on the growth, properties, and applications of these versatile nanostructures. In the present study, anodization conditions were found to be the key determinants for TiO_2-NTs' structures and properties. In fact, this work demonstrates that tuning anodization conditions leads to tailoring TiO_2-NTs' for distinctive electrochemical applications.

Deconvoluting myriad factors, for example temperature, electrolyte, reaction time, and potential, which govern the anodized products properties, was possible by examining the correlation anodization parameters to TiO_2-NTs characteristics. In present study, a synergistic experimental approach was employed in order to investigate how anodization parameters affect the anodized products structures and properties. This work clearly delineates that the nanoscale geometry (tube diameter, surface area, and self-ordering degree) of TiO_2-NTs is highly tailorable by tuning the anodization parameters. Upon

achieving well-controlled TiO_2-NTs, they exhibited good electrosorption capacity and selectivity in the alkaline metal ions electrosorption test.

In addition, a novel strategy to fabricate hierarchically flow-through 3D Ti/TiO_2 NT electrodes for hydrogen evolution reaction (HER) was developed. The 3D Ti/TiO_2 NT electrodes reported here take advantage of 3D printing and *in-situ* anodization to achieve efficient HER electrocatalysis. Most importantly, the preparation of the 3D Ti/TiO_2 NT electrode is facile and readily scalable since the fabrication does not include time- and energy-consuming processes such as complex precursor preparation and high-temperature heat treatments. The large-scale construction of 3D Ti/TiO_2 NT does not require high capital cost and the flow-through feature makes it very appealing for continuous, industrial-scale hydrogen production. This study also provides evidence that the TiO_2 NT on the surface of the 3D Ti templates is the active catalytic surface promoting HER, by a two-step mechanism that contributes to the faster rate of the overall process. The 3D Ti templates contribute to fast HER reaction rates in terms of offering a seamless electron transfer network and large exposed active sites, namely TiO_2 NT.

ACKNOWLEDGMENTS

I am heartily thankful to my advisor Dr. Taboada-Serrano, who gives me the guidance and the opportunity to participate in the program and advises me in both theoretical and experimental fields. I would like to show my gratitude to my dissertation committee members, Dr. Lapizco-Encinas, Dr. Wan, and Dr. Tsouris, for their instructive suggestions and valuable comments on my thesis progressing. It is also a pleasure to express my appreciation to Dr. Richter and Dr. Weinstein for their generous support and insightful suggestions on my research. I would also like to thank Dr. Richard Mayes and Dr. Brian Dehoff from the Oak Ridge National Laboratory, who helped with 3 D printing and characterization, Mr. Richard Hailstone from the Chester F. Carlson Center for Imaging Science at Rochester Institute of Technology and Mr. Brian McIntyre from the Institute of Optics at the University of Rochester for their paramount skill and extensive support in electron microscopy technical support. I am also grateful to Paul Gregorius, Julie Olney, and Lisa Zimmerman for their continuous and reliable administrative support. I would also like to thank my lab mates Thomas Close, Samantha Pustulka, Scott Pedu, and Yali Zhang for their assistance and support to the project. I am deeply indebted to my parents, my wife Yuan Xue, my son Elliot Li, and friends for their help, support and understanding.

Lastly, I would like to acknowledge the financial support from the Kate Gleason Fund at Rochester Institute of Technology.

Table of Contents

Table of Figures

Table of Tables

CHAPTER 1 INTRODUCTION

1.1 Overview

Titanium dioxide (TiO_2) is one of the most extensively investigated materials, because it is low cost, chemically stable, environmentally friendly, and biocompatible. Consequently, TiO_2 has been widely used in paints, cosmetics, pigments and medical care products for many years.[1-9] Additionally, TiO_2 is also used in heterogeneous catalysis, as a photocatalyst in solar cells for hydrogen and electricity generation, and as corrosion-resistive and optical coating.[10] Depending on the type of and specific requirements of the applications, it is easy to tailor TiO_2 into desired geometries including thin film, nanoparticles, porous media, nanofibers and others.

In 1991, Iijima, a Japanese researcher, was the first to report the discovery of carbon nanotubes, which rapidly became a stunning research topic not only in nanotechnology but also in physics, chemistry, and material science.[11] Inspired by Iijima's groundbreaking findings, a range of transition metal oxides were synthesized into this one-dimensional or virtually one dimensional structures such as nanotubes, nanofibers, nanorods, and nanowires in the matter of a few years.[12-17] Among the transition metal oxides explored for fabrication of nanostructures, TiO_2 nanotubes (NTs) attracted immediate attention due to their low cost, good biocompatibility, and particularly due to their ability to be engineered into semiconductors with wide band gap. In fact, thousands of publications cover research topics involving the use on TiO_2 NTs from biomedical engineering to photo electronics applications. Over the past decades, the TiO_2 nanotubular architecture has resulted in over 100,000 publications, evidence of the immerse research efforts devoted to this field (Figure 1).[18] In general, TiO_2 NTs can be fabricated through different approaches; for example: hydrothermal reaction, template-assisted deposition, and anodic

electrochemical methods (anodization), among others. Based on Figure 1, there is a clearly increasing research interest on the synthesis of TiO_2 NTs via anodization. This fact is not surprising since anodization presents the following advantages over other synthesis methods: facile operation, energy-efficient procedures, well-defined tubular geometry, and even tailorable TiO_2 NT morphology and properties.

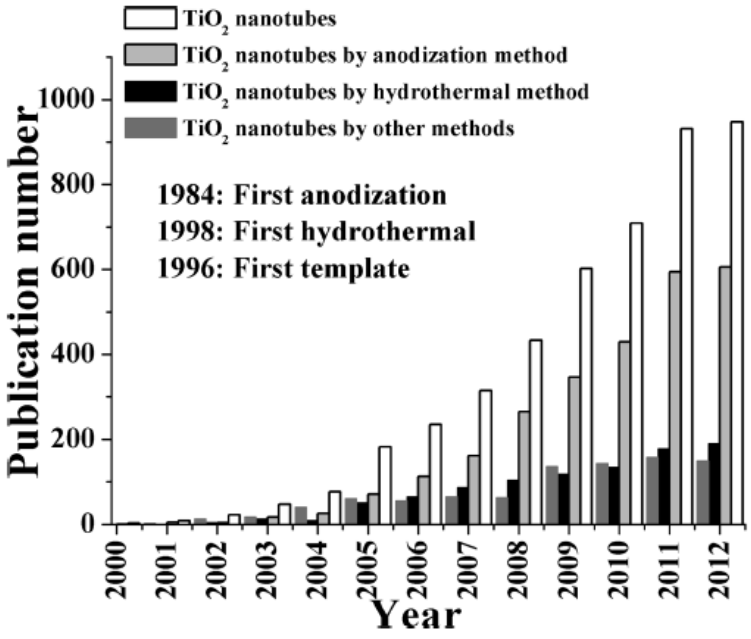

Figure 1 Number of published articles in the field of synthesis of TiO_2 nanotubes via different methods.[18]

1.2 Synthesis of TiO_2 nanotubes

As stated earlier, the synthesis of TiO_2 nanotubes (NTs) can be achieved through various approaches, including template-assisted deposition, hydrothermal reaction, electrospinning, and anodic electrochemical methods, namely, anodization.[19-24] A brief description of synthesis of TiO_2 NTs is presented below.

1.2.1 Template-assisted deposition

The first template-assisted deposition of TiO_2 NT dates back to 1996. An ordered alumina template was adapted for TiO_2 NT deposition by Hoyer.[25] Inspired by Hoyer's work, Kobayashi et al. employed organogelators as structure-directing agents for TiO_2 fabrication.[19] The organogelator, which was derived from cyclohexane, served as the template, resulting in TiO_2 NTs with outer and inner diameters of 150-600 and 50-300 nm, respectively[19]. Ku and coworkers successfully fabricated highly-ordered TiO_2 NT arrays through atomic layer deposition (ALD) with the help of a nanoporous silicon wafer template (mean pore diameter 53 nm and thickness 200 nm), Figure 2[26].

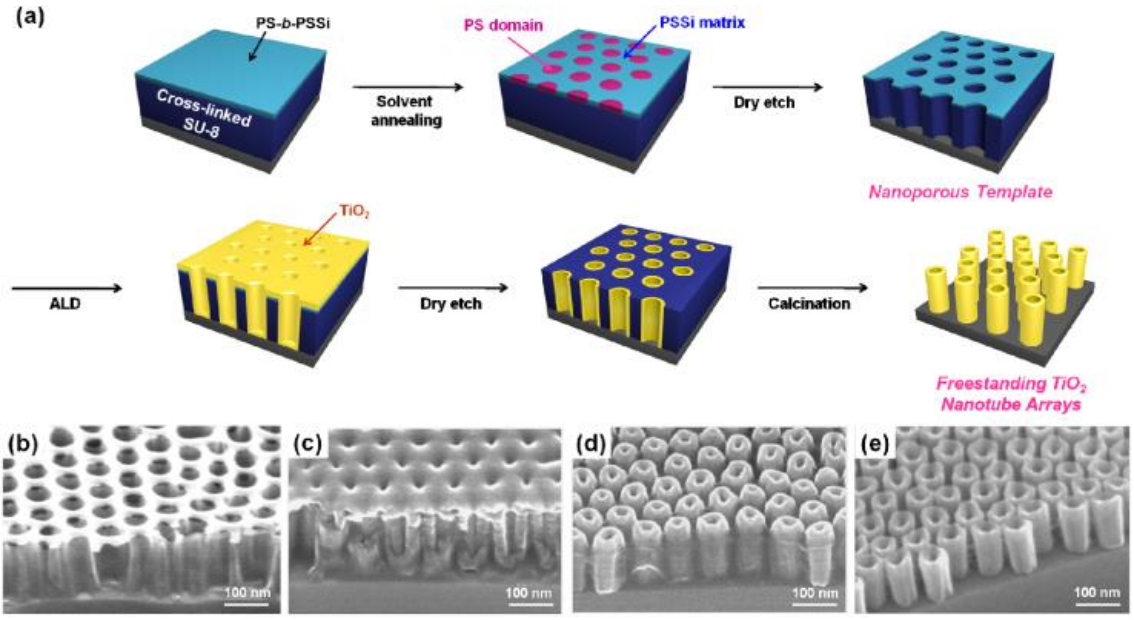

Figure 2(a) Schematics of the process to fabricate highly-ordered, freestanding TiO_2 nanotube arrays. Cross-sectional SEM images of (b) the nanoporous template with a mean pore diameter of 53 nm and a thickness of 200 nm, (c) after ALD of 20 nm-thick TiO_2 thin films on the nanoporous template, (d) followed by CF4 RIE to remove the overlayers on the top surface of the template, and (e) highly uniform and densely packed freestanding TiO_2 nanotube arrays with wall thickness of 20 nm after calcination to completely remove the organic template.[26]

The most typical template material for the deposition of TiO_2 NTs is porous anodic alumina oxide (AAO), which can be well regulated into a hexagonal pattern of nanopores

in a thick order.[27] To date, advances in AAO templates have led to well-defined self-standing porous AAO with pore distance 50-500 nm, with aspect ratios > 1000.[28, 29]

In addition to conventional electrodeposition methods, an alternative approach to synthesizing TiO_2 NTs with AAO templates is using polymer wetting. The idea is based on the fact that a low-surface-energy polymer solution is able to preferentially wet the inner walls of the pores of the AAO template, which have high surface energy. Consequently, an appropriate precursor containing Ti oxide and polymers can be used for fabricating TiO_2 NTs through AAO-pore wetting process followed by template removal.[30]

1.2.2 Hydrothermal reaction

Kasuga et al. synthesized TiO_2 NTs via the hydrothermal reaction for the first time in 1998.[21] In a typical hydrothermal reaction, a titanium oxide precursor is heated under a basic environment (for example NaOH solution) in an autoclave at temperature ranging from 100 to 180 °C during 24 hours to several days.[18] Usually, the TiO_2 NT fabricated via the hydrothermal approach featured multi-walled structures, open ends and inner diameters ranging from 2 to 20 nm. Nowadays, the mechanism of hydrothermal reaction for TiO_2 NT synthesis is still somewhat controversial[18]. Kasuga et al. believe that the nanotubes structures are formed during the washing process with the presence of hydrochloric acid (HCl)[18]. They proposed the following mechanism of nanotube formation: first, TiO_2 nanoparticles (precursor) react with sufficient sodium hydroxide to produce intermediate products such as, Ti-O-Na and Ti-OH. During the second step (washing), H^+ ions supplied by HCl exchange for Na in Ti-O-Na. Simultaneously, Ti-OH reacts with HCl and water to re-form Ti-O-Ti. After this step, nanosheet structures were observed and believed to have been produced via exfoliation[18]. Finally, the TiO_2 nanosheets would

convert into NTs structure by folding.[31] Other researchers proposed a similar mechanism based on experimentation that well aligned with the one presented by Kasuga and coworkers.[32]

Du et al. brought different findings to the table, which pointed towards the fact that TiO_2 NTs are formed hydrothermally without the involvement of the washing process.[33] Other researchers have found more evidence supporting Du's conclusion.[33-36] Wang et al. concluded that the as-prepared TiO_2 NTs were anatase rather than rutile and proposed the mechanism, depicted in Figure 3a-e. In Figure 3, NaOH initially disturbs the crystalline structure of raw anatase TiO_2 (Figure 3a), which may cause breakage of Ti-O-Ti bonding between the octahedra, the basic building blocks for anatase lattice (Figure 3b). The free octahedra reassemble into larger structures by sharing edges, with the formation of hydroxyl bridges between the Ti ions resulting in zigzag structures. The larger structures grow along the [100] direction of anatase (Figure 3c). Lateral growth occurs in the [001] direction and then results in the formation of two-dimensional crystalline sheets (Figure 3d). Afterward, in order to saturate the dangling bonds and reduce the surface energy, the crystalline sheets roll up into multi-layer nanotube structure (Figure 3e).[37] This mechanism is supported by the fact that multi-layer TiO_2 NTs structure is a common architecture for those produced through hydrothermal approach. It is also worth pointing out that the long reaction time is a significant drawback for this kind of method.

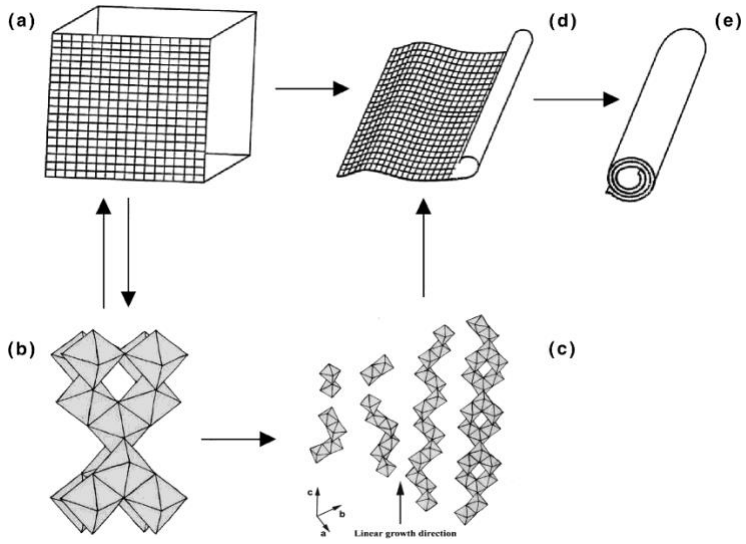

Figure 3 Schematic illustration of hydrothermal reaction for TiO_2 NT formation[37]

1.2.3 Electrospinning

In a typical electrospinning process, when a high voltage is applied, a thin jet of precursor solution is formed at the tip of a nozzle or syringe. The thin jet is then loaded onto a particular collector, usually organic nanofibers for nanotubular structures. After appropriate heat treatment, the organic nanofibers are removed or decomposed so that TiO_2 NTs are obtained. Figure 4 depicts the procedure and TiO_2 NTs obtained by Nakane and Ogata.[38] Nakane and Ogata first prepared pure Poly(vinyl alcohol) (PVA) nanofibers through electrospinning with an extrusion rate of 0.015 ml/min at 25 kV voltage to use as collector. Then, a precursor, consisting of titanium alkoxide [titanium tetraisopropoxide (TTIP)](10 wt.%)-ethanol solution, was deposited onto the PVA nanofibers by immersion for 10 minutes. After calcination, the PVA nanofibers were removed and the TiO_2 NT structure was revealed. The outer and inner diameters of the TiO_2 NT calcined at 500 °C for 5 hours corresponded to 440 nm and 270 nm, respectively.[38]

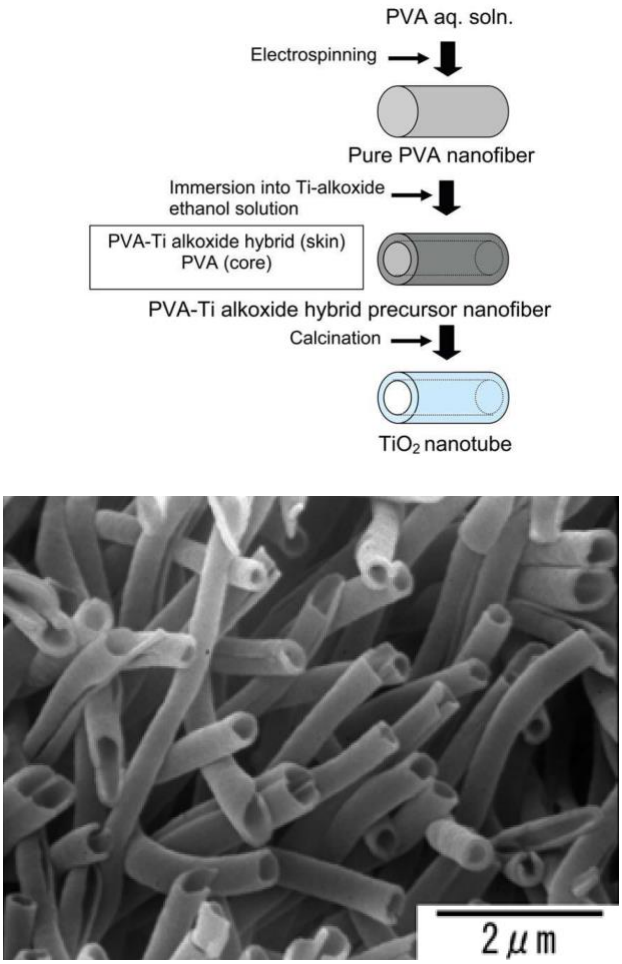

Figure 4 Schematic illustration of TiO_2 NT fabrication via elecrospinning.[38]

1.2.4 Anodic electrochemical methods (anodization)

Historically, anodization is an old process, which was first used a century ago in order to create an oxide layer on the surface of a metal substrate for protection against the environment. In the past decades, the anodization of a series of metals such as aluminum, magnesium, zinc, and titanium has been studied for different purposes.[39-42] In a typical anodization setup, shown in Figure 5, the target metal works as anode and an inert cathode, usually platinum or carbon, is employed. When a sufficiently high potential is applied to the anodization cell, the oxidation reaction is triggered and reaction (1) will take place on the target metal releasing metal ions. As a result, an oxide layer is formed on the surface

of the metal (reaction 2), while a fraction of the metal ions dissolves in the electrolyte (reaction 3). At the same time, protons are reduced to generate hydrogen gas at the cathode (reaction 4).

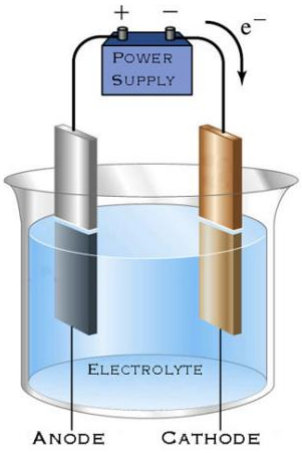

Figure 5 Anodization cell setup

$$M \rightarrow M^{n+} + ne^- \quad (1)$$

$$M + \frac{n}{2} H_2O \rightarrow MO_{n/2} + n\,H^+ + n\,e^- \quad (2)$$

$$M^{2+} + n\,H_2O \rightarrow M(OH)_n + n\,H^+ \quad (3)$$

$$n\,H^+ + n\,e^- \rightarrow \frac{n}{2} H_2 \quad (4)$$

In the case of anodization to synthesize TiO_2-NTs, fluoride ions (F^-) play an important role in the nanotubular structure formation. When present, F^- and H^+ will attack the oxide layer and produce the soluble $[TiF_6]^{2-}$ species (reaction 5 and 6, direct complexation of titanium ions and chemical dissolution of titanium oxide, respectively). Thus, when the rate of solvatization and rate of formation of oxide layer establish an equilibrium, one can

expect the growth of highly-ordered self-organized TiO_2 NT in the oxide layer, as shown in Figure 6.

$$Ti^{4+} + 6\,F^- \rightarrow [TiF_6]^{2-} \qquad (5)$$

$$TiO_2 + 6\,F^- \xrightarrow{H^+} [TiF_6]^{2-} + 2\,H_2O \qquad (6)$$

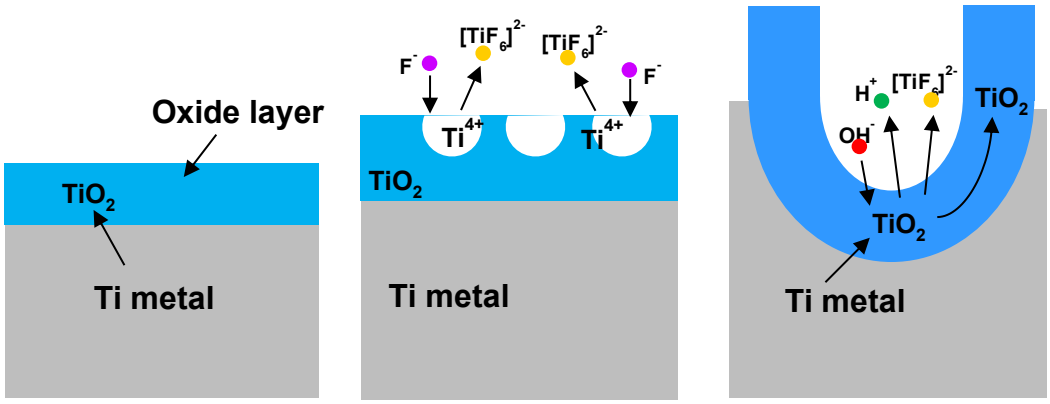

Figure 6 Schematic illustration of TiO_2 NT anodization with the presence of F- and H-.

1.3 Factors affecting the morphology and properties of anodized TiO_2 NTs

Various morphological products could be potentially achieved during anodization of Ti metal in fluoride-containing electrolytes such as porous films, nanofibers, and also nanotubes. The specific structure and properties of the anodized products significantly depend on a number of anodization factors including temperature, electrolyte formulation, and applied potential. Based on the mechanism of anodization for the formation of TiO_2 NTs discussed in section 1.2.4, water is a key component in the formation and even the morphology of TiO_2 NTs due to the two following reasons: (i), water is required for initiating the oxide reaction (reaction 2); (ii), water can accelerate the dissolution of oxide layer (reaction 3) as effective solvent for dissolution agents, for example, F^- (reaction 5 and 6).

It is believed that the electrolyte formulation (e.g., aqueous-based or organic-based solution, presence of halogen ions or other agents) plays a role in the specific shape of anodized products, as depicted in Figure 6. In aqueous electrolyte where the water is not only a precursor but also a solvent, the reported diameter of TiO_2 NT ranges from 10 nm to 100 nm with applied potentials from 1 to 25 V.[43, 44] In contrast to the aqueous electrolyte, it has been reported that the organic electrolytes show much lower chemical etching rates for the oxide layer.[18] As a result, the equilibrium between the oxide layer growth and dissolution rate is displaced towards oxide growth rather than dissolution (dominant with aqueous electrolyte) resulting in longer NTs. The length of TiO_2 NTs can reach ~100 μm with organic-based electrolyte instead of a few micrometers with aqueous electrolyte as reported in the literature.[45]

As the anodization time and chemical etching rate (determined by electrolyte formulations) define the length of TiO_2 NTs, the diameter of TiO_2 NTs is mostly controlled by anodization potential as reported in the literature.[46-48] Some typical TiO_2 NT diameters obtained with a series of electrolyte formulations as function of applied potential are shown in Figure 7. In general, the diameter of TiO_2 NTs increases linearly with increasing applied potential. Notably the slope of the voltage dependence varies significantly for different electrolyte formulations. The small diameters of TiO_2 NTs and low slope of the voltage dependence obtained for organic electrolytes can be ascribed to the low conductivity of the solution and the resulting IR-drop (electrical resistance) effects, which reduce the effective potential in anodization with organic electrolyte.

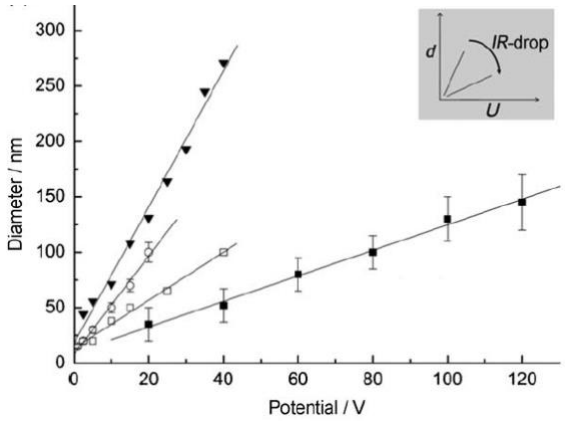

Figure 7 Potential dependence of TiO_2 NT diameter with various electrolyte (▼ glycerol/water 50:50[49], □ glycerol[43, 50], ■ ethylene glycol[50], ○ water[51]).

Apart from the TiO_2 NT length, the amount of water in the electrolyte is also an important determinant for other morphological features owing to the high conductivity and chemical etching rate resulting from higher ion-solubility. The first morphological characteristic of the TiO_2 NTs structure controlled via the addition of water are the degree of order and uniformity of the tubular structure. In fact, ordering and uniformity decrease with higher amount of water in the electrolyte. It has been suggested that the high chemical etching rates, achieved via contribution of water and F^- make the NT walls thinner and can even penetrate tube walls in electrolyte solutions with high water content. This fact is often evidenced by the formation of needle structures when executing anodization with water-based electrolytes. This so-called "nanograss" can block nanotube openings, therefore substantially changing TiO_2 NT's properties. In order to prevent the formation of nanograss and over etching, several methods have been reported. Some of these strategies include sacrificial layer coating, photoresist layers on substrate, and supercritical drying of the nanotubes.[52-54]

As mentioned above, the water content in the electrolyte reduces the degree of ordering regularity of the tubular shape of the TiO_2 NTs. In Figure 9, on can observe that

the nanotube structure of TiO_2 NT synthesized with organic electrolyte is defined much better than that of the TiO_2 NT synthesized with water-based electrolyte. Ring-like structures, also called "ripples", have been reported on the nanotube wall with aqueous electrolyte.[43, 49] The effects of ripples on TiO_2 NTs' properties is still unknown. Some researchers identified them as defects of nanotubes so that the ripple-free structure is preferred.[55] Controversially, some researchers believed that the ripples could be helpful for charge carrier trapping in the case of certain applications.[56]

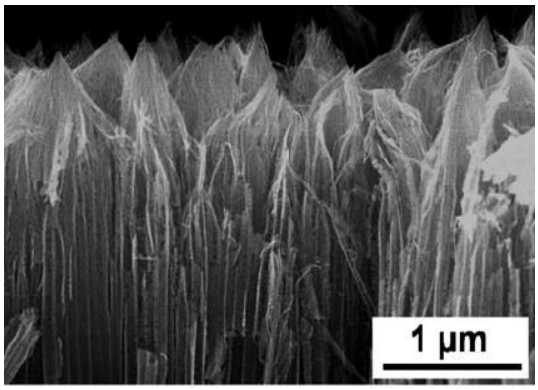

Figure 8 Over-etched TiO2 NT top with the "nanograss"

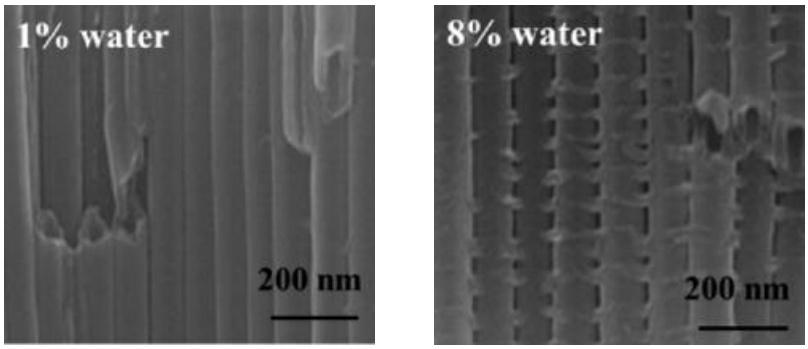

Figure 9 TiO_2 NT with smooth tube wall (left) and rippled tube wall (right).[57]

1.4 Application of TiO_2 NTs

1.4.1 Dye-sensitized solar cells

One of the most extensively studied applications of TiO_2 NTs is dye-sensitized solar cells. For the first time in 2005, Macak applied self-organized TiO_2 NTs to dye-

sensitized solar cells (DSSC) obtaining a low but promising energy conversion efficiency: 3.3% of incident photon to energy conversion efficiency in visible light and 0.036% of total energy conversion efficiency with the DSSC configuration.[57] Figure 10 depicts the working principle of a typical DCCS. When light induces the excitation (oxidation) of the photosensitized dye, the excited electrons are injected into the conduction band of the TiO_2 electrode. The excited electrons in the conduction band of the TiO_2 electrode then diffuse towards the back of the TiO_2 electrode, and finally move to the counter electrode through an external circuit, in which the current can be harvested. The oxidized dye molecules are reduced to ground state by the I^-/I_3^- redox mediator in the electrolyte within a very short time scale, usually within nano-seconds. The I_3^- travels back to counter electrode, where the I_3^- accepts the electrons from the external circuit to form I^-.

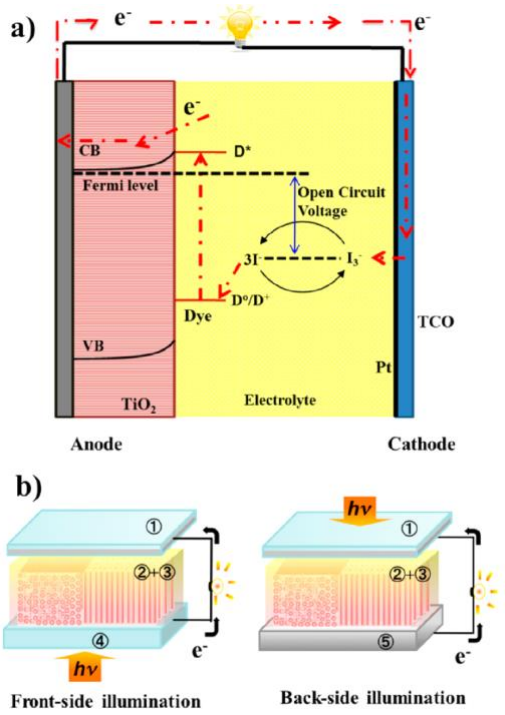

Figure 10 Schematic diagram of: (a) principle of a dye-sensitized solar cell; (b) different configuration using nanoparticle and nanotube layers, front-side illuminated (left) and back-side illuminated (right) (1, platinized fluorine doped tin oxide (FTO); 2, iodine electrolyte; 3, TiO_2 layer; 4, FTO substrate; and 5, Ti metal).[18]

The efficiency of TiO_2-NTs-based DSSC depends on the following three factors: (1), the energies of the highest occupied molecular orbital (HOMO) and the lowest unoccupied molecular orbital (LUMO); (2), the Fermi level of the TiO_2 electrode; and (3), the redox potential of the mediator in electrolyte. After Macak's pioneer work, hundreds of research papers have focused on the application of TiO_2 NTs to DSSCs in order to improve their energy conversion efficiency. The results thus far have demonstrated that smoother nanotube walls (i.e., ripple-free walls), high aspect ratio of TiO_2 NTs, crystal structure, and anode configuration are able to dramatically increase the DCCSs' performance.[43, 58-61]

1.4.2 Photocatalysis

So far, TiO_2 has been regarded as one of the most active photocatalysts. The intrinsic photosensitive, semiconductive nature of TiO_2, i.e., its ability to create electrons and holes when exposed to UV light, enables TiO_2 to work as photoelectrode and photocatalyst. Figure 11 explains the process of photocatalysis. When the TiO_2 electrode absorbs sufficient high energy from light ($h\nu > E_g$), electron/hole pairs are created in the TiO_2 conduction and valence band, respectively. Then, the electrons and holes react with electron acceptors and electron donors (A and D, in Figure 11, respectively), which are reduced and oxidized to form A^- and D^+. This redox reaction is the favorable photocatalytic reaction at these conditions. The electrons and holes can recombine or be trapped by the environment, which consumes electron/hole pairs and reduces the photocatalytic efficiency.

Many factors are believed to influence the photocatalytic activity of TiO_2 NTs including diameter, length, and crystallinity. Although crystallinity of TiO_2 NT electrodes can be changed without modifying the morphology of the electrode, it is very difficult to

vary TiO_2 NT length independently from NT diameter. Therefore, a lot of discrepant research results have been published regarding the effects of TiO_2 NTs' length and diameters on their photocatalytic activity. Agarwal et al. reported that, in acid orange 7 (AO7) photodegradation tests, higher photocatalytic activity was found to correlate with greater TiO_2 NT length up to 16 µm.[62] Observations by other researchers have supported these findings over the years.[63-66] However, a number of publications disagree with the conclusions above because they found that the photocatalytic activity decreased with TiO_2 NT length starting at 7 µm.[67, 68] In some cases, even no influence of NT length on photocatalytic activity was observed.[69]

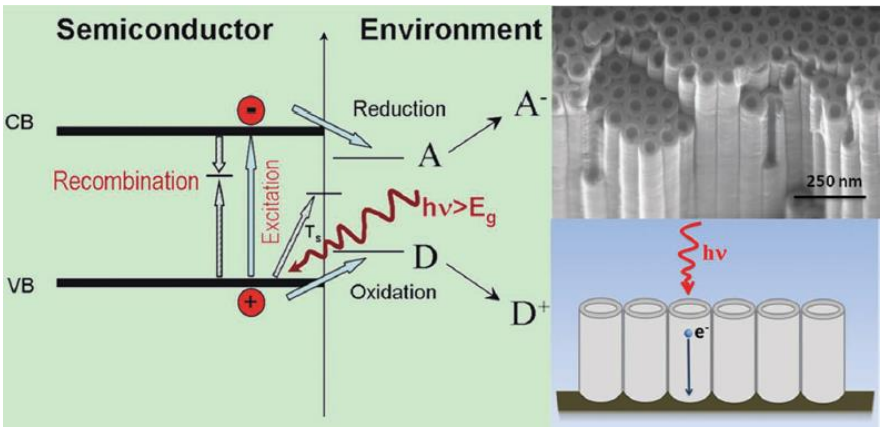

Figure 11 Schematic illustration of photocatalysis process at a TiO_2 NTs and electrolyte interface.[71]

As-prepared TiO_2 NT exhibits very low photocatalytic activity[70-72]. Annealing boosts the photocatalytic activity of TiO_2 NTs significantly as shown in Figure 12. During annealing, the as-prepared TiO_2 NT (amorphous) transforms to anatase at 300 °C and further to rutile when temperature is above 500 °C. The improvement of photocatalytic activity stems mainly from the higher conductivity of anatase and rutile compared to that of as-prepared TiO_2 NT.[73-75] It is also worth to point out that the light source used for

excitation should be taken into consideration when discussing TiO_2 NT crystallinity effects on photocatalysis.[76]

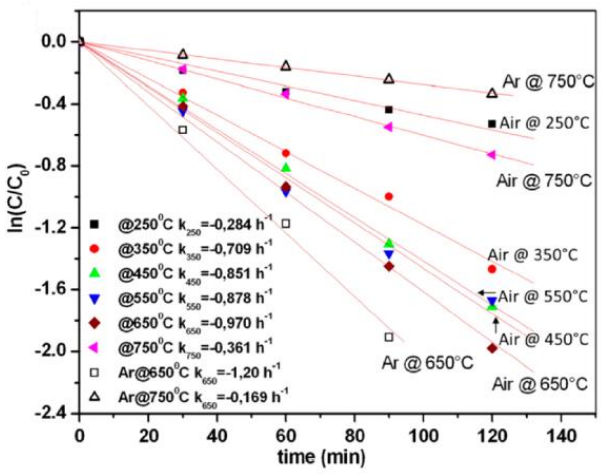

Figure 12 Annealing conditions effects on photocatalytic activity of TiO_2 NTs.[79]

1.4.3 Sensors

Another extensive application of TiO_2 NTs is quantitative and qualitative analysis due their good chemical stability, high temperature resistance, and semiconducting property. Dating back to 1983, Logothetis and Kaiser firstly used TiO_2 film in order to monitor and control the combustion process of internal combustion engines. The film used by Logothetis and Kaiser as a sensing system for optimizing the air-to-fuel ratio in the engine was fabricated via chemical vapor deposition (CVD).[77] Recently, Navale et al. employed TiO_2 nanoparticles for acetone sensing and the detection limit is able to achieve sub-ppm concentrations.[78] It is believed that the gas sensing mechanism for semiconductor oxide materials is based on the change in electric resistance with the presence of anatase. This change in electrical resistance is a result of adsorption/desorption and further interaction of target gas molecules at the surface of sensor.[79, 80]

At a working temperature of 270 °C, when TiO_2 sensors are exposed to air, oxygen will adsorb onto the surface by capturing the electrons from the conduction band of TiO_2 and forming an electron depletion layer, as shown in Figure 13. Herein, TiO_2 is an n-type semiconductor since the electrons are dominating carriers. When reducing acetone gets into contact with TiO_2 surface, the previously adsorbed oxygen will react with acetone molecules and release the trapped electrons back to the conduction band of TiO_2 causing an increasing of TiO_2 conductivity and shrinkage of the electron depletion layer. The acetone will then be consumed by converting into CO_2 and H_2O. When the acetone is completely turned into CO_2 and H_2O, the conductivity of TiO_2 will increase again due to electron capturing by the adsorbed oxygen.[78]

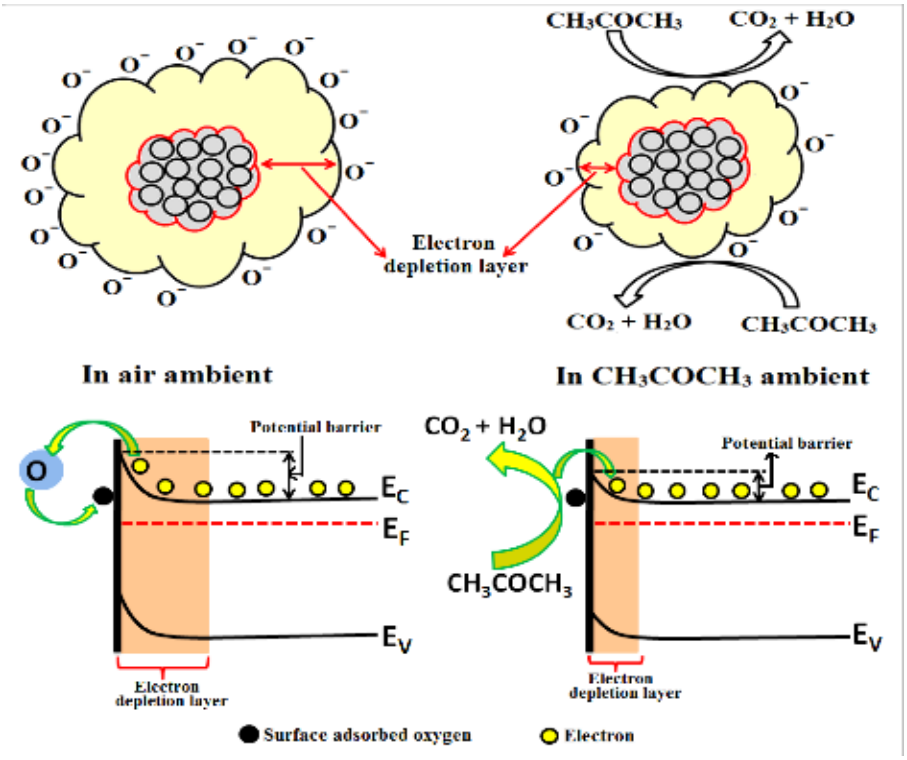

Figure 13 Schematic illustration of gas sensing mechanism of TiO_2 nanoparticles.[81]

1.5 Summary

TiO_2 is one of the most extensively studied compounds in materials science. Owing to its exceptional properties it has been used for instances in photocatalysis, dye-sensitized solar cells, and sensor applications. Over the past decades, a considerable number of various strategies to synthesize TiO_2 NTs have been researched, such as template-assisted methods, electrospinning, hydrothermal, etc. Among them, one simple, low-cost, and easy-operated approach is self-organizing anodization of titanium metal under specific electrochemical conditions. The anodization conditions are often the key determinants for the TiO_2-NTs' structures and properties. Due to its advantages, anodization was used as the method of choice to synthesize the electrodes and electrocatalysts in the present work in order to achieve the goal and objectives described in the next chapter.

CHAPTER 2 RESEARCH DESIGN AND OBJECTIVES

2.1 Problem identification

The general trend of applying TiO_2 NTs lies on their photosensitive and semi-conductive property, which has been extensively discussed in chapter 1. Nevertheless, another beauty of TiO_2 NTs, from the eyes of an electrochemical engineer, is their highly-ordered and tailorable morphological structure. The present research is motivated by the desire to expand the use of TiO_2 NTs to the new electrochemical applications, such as electrosorption and electrochemical hydrogen production, where TiO_2 NTs morphology and properties play a role; after all, TiO_2 NT is the key determinant that governs electrochemical performance.

TiO_2 NTs as a versatile nanomaterial enjoy a rapidly increasing interest. Various electrochemical process development, from charge storage (supercapacitors) to electrocatalysis (hydrogen production), require low-cost and tailorable electrodes that are yet to be identified and produced for real world, large scale applications. TiO_2 NTs electrodes are a good candidate to fulfill the above role due to the capability to control TiO_2 NTs' morphology and crystalline structure during fabrication. In this work, it was desirable to make active attempt to apply the TiO_2 NTs to the areas that remain untouched, for example, electrochemical hydrogen production.

2.2 Hypothesis

The hypothesis driving the present work is that "***the TiO_2 NTs morphology and crystalline structure can be finely controlled through tuning anodization parameters for example, temperature, electrolyte formulation, and applied potential, and consecutive annealing. And that tailoring of the structural conditions will lead to successful application of TiO2 NTs in electrochemical applications still unexplored for these***

materials". In that light, highly-ordered TiO_2 NTs with different well-defined pore diameters and crystalline structures are used as model electrode for studying the electrosorption, which will also be an first attempt to bridge the gap between molecular modeling prediction and experimentally measurement of electrosorption. Another exploration about novel electrochemical application of TiO_2 NT is to link it closer to catalytic hydrogen production. The fundamental principle of hydrogen production is to lower the voltage required by water electrolysis. In this work, the performance of a 3D flow-through TiO_2 NTs electrode by combining 3D printing and anodization is tested for hydrogen evolution. 3D printing embracing anodization may open the door of fabricating electrode for real world large scale application facile and cost-effectively.

2.3 Overall objectives

The ultimate goal of the study was to develop fully control on the fabrication of TiO_2 NTs so they could be tailored for various applications ranging from basic science to energy processes.

First of all, the methodology of synthesizing highly-ordered TiO_2 NTs was be investigated. Probing into the anodization parameters effects on the TiO_2 NTs morphology and crystalline structure is a core topic that is be thoroughly discussed. A series of TiO_2 NTs with different pore diameters and crystalline structures were fabricated and comprehensively characterized, which were then ready to be tested in further electrochemical experiments.

Upon the successful control of the morphology and properties of TiO_2 NTs, the second objective was to utilize these materials as a model system to investigate the effects on ion electrosorption in terms of TiO_2 NTs properties, ion strength, and ion-electrode

interactions. The effects of TiO_2 NTs anodization features on the mechanism of electrosorption will be a valuable reference for the basic engineering of several applications, in which electrosorption is the dominating electrochemical processes, including capacitive deionization and supercapacitors.

The third objective was to test the electrocatalytic activity of the anodized TiO_2 NTs towards electrochemical hydrogen production. It is expected that anodization technology is capable of providing a facile and scalable technology to synthesize, engineer, and optimize novel catalysts for renewable energy fuels. If successful, low cost, easy operation, high control, and good compatibility can prove the anodization to be a revolutionary catalysts fabrication pathway, which avoids the time and energy-consuming processes, such as doping and heat treatments, usually present in traditional catalysts industry.

CHAPTER 3 ANODIZATION OF TITANIUM DIOXIDE NANOTUBES

3.1 Motivation

Titanium dioxide (TiO_2) is one of the most extensively studied compounds in materials science. Owing to its exceptional properties, TiO_2 has been used in photocatalysis, dye-sensitized solar cells, and sensor applications primarily. Since the first successful fabrication of highly-ordered TiO_2 nanotubes (NTs) via electrochemical anodization in the 90s, this finding triggered thousands of publications dealing with growth, modification, and applications of these versatile 1-dimensional nanostructures.

As discussed in chapter 1, the morphology and structure of TiO_2 NTs fabricated via anodization is easily controlled by means of tuning the electrochemical conditions. Various anodization conditions, for example, electrolyte formulation, applied potentials, and temperature, will be thoroughly investigated in purpose of better managing the morphology and property of TiO_2 NTs. The NT regularity and diameter are two most important parameters that will influence the TiO_2 NTs performance in future electrochemical applications, such as electrosorption and catalysis. Additionally, crystalline structure is another important variable to consider when tailoring electrode to application. This variable will affect the electrochemical performance of the TiO_2-NT electrodes due to electrical conductivity of the material and molecular structure of the crystal.

In this chapter, we present the work performed to achieve the first objective described in Chapter 2. This objective involved attaining good control of the TiO_2 NTs regularity and diameter through optimization of anodization conditions. Temperature, ranging from 5 °C to 35 °C, potential, ranging from 45 V to 85 V, and two different electrolytes, aqueous and organic (ethylene glycol), were carefully tested as anodization parameters resulting in structural characteristics. Scanning electron microscope (SEM) was

employed in order to observe the morphology and carry out the measurements of NTs diameter and length. Additionally, crystalline structure transition was achieved via annealing the anodized samples while maintaining its morphological structure. The aim was to synthesize highly-ordered self-standing TiO_2 NTs with varying tube diameters and lengths in order to further explore the morphology and crystalline structure effects on their electrochemical application.

3.2 Background

3.2.1 Why is the tubular structure formed in TiO_2?

In 1999, the first self-organized TiO_2 NTs were produced through anodization in chromic acid and hydrofluoric acid electrolyte by Zwilling and coworkers.[24] The more important findings revealed by Zwilling group were the recognition of the addition of fluoride ions as the key determinant for the self-organized NT structure formation.

Typical anodization of TiO_2 NTs is usually carried out by applying a constant potential between 1-30 V in aqueous electrolyte and 5-150 V in organic electrolyte containing 0.05-0.5 mol/L (0.1-1 wt.%) fluoride ions. The time-dependent current behavior during anodization is a critical indicator of the various stages involved in TiO_2 NTs anodization, as shown in Figure 14.[81] It should be pointed out that in the absence of fluoride ions, a compact oxide (CO) layer would be obtained (depicted in dotted lines in Figure 14). However, in the presence of fluoride ions, a porous oxide (PO) structure can be obtained due to the itching ability of fluoride ions on the oxide layer.

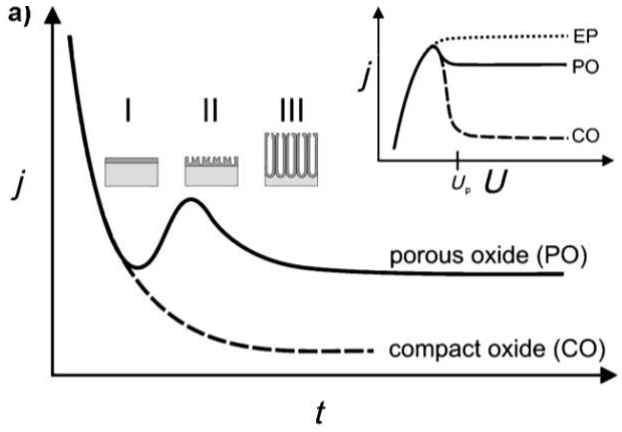

Figure 14 Representative current vs. time characteristics of constant voltage anodization with absence (----) and presence (—) of fluoride ions in electrolyte. (EP: electropolishing).[84]

Depending on fluoride concentration in the anodization solution, three different electrochemical characteristics can be identified (Figure 14 inset, which is a linear sweep voltammetry current vs. voltage curves). If the fluoride concentration is very low (≤ 0.05 wt.%), a CO layer will be formed during anodization. On the other hand, if the fluoride concentration is very high (>1 wt.%), most TiO_2 will react with sufficient fluoride ions to form soluble compounds into electrolyte. In this case, an electropolished Ti surface instead of an oxide film will be observed. In intermediate fluoride-ion concentrations, interesting structures can be found in the oxide layer.

When Ti anodization is performed with intermediate fluoride ion concentrations (0.5-1.0 wt.%), a competition between the oxide layer formation and dissolution takes place and as a result, a porous oxide film will be obtained. As discussed before, fluoride ion plays a key role in the formation of tubular structure. During anodization in the presence of fluoride ions, these small ions migrate several times faster than oxygen ions and thus aggregate at the interface of the metal and oxide layer forming locally, fluoride-rich spots., Within those fluoride-rich spots, dissolution of the oxide layer happens very easily compared to surrounding fluoride-ion-depleted areas. Due to the different dissolution rate

of the oxide in the fluoride-rich area (forming hollow tubing) and regular area (forming tube wall), the tubular structure is obtained on the oxide layer. Figure 15 illustrates the TiO_2 NTs formation during the anodization process at (i) 20 V in glycerol/0.35 mol/L NH_4F, depicted in Figure 15a; and (ii) glycerol/0.175 mol/L NH_4F, depicted in Figure 15b. [85] Figure 15 shows the progression of anodization via cross-sectional SEM images of oxide layer, with the upper section on the top and the lower section on the bottom.[82] The dashed line depicts the plane of the non-anodized Ti metal surface protected by photoresist-mask during anodization. On Figure 15, one can clearly see the fact that during anodization, the oxide layer grows along with the consumption of the substrate metal. With the presence of higher fluoride ions concentration, both oxide layer growth and metal consumption are accelerated.

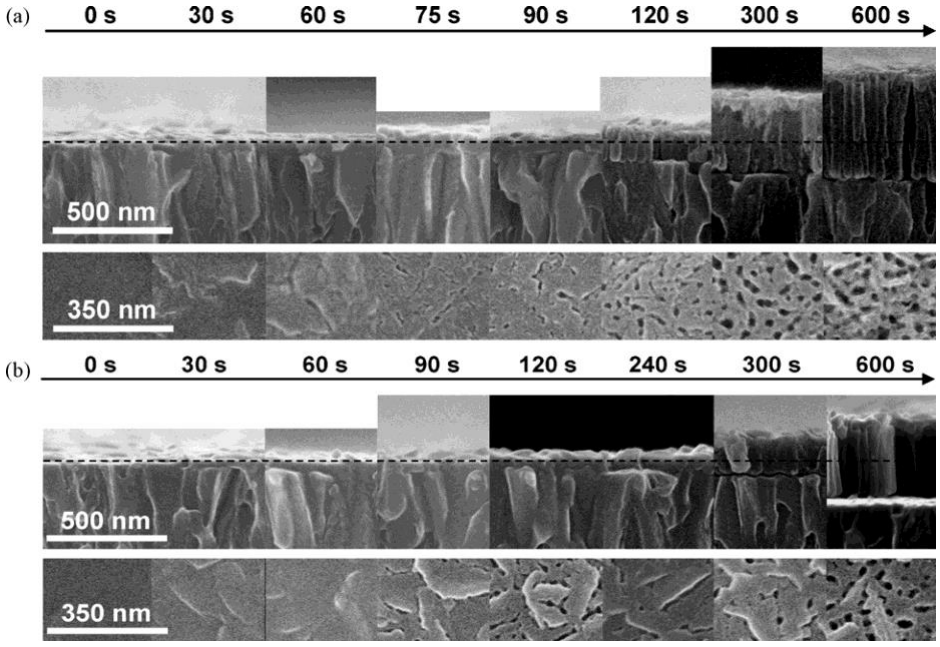

Figure 15 TiO_2 NTs growth at 20 V in glycerol/0.35 mol/L NH_4F (a), and glycerol/0.175 mol/L NH_4F (b).[85]

3.2.2 Ordering and crystalline structure of TiO_2 NTs

TiO_2 NT arrays produced via anodization can show ordering and regularity to different degrees. However, some specific applications, such as photonic crystals or high density magnetic storage media, require highly uniform TiO_2 NTs, especially in terms of pore diameter.[83, 84] In the present study, the TiO_2 NTs were used as a model system for electrosorption and then as electrocatalyst, therefore monodisperse distribution of the NT pore diameter was necessary. The intention to use some of the experimental electrosorption results obtained with the TiO_2 NT electrodes in this work towards validation of molecular simulation results required high control of regularity, diameter and other characteristics of the TiO_2 NTs. Such purpose can be achieved, to a large extent, by finely adjusting the anodization parameters including electrolyte formula, temperature, and applied potential. Generally, organic electrolyte is a better choice for producing higher degree of ordering among TiO_2 NTs than aqueous electrolyte. However, anodization cannot take place without the presence of water in organic electrolyte. On the other hand, a larger amount of water in the electrolyte usually leads to a lower degree of ordering of NT structure. This requires minimizing the water content while initializing anodization.

The anodic TiO_2 NTs are often amorphous. Annealing the amorphous NTs in air is a straight-forward approach to change the crystalline structure.[85-87] Typically, the crystalline structure conversion from amorphous to anatase starts at 280 °C.[88] Temperature increase beyond 500 °C triggers the onset of the rutile phase. Figure 16 depicts XRD spectra of the crystalline structure conversion at elevated annealing temperature.[18] Only 4% rutile structure was found after annealing at 500 °C for 12h.

When the temperature rises up to 900 °C, 100% rutile conversion rate is achieved after 2 hours of annealing.[81]

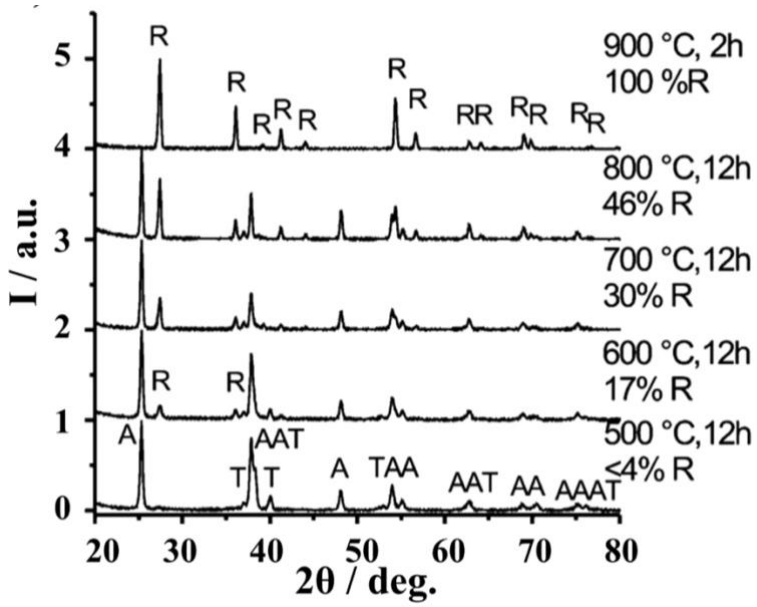

Figure 16 XRD spectra of TiO_2 NTs annealed at various temperatures (T: Ti metal, A: anatase, R: rutile).[18]

3.3 Experimental procedures and materials

3.3.1 Anodization of TiO_2 NTs

Titanium dioxide nanotube electrodes (TiO_2 NT) were fabricated following the method described in previous work.[89, 90] Pieces of titanium foil (purity 99.7%, from STREM Chemicals Inc. Newburyport, MA) were cut to the desired electrode size and rinsed with ethanol. In the case of the organic anodization bath, 150-mL solution of Ethylene Glycol and aqueous 0.05 mol/L ammonium fluoride with volume ratio of 50:1 was introduced into a temperature-controlled anodization cell under dry air in order to synthesize electrodes at different anodization conditions. In the case of the aqueous electrolyte, ammonium fluoride has been added in order to make the F^- concentration equal to 0.05 mol/L. Sulfuric acid will be used to adjust the pH value of electrolyte between 3

and 4. The pieces of foil were anodized at varying temperatures for 1 h in this solution with a platinum counter-electrode at fixed voltages of 45 V, 60V, ad 80 V. Temperature was one of the anodization parameters explored in order to define electrode-surface architecture. Highly-ordered and uniform cylindrical tubes were the desired electrode architecture for electrochemical studies.

Anodization experiments were carried out in a custom-built anodization cell equipped with a jacket, thermocouple, connections to a fluid-recirculation bath, and a custom-programmed temperature-control algorithm in LabVIEW. A TDK-Lambda ZUP 1203.6/U power supply and an Agilent Technologies Digital Multimeter 5 ½-Digit Display were connected to the anodization cell and controlled by a custom-developed LabVIEW code.

After anodization, the electrodes were removed from solution, rinsed with methanol, and allowed to air-dry. Four electrode samples were prepared simultaneously in order to ensure consistent characteristics. Some of the samples were annealed in air at 425 °C for 1 h in order to change the TiO_2 crystalline structure. The mass of the NTs was determined prior and after annealing by weighing, in order to detect any change in mass that might have occurred during annealing.

3.3.2 Characterization of TiO_2 NTs

Scanning electron microscopy (SEM, Zeiss Auriga CrossBeam SEM) was used to characterize the morphology of TiO_2-NT electrodes. The specific surface area was determined via statistical analysis of the dimensions of the nanotubes measured from SEM images taken at random locations on the electrodes synthesized for this work, in the same

fashion as previous work [28]. The mass of the nanotubes was determined via direct weighing.

3.4 Results and discussion

3.4.1 Morphology and crystalline structure of anodic TiO_2 NTs

Figures 17a and 17b show SEM images (top and side view) of one of the TiO_2 NT electrodes anodized with potential of 60 V for 1 hour at 15 °C. Regular nanotube structure with uniform diameters and lengths were obtained at these anodization conditions, which were subsequently used in electrochemical experiments. Statistical analysis of SEM images was used in order to determine the mean diameter and length for the TiO_2-NT electrodes prepared. Based on the measurement from the SEM images, it can be seen that the TiO_2 NT electrode has a diameter of 41.4 ± 4 nm, length of 2136 ± 50 nm and specific surface area of 31.4 ± 2.2 m^2/g. This level of control is highly desirable for electrosorption studies. However, it is also necessary to point out that surface architecture is highly sensitive to the anodization conditions. For instance, in Figure 17c, when anodization was carried out with the same anodization-bath formulation, applied potential and anodization time but at 5 °C, nano needle structures, instead of nanotubes, were obtained. This suggests that the low temperature may have changed the balance between the competitive oxidation reaction and oxide dissolution reaction taking place during Ti anodization in the presence of F-. Another example is provided in Figure 1d, in which the anodization conditions were the same, but the temperature was 35 °C. One can observe that the nanotube structure is less regular and defined than the one depicted on Figure 17a. This is because the high

temperature accelerates both the fluoride etching and oxide layer growth, resulting in the cluster-like nanotube bulk appearance and deconstruction of some nanotubes.

The TiO_2 NTs synthesized with two different formulations of electrolyte on identical Ti substrates showed significant variation in morphology. By comparing Figures 18 left and right, it is apparent that the morphological structures of ethylene-glycol-based TiO_2 NT (TiO_2 NT-EG) and water-based TiO_2 NT (TiO_2 NT-W) have some differences. Water is required for initiating the anodization; on the other hand, water will assist fluoride ions to etch off the oxide layer. Therefore, water content is the determinant of the degree of ordering with constant fluoride ion concentration. In Figure 18, with identical fluoride ion concentration 0.05 mol/L, the uniformity of the nanotube structure in the case of TiO_2 NT-EG is more obvious than that of the TiO_2 NT-W. This difference stems from the fact that the water-based anodization bath exhibits higher chemical etching rate for the oxides (namely, TiO_2 NT), than the organic-based electrolyte (ethylene glycol in the present study). The balance between the rates of oxide-layer formation and re-dissolution might be slightly off-set towards re-dissolution of the oxide layer, resulting in long, thin-walled nanotubes in the aqueous case. Meanwhile, limited charge transfer during the anodization process is observed due to low electrical conductivity of the ethylene-glycol-based anodization bath, a larger resistive current drop. As a result, the mass of TiO_2 NT-EG obtained during the same anodization time on the same Ti substrate was 38% of that of TiO_2 NT-W. Additionally, the oxide-layer re-dissolution rate was also lower, resulting in short, thick-walled nanotubes in the organic case. From the SEM images one can also infer that the TiO_2 NT-W is more densely packed on the surface of Ti substrates, suggesting a larger number of nanotubes than that of TiO_2 NT-EG, as shown in Figures 18.

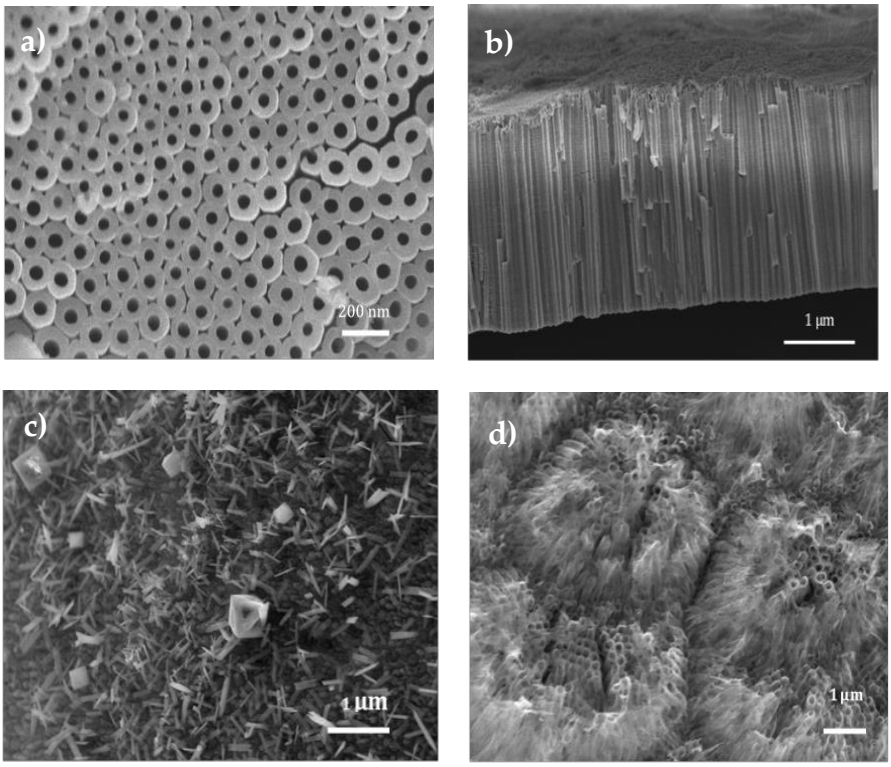

Figure 17 SEM images of TiO_2 NT electrodes (a), top view of TiO_2 NT anodized at 60 V 15 °C, annealed; (b) side view of TiO_2 NT anodized at 60 V 15 °C, annealed; (c) top view of TiO_2 NT anodized at 60 V 5 °C, non-annealed; (d) top view of TiO_2 NT anodized at 60 V 35 °C, non-annealed).

Electrodes of uniform TiO_2 NTs were prepared with temperature of 15 °C and an anodization time of one hour for subsequent electrochemical studies. Half of the electrodes were annealed in order to modify their crystalline structure without modifying their architecture. The annealed electrodes are identified as TiO_2-NT-A, and the non-annealed electrodes are identified as TiO_2-NT-NA hereafter. Based on previous discussion, the TiO_2-NT-A electrode should be anatase, instead of amorphous (TiO_2-NT-NA), which also holds higher electric conductivity than the latter.[70] It should note that the morphological structure of TiO_2 NTs will be well maintained during annealing although the crystalline

structure has indeed changed. The crystalline structure effect on TiO_2 NTs electrode electrochemical performance will be discussed more in Chapter 4.

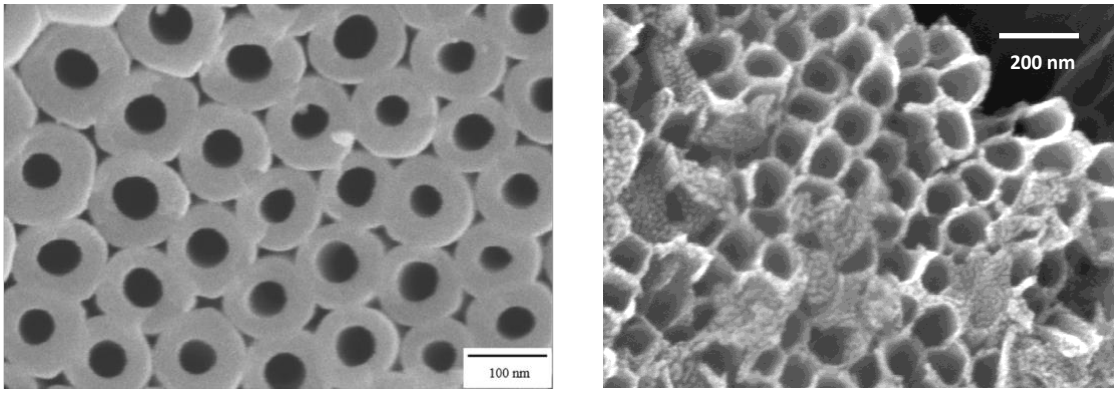

Figure 18 TiO_2 NTs anodized with 15 °C, 1h, 60 V, with ethylene glycol electrolyte (left) and aqueous electrolyte (right).

3.4.2 TiO_2 NTs pore size control

In section 3.4.1, we have confirmed anodization conditions that result in well-defined tubular structures. These conditions included a temperature of 15 °C, anodization time of 1 hour, and fluoride ion concentration equal to 0.05 mol/L in the form of NH_4F. With these parameters, when the applied potential was equal to 60 V, highly-ordered TiO_2 NTs with pore diameter of 41.4±4 nm were successfully prepared. These type of TiO_2 NT electrodes, were used model electrodes for electrosorption. The aim was to study the morphological, mainly NT pore size, effects on the electrochemical behavior of the electrode during electrosorption. In fact, a series of TiO_2 NTs with different pore sizes were synthesized by varying applied potential keeping the other conditions fixed in order to gain insighst into the application of these electrodes during electrosorption and comparing their behavior with results from molecular simulation.

Three different potentials, 45 V, 60 V, and 85 V, were selected for fabricating TiO_2 NT electrodes with different pore sizes. Table 1 summarizes the three pore diameters

targeted in this study, their respective pore lengths, their associated specific surface areas, and the nomenclature used to discuss the results. It must be noted that the specific surface area refers to the internal area of the tubular structure normalized with respect to mass of TiO_2 NT. Statistics for the pore diameters and lengths for all samples were extracted from multiple SEM images of different sections of the electrodes. These SEM images were also used to calculate an average nanotube-density per unit area of sample. The specific surface area was obtained by multiplying the average internal cylindrical area of the pores by the nanotube-density in the electrodes, and then normalizing by the mass of each electrode.

Table 1 Dimensions and specific surface areas for TiO_2 NT electrodes

Anodization potential	**45 V**	**60 V**	**85 V**
Diameter (D, nm)	36.8±3	41.4±4	44.9±6
Length (h, nm)	1671±32	2136±50	2263±89
Mass of nanotubes (mg)	0.0691	0.213	0.317
Specific surface area (m^2/g)	89.6±4.7	31.4±2.2	20.7±0.8
Nomenclature	NT-37	NT-41	NT-45

3.5 Conclusions

In this chapter, the anodization parameters including temperature, electrolyte formulas, and applied potential required to control and tailor the TiO_2 NT electrodes for the work were determined. The experimental results demonstrate that a highly-ordered TiO_2 NT electrode with pore diameter of 41 nm has been successfully produced at 15 °C, with ethylene glycol and 0.05 mol/L NH_4F, volume ratio 50:1, and applied potential of 60 V. Lower or higher temperatures will limit or disturb the NT structure formation due to thermodynamic reasons. Aqueous electrolyte favors the generation of TiO_2 NTs, larger

mass of TiO_2 NTs on the electrodes was generally observed, but it is negative to regularity and definition of the tubular structure.

Upon successful fabrication of well-defined TiO_2 NTs, further tuning of the applied potential was performed in order to develop TiO_2 NTs with different pore sizes. It was expected that the degree of ordering of TiO_2 NTs would have significant effect on their electrochemical performance, such as electrosorption and electrochemical hydrogen production. Based on the anodization conditions presented in this chapter, well-regulated TiO_2 NTs electrodes with pore size of 37 nm, 41 nm, and 45 nm were produced. The great uniformity of TiO_2 NTs, which was demonstrated by careful SEM examination, paved the way for studying how morphological structure of TiO_2 NTs influence on their electrochemical performance.

CHAPTER 4 ELECTROSORPTION OF MONOVALENT ALKALINE METAL IONS ONTO TITANIUM DIOXIDE NANOTUBES

4.1 Motivation

The separation and recovery of metal ions and ionic compounds from aqueous solutions is most challenging due to the stability of these charged species in aqueous environments. The possibility of exploiting physicochemical properties of ions and specific interactions with separation media to trigger electrosorption of selected ions was worthy of extensive study. Electrosorption is the accumulation of oppositely charged ions in the vicinity of a charged electrode in a liquid medium. This process governs the outcome of electrochemical reactions, charging/discharging of batteries, operation of supercapacitors and separation processes such as capacitive deionization (CDI) and electrodialysis.

The classical theory of electrosorption considers only ion charge and predicts that electrosorption capacity should increase proportionally with electrode surface area and applied electrical potential. Significant amount of molecular simulation work has been peformed over the past two decades in order to test the assumptions of the classical theory on electrosorption. However, up to now, experimental approach for electrode configuration and ion strength effect on electrosorption remains rudimentary. This is because the model electrodes for electrosorption studies have not been able to meet the requirement of consistency of electrode morphology and structure. In this chapter, highly-ordered TiO_2 NTs with three uniform pore sizes (37, 41 and 45 nm) were fabricated and used as model electrodes to study the interactive effects of pore diameter, applied potential and ion type on the electrosorption of three alkaline-metal cations (Li^+, Na^+, Cs^+). The model materials used were TiO_2 NTs, grown via anodization with well-defined diameters and lengths as discussed in Chapter 3. The model ions used were lithium, sodium, and cesium, in order to explore the physicochemical characteristics that could affect ion separation via

electrosorption, such as ion size and ion solvation strength. Two different crystalline structures for the titanium nanotubes were investigated: amorphous and anatase, achieved via annealing. Choronoamperometry and cyclic voltammetry experiments were employed to evaluate the electrosorption performance of the titanium dioxide nanatubes.

In contrast with classical theory predictions, electrosorption of ions was achieved not solely in response to electrostatic interactions between ions and electrode surface. Selective separation of ionic species bearing the same charge was achieved most likely via desolvation and specific ion-surface interactions triggered by the difference in crystalline structure of the titanium dioxide nanotubes electrodes used in this work.

4.2 Background

4.2.1 TiO_2 NTs as a model system for electrosorption

The properties of charged interfaces and the electrosorption of ions on charged surfaces have remarkable influence on the kinetics of various electrochemical processes, including those having technological importance such as water desalination and energy storage.[91-94] Electrosorption is a process where ions of opposite charge (counter-ions) are immobilized within a region known as the electrical double layer (EDL), which forms in the vicinity of the electrolyte-electrode interface when a low direct current potential is applied.[95, 96] Electrosorption takes place during electrochemical reactions, charging/discharging of batteries, operation of electrochemical capacitors (ECs) and capacitive deionization (CDI).[97, 98] Recently, CDI technology, which relies on the reversible removal of ions from solution by trapping them within the EDL, has gathered great interest due to its low energy cost, environmental friendliness, and no secondary

pollution.[99, 100] Electrochemical capacitors (ECs) use the electric field in the EDLs established at the electrode-electrolyte interface to store electrical energy. Without Faradaic (redox) reaction at EC electrodes, EDL energy storage mechanism makes fast energy uptake and delivery, and good power performance possible.[101, 102] Therefore, the properties of the EDL crucially determine the ions that can be removed from aqueous solutions in CDI and the energy that can be stored in ECs. Finally, the characteristics of the EDL directly influence the outcome of electrochemical reactions by adding another "resistance" or providing more "housing" for electrostatic charge storage to the processes.

Previous literature on electrosorption mainly focused on electrode development, and mostly for specific applications.[103-105] Porous carbons are often the choice of materials for electrosorption as they combine high surface area and good electrical conductivity.[106, 107] In spite of considerable efforts directed towards increasing surface area of carbon-based electrode materials in the last decades, CDI and ECs performance are still not at the required level in order to become competitive technologies. One of the factors contributing to this is the inaccessibility of surface area and the disordered pore arrangements of carbon materials that result in only part of the total surface area being utilized during electrosorption. Additionally, it was found that electrosorption capacity is dependent on the type of ion and its characteristics, e.g., hydrated-ion radius, charge and even specific interactions with the surface. These dependencies cannot be fully captured by the classical Theory usually employed to model CDI and EC performance. Chen and coworkers noted that during CDI operation with activated carbon electrodes at the same concentration, smaller ions depicted size-affinity by being preferentially captured by EDLs.[108] Furthermore, they claimed that in mixed Cl^- and NO_3^- solution, Cl^- is

preferably electrosorped over NO_3^-. This interesting observation suggests that specific interactions between ion and electrode indeed played a role in electrosorption process since the Cl^- and NO_3^- have similar hydrated radius (3.31 Å and 3.35 Å respectively), same concentration, and identical ionic charge in the test.[108] However, the current knowledge of this interaction is still rudimentary, and many experimental observations remain difficult to interpret because the property of carbon-based electrodes such as the architecture, composition, and pore size are difficult to control in order to perform a systematic study of these phenomena.

A model electrode with tunable properties is required in order to better understand the effects of electrode properties and their interactions with different ions on electrosorption. Electrodes with defined and tunable architectures, where pore sizes and pore lengths can be well defined would allow for systematic investigation of the effects of confinement and surface properties on the electrosorption of ions with specific characteristics [19,20]. Owing to well-defined pore diameters and lengths via anodization of titanium foil in specifically formulated chemical baths; highly-ordered and self-organized titanium dioxide nanotubes (TiO_2 NT) are a very appealing candidate for fulfilling this role [19,20]. A particular advantage of TiO_2 NT is that the crystalline structure is easily tuned by simply annealing between 350-450 °C in air (from amorphous to anatase), without modifying the electrode architecture. Anatase TiO_2 NT is a good approach to compensate for the low conductivity of amorphous TiO_2 NT while offering a potentially different ion-accommodation mechanism. Anatase TiO_2 contains a cavity in its crystalline structure where a small ion could insert itself [21]. In the present work, TiO_2 NTs were fabricated and tested for their suitability as model electrodes for electrosorption

studies. Electrosorption of three monovalent alkaline cations (Li^+, Na^+, Cs^+) was systematically explored in order to capture the interactive effects of crystalline structure and hydrated ion radius on electrosorption capacity, charge dynamics and utilization of electrode-surface area. The three ions chosen for the present work bear the same charge, but have distinctly different hydrated radiuses, which allowed us to investigate the effects of ion size during electrosorption. Additionally, the three ions selected are relevant in terms of applications: desalination, energy storage and deionization of radioactive waste. The goal of the study was to demonstrate the suitability of anodized TiO_2 NT electrodes to study how electrode properties and ion characteristics affect electrosorption.

4.2.2 Electrosorption of monovalent alkaline ions onto TiO_2 NTs: the morphological effect

The framework of the classical EDL Theory, which has been traditionally used to describe EDL structure and electrosorption, treats ions as point charges within a continuous electric field. This theory predicts that electrosorption capacity is directly proportional to the applied potential and solid/liquid interfacial area available for accumulation of charge, and that electrosorption capacity is mostly determined by ionic charge. However, this theory does not incorporate the effects of nanoscale confinement on the electrical double layer, nor does it account for other properties of the solution apart from ionic charge. The introduction of nanostructured electrodes to different types of electrochemical processes has brought into attention the fact that electrode architecture and level of confinement greatly influence process outcomes, and that classical theory fails to capture these effects in most cases [107, 109-119].

In electrocatalysis, increase in electrosorption and current density was expected due to the dramatic enlargement of surface areas achieved via the utilization of nanostructured electrodes, as predicted by classical theory [109, 110]. However, deviations from classical theory predictions and unexpected behavior of electro-catalytical activity suggest that the size of the ionic species involved in the reactions is a key parameter to consider in nanoporous catalysts, as it determines availability of reactants at the interface [109, 110]. In fact, although transport of ions into nanostructured electrodes plays a significant role in the availability of reactants at the surface, it has been largely hypothesized that electrostatics combined with size-exclusion effects are actually a more critical factor [109-112]. Unfortunately, the complex architecture of catalysts and electrodes used in electrochemistry, and the complexity of the processes taking place do not allow for a clear elucidation on how confinement might be affecting the availability of reactants of different ion sizes at the solid-liquid interface.

Literature on capacitive water desalination indicates that properties of porous carbon-based electrode materials, such as specific surface area and pore size, are key factors governing the performance of capacitive deionization and other hybrid electric-field-enabled separation technologies [113]. Biesheuvel et al. suggest that low desalination efficiencies may be tied to the pore-diameter of carbon materials during capacitive desalination [115]. It has also been hypothesized that the size of the hydrated ion may play a role in the efficacy of their removal from solution via electrosorption on different carbon-based materials [115-121]. Furthermore, it has been reported that pore size distribution seems to correlate with the preferential exclusion of ions during sorption in different types of carbon materials, including carbon aerogels, carbon nanotubes and others [122, 123].

Carbon materials such as activated carbon, carbon aerogel, and mesoporous carbon, which have been the focus of water desalination studies, have intricate electrode architectures with disordered pore arrangements, wide and even bimodal pore-size distributions, and inaccessible surface areas. These features make it very difficult to determine how a specific electrode property affects electrosorption capacity, and thus, desalination efficiencies [107, 113, 114].

Molecular simulations have been implemented in order to overcome the Classical Theory assumptions, and gain insights into the EDL structure at the molecular level that could explain the experimental phenomena observed in electrochemistry. Findings of these molecular modeling studies include ion-size-driven exclusion effects such as: (a) ordering of ions within the EDL by size rather than charge at low and moderate applied potentials, i.e., entropic effects dominating over energy effects; (b) co-ion exclusion effects from within charged slit-type pores; (c) charge inversion and others [120, 121, 124-127]. All these effects are expected to influence macroscopic EDL-properties like the amount of charge stored in the EDL and the concentration profiles of ions within the EDL. Despite considerable work on molecular modeling of EDL, no attempts have been made to directly compare experimental and molecular modeling results because of the lack of experimental tools that would allow to measure EDL structure at the atomistic level within nanostructures. Furthermore, the simplicity of the systems used in molecular modeling studies (slit-type nanopores) does not allow for direct comparison between modeling predictions of EDL structure with macroscopic-level electrochemistry experiments with nanostructured electrodes. Nanostructured electrodes usually have complex architectures that render a direct comparison to simple molecular modeling systems impossible.

The current work aimed to bridge the gap between molecular modeling and experimental data by using a model system (uniformly-sized, cylindrical nanotubes) close to molecular-modeling systems in order to test whether the occurrence of steric effects within the electrical double layer (EDL) structure inside confinement can affect measurable macroscopic quantities.

The model system was very well defined and tunable at the nanoscale in order to perform a systematic experimental study of the interactive effects of pore diameter, applied electrical potential and hydrated ion radius on the electrosorption equilibrium of three similarly charged ions with different hydrated-ion-radius. Titanium dioxide nanotubes (TiO_2 NT) were used as model electrodes in order to study the electrosorption of three monovalent alkaline cations (Li^+, Na^+, and Cs^+). Although the three ions chosen have the same charge, they have distinctly different hydrated radii, and this enables an investigation of the effect of ion size on electrosorption. Titanium dioxide nanotubes were selected as model electrodes for this work, because highly-ordered and self-organized titanium dioxide nanotube electrodes can be fabricated with well-defined pore diameters and lengths; this is accomplished via anodization of titanium foil in specifically formulated chemical baths [55, 128-131]. Nanotube diameter can be controlled during fabrication via tuning the anodization potential, and variations in nanotube spacing, order (uniformity and packing), and wall thickness are also possible via tuning other fabrication conditions [55, 128, 129, 131].

Molecular modeling predictions of EDL structure are mainly ion-concentration profiles within the EDL, i.e. amount of charge accumulated within the EDL. Since the work was an experimental, basic-science study of electrical double layer formation in

confinement that could be used for validation of molecular modeling results, electrical capacitance and electrosorption capacity, i.e, the amount of ions accumulated within the EDL at the solid-liquid interface, were obtained via chrono-amperometry (CA) and cyclic voltammetry (CV) in the present study. The premise for the choice of these electrochemical methods was to avoid experimental techniques that are highly dependent on the combination of parameters used in pre-selected models (e.g., equivalent circuits and others), which would defeat the purpose of generating little-processed data for validation of atomistic models used in molecular simulations.

4.3 Experimental procedures and materials

4.3.1 TiO_2 NT electrodes

TiO_2 NTs used for electrochemical tests were synthesized by anodization, which has been introduced in chapter 2. Highly-ordered TiO_2 with three pore diameters: 37 nm, 41 nm, and 45 nm (noted as NT-37, NT-41, and NT-45 respectively); and two crystalline structures amorphous and anatase (noted as NT-NA and NT-A, respectively) were systematically studied in order to identify morphological effects on electrosorption. This information can be used to define strategies to tailor the electrodes for electrosorption-related applications.

4.3.2 Electrochemical tests

All electrochemical tests in this work were performed using a BASi Cell stand C3 potentiostat, the counter electrode was a BASi MW-1032 platinum electrode, and the reference electrode was BASi Ag/AgCl (BASi MW-2052). The working electrodes were the TiO_2 NT prepared as detailed above. Electrochemical tests were performed with three

monovalent alkaline metal ions (Li^+, Na^+, Cs^+) as counter-ions and the same co-ion (Cl^-) in 20 ml of each of the following 0.1M solutions: Sodium Chloride (NaCl), Lithium Chloride (LiCl), and Cesium Chloride (CsCl). The area of the working electrode was 2 cm^2, corresponding to a mass of electrode (TiO_2 nanotubes and titanium foil) equal to 0.010 ± 0.001 g in all cases. The Ag/AgCl reference electrode and the platinum-wire counter electrode were placed in the solution along with the working electrode in a typical three-electrode set-up. The volume and concentration of the solutions were selected to ensure that ions were not depleted from the bulk solution at higher applied potentials. This was to avoid ion-concentration effects on electrosorption capacity. A blanking procedure was run before each electrochemical test, comprising a constant potential of +600mV vs Ag/AgCl being held for 5 minutes. This was done to ensure that each test had the same initial conditions. The potentiostat was programmed for each electrochemical test with the specifications described below.

One chronoamperometry cycle (CA) included two seconds of quiet time with no applied potential (0 mV), 130 seconds at a constant negative applied potential (charge) and 130 seconds at the same constant positive applied potential (discharge). The pairs of negative and positive applied potentials during charge and discharge were -200 mV/+200 mV; -400 mV/+400 mV; and -600 mV/+600 mV. Each CA cycle (quiet time, charge, and discharge) was repeated at least fifteen times with a blanking procedure between each cycle in order to target true equilibrium electrosorption capacity with the measurements.

In the electrochemical impedance spectroscopy (EIS) test, the three-electrode cell was set up in the same way as for the CA and CV tests. The EIS tests were conducted with a Gamry Reference 600 (Gamry Instruments, PA) with the amplitude of the sinusoidal AC

voltage signal of 5 mV over the frequency range 1 mHz to 1 kHz. Electrochemical impedance spectroscopy (EIS) spectra were analyzed with the Z-view software.

4.3.2 Electrosorption capacity

Electrosorption capacity was calculated assuming that each electron unit of charge was neutralized by one ionic charge. The accumulated charge was calculated via numerical integration of the area underneath the current response curve with time during the charging cycle. Values for electrosorption capacity were double-checked via calculation of the charge released during the discharge part of the cycle.

4.4 Results ad discussion

4.4.1 Effects of electrode crystalline structure and ionic strength on electrosorption

The effect of the TiO_2 NTs characteristic on electrosorption capacity was investigated in terms of its crystalline structure. As stated earlier, two groups of TiO_2 NTs: amorphous (non-annealed, TiO_2 NT-NA) and anatase (annealed, TiO_2 NT-A) were selected in order to study the effect of TiO_2 crystalline structure on electrosorption capacity of similarly-charged ions. Anatase TiO_2 NT electrodes are prepared via annealing the as-synthesized amorphous electrodes in air at 425 °C for 1 hour. The surface structure (TiO_2 NT diameter and length) of amorphous and anatase electrodes is identical, as it is not modified during annealing. Tighineanu et al. reported that the conductivity of anatase TiO_2 can be higher that of amorphous TiO_2 by several orders of magnitude.[132] Due to high conductivity, it was expected that the TiO_2 NT-A would lead to high charge densities at the surface of the electrodes, i.e., larger electrosorption capacities. Figure 19a and 19b depict electrosorption capacity for Cs^+, Na^+ and Li^+ for both TiO_2 NT-NA and TiO_2 NT-A

electrodes. In Figure 19a, TiO_2 NT-A electrode shows higher electrosorption capacity for each ion than that of TiO_2 NT-NA electrode, as expected. It is also shown that for TiO_2 NT-A, the highest electrosorption capacity, 29.78 μmol/m^2, was achieved during Cs^+ electrosorption at -600 mV. As for TiO_2 NT-NA, the highest electrosorption capacity was obtained for Cs^+ at -600 mV with a value equal to 12.19 μmol/m^2. This is only 40.9% of the highest electrosorption capacity of Cs^+ on TiO_2 NT-A at the same applied potential. Regardless of ion, the TiO_2 NT-A electrode substantially exhibited better electrosorption performance, which can be attributed to the higher conductivity of TiO_2-NT-A. Additionally, TiO_2-NT-A possesses a tunnel structure of anatase that may potentially aid electron transport and ion accommodation. It should be pointed out that, at a specific applied potential, the electrosorption capacity for various ions with both TiO_2 NT-A and TiO_2 NT-NA electrodes follows the order of $Li^+ < Na^+ < Cs^+$. For example, as seen in Figure 18b, with applied potential of -600 mV, electrosorption capacities of Li^+, Na^+, and Cs^+ with TiO_2 NT-A were 17.88, 24.79, and 29.77 μmol/m^2 respectively, while with TiO_2 NT-NA, the electrosorption capacities were 6.82, 8.91, and 12.19 μmol/m^2 for Li^+, Na^+, and Cs^+ respectively. This trend can be explained by the fact that smaller hydrated ions experience less steric hindrance towards packing within the EDL and may also experience stronger electrostatic forces. In fact, the trend in electrosorption capacity aligns with decreasing size of the hydration radii for Li^+, Na^+, and Cs^+ (which are equal to 3.82 Å, 3.58 Å, and 3.29 Å, respectively).[133] Furthermore, the comparative advantage of smaller hydrated ions towards electrosorption is more marked with TiO_2 NT-A electrodes. For instance, at -200 mV, the elecrosorption capacity of Cs^+ with TiO_2 NT-NA was 2.9 times higher than that the corresponding value to Li^+, whereas this value was equal to 6.1 in the

case of TiO_2 NT-A. The differences in electrosorption behavior did not limit themselves to capacity at equilibrium, but also in the dynamic behavior of the charging process (i.e., accumulation of charge within the EDL).

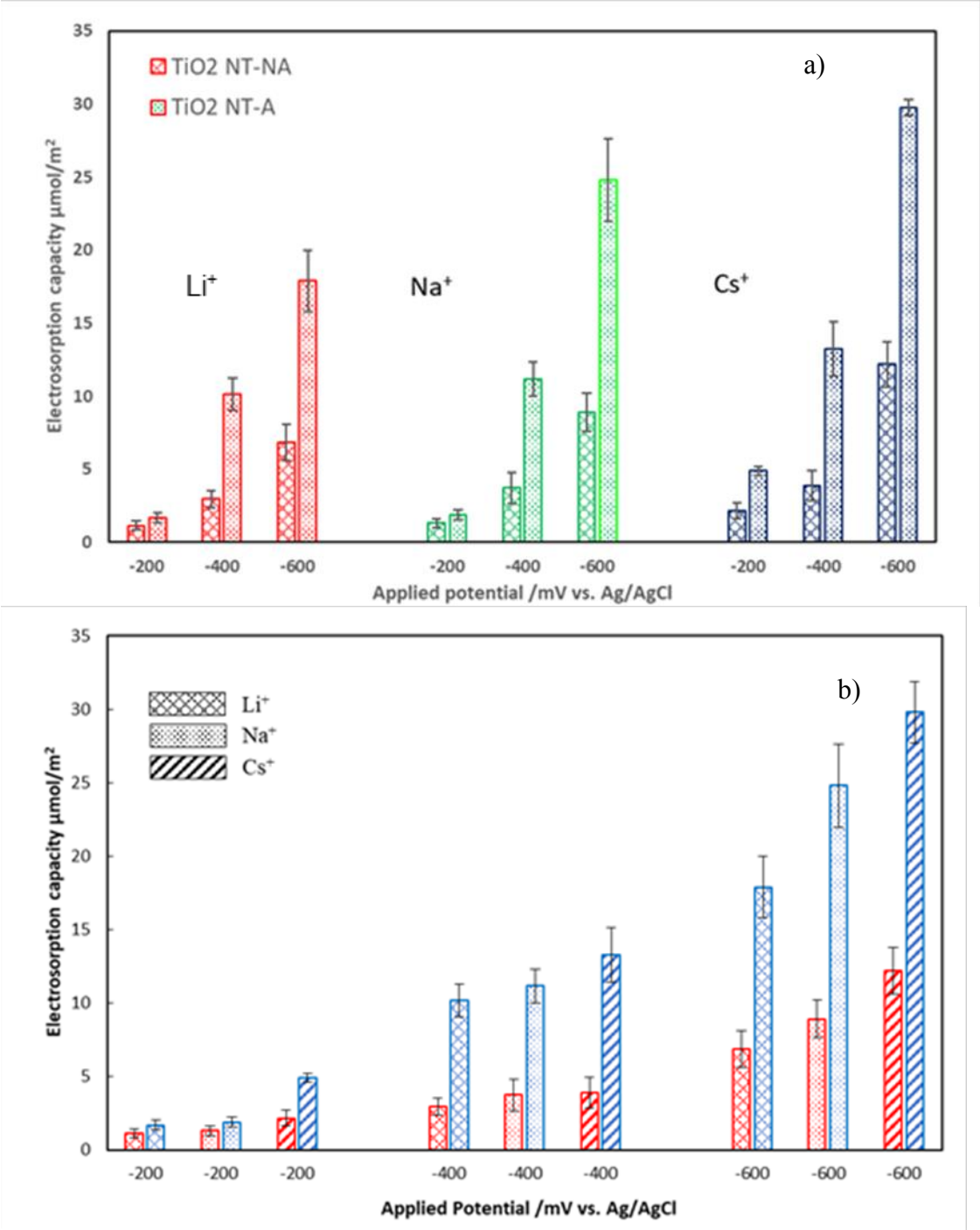

Figure 19 Electrosorption capacity of Li^+, Na^+, and Cs^+ (a) at various applied potentials; and (b) for different electrodes (red bars for TiO_2 NT-NA and blue bars for TiO_2 NT-A).

4.4.2 Charging dynamics dependence on ion and crystalline structure

Figure 20 a-c shows the dynamic behavior of EDL formation for TiO_2 NT-A and TiO_2 NT-NA under -200 mV, -400 mV, and -600 mV, respectively. When the applied potential was -200 mV, the highest charging rate was obtained with TiO_2 NT-A electrode and Cs^+ in Figure 20a. Furthermore, it is evident that the charging rates for TiO_2 NT-A were consistently higher than the rates obtained for TiO_2 NT-NA with all the ions studied in this work. Increasing applied potential does not only increase the charging rate, but also accentuates the difference between charging rates of anatase and amorphous TiO_2 NT electrodes. When the applied potential increased to -400 mV, it became more apparent of the advantage of TiO_2 NT-A in terms of charging rate. From Figure 20b, two groups of charging curves are clearly identifiable resulting from the differences in electrode crystalline structure. Figure 20c depicts even a more dispersed behavior of the curves of charging rate, with a clear advantage for TiO_2 NT-A. One should notice that the charging rate is consistent with the decreasing hydrated ion radii. As seen in Figure 20 a, b, and c, the charging rate followed the order of $Cs^+ > Na^+ > Li^+$ with both TiO_2 NT-A and TiO_2 NT-NA. Interestingly, the dispersion among charging curves brought about by the differences in hydrated-ion radii become more marked as applied potential increases.

Summarizing, (i) TiO_2 NT-A electrodes exhibited faster charging rates for each ion at every specific potential than that of TiO_2 NT-NA electrode due to the high conductivity of anatase; (ii) Cs+ with TiO_2 NT-A consistently exhibited the highest charging rates at each tested potential, followed by Na^+ and Li^+. This last finding confirms the fact that smaller hydrated ions have the advantage of less steric hindrance and most likely stronger electrostatic interactions during electrosorption.

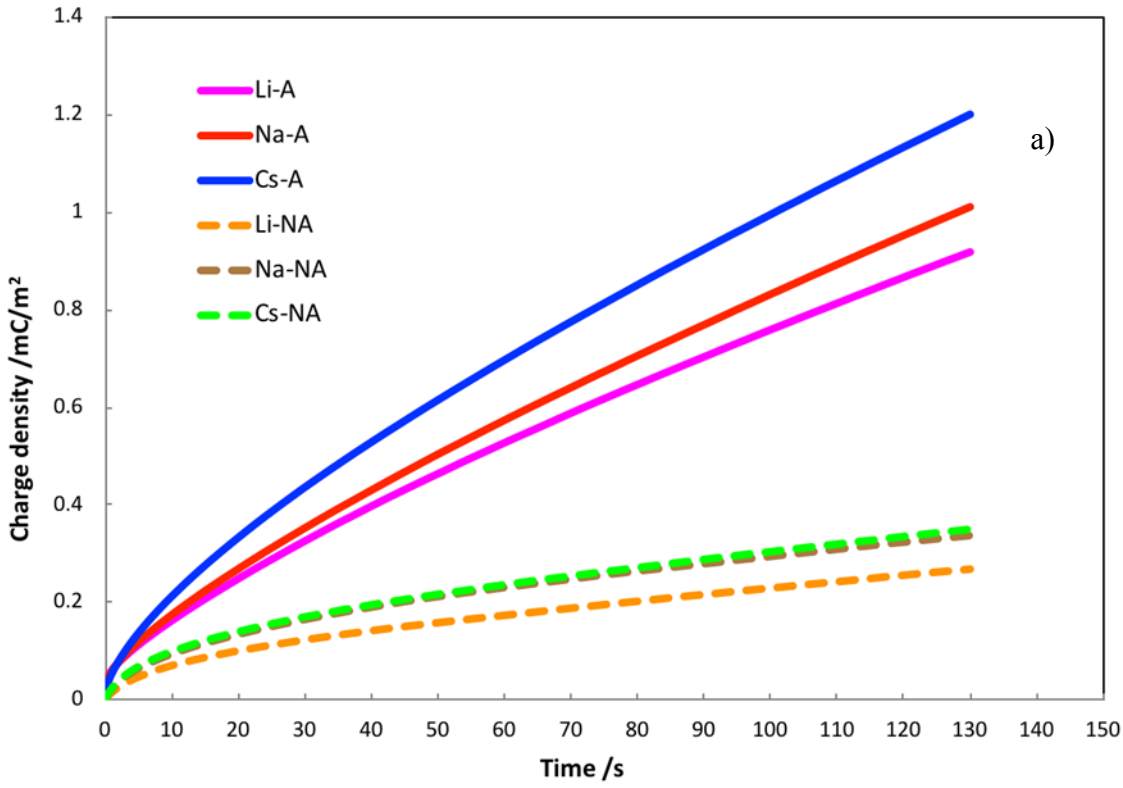
Li-A
Na-A
Cs-A
Li-NA
Na-NA
Cs-NA
Charge density /mC/m²
Time /s
a)

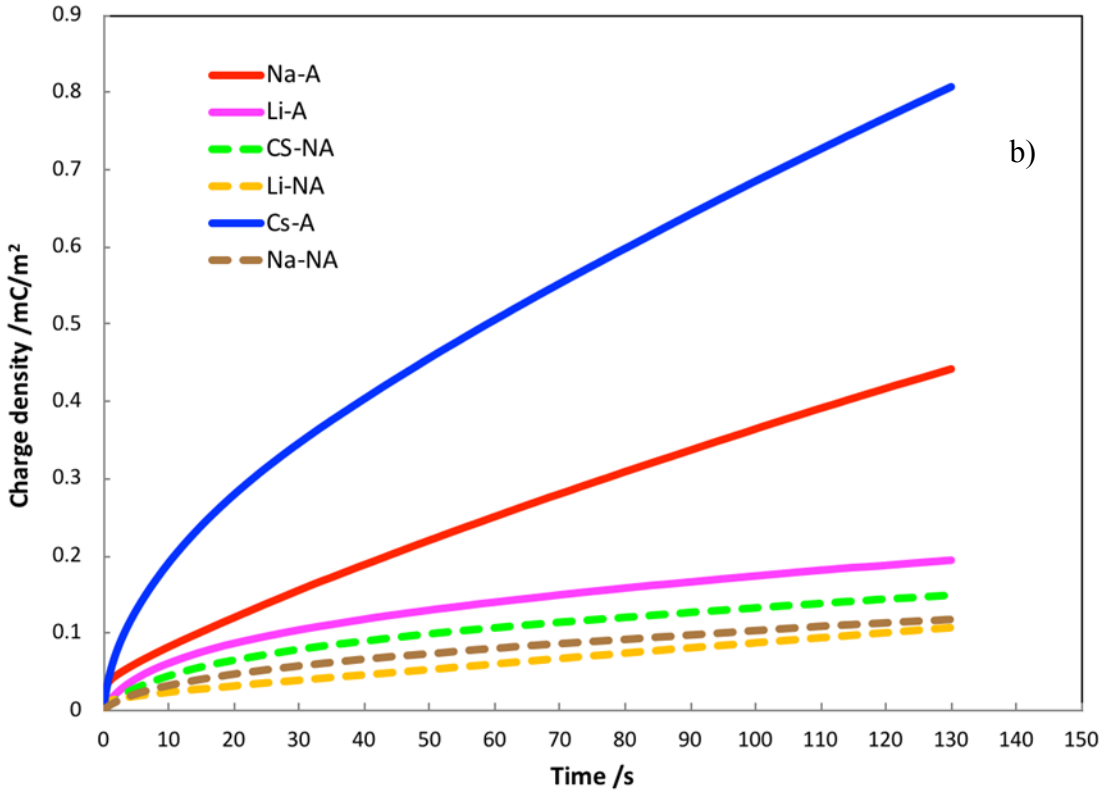
Na-A
Li-A
CS-NA
Li-NA
Cs-A
Na-NA
Charge density /mC/m²
Time /s
b)

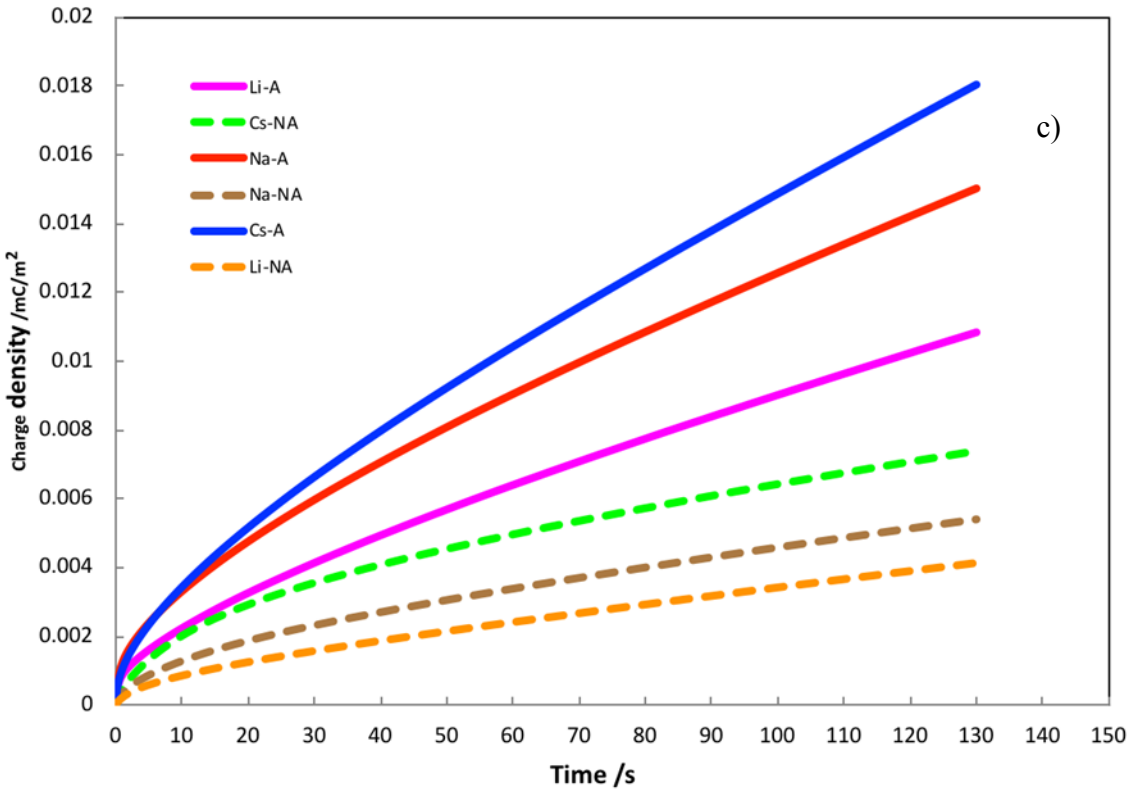

Figure 20 Charging rate of Li^+, Na^+, and Cs^+ with TiO_2-NT-A and TiO_2-NT-NA under (a) -600 mV vs. Ag/AgCl; (b) -400 mV vs. Ag/AgCl; and (c) -200 mV vs. Ag/AgCl (solid line for TiO_2-NT-A and dash line for TiO_2-NT-NA).

4.4.3 Electrochemically active surface area

It is not difficult to conclude that ion electrosorption benefits from the large surface area of TiO_2 NTs. The TiO_2 NT-A and TiO_2 NT-NA electrodes did not have any morphological difference, i.e., the surface structures on both electrodes were identical. Given the higher electrosorption capacity and charging rates exhibited by TiO_2 NT-A, it was necessary to determine how much of the total surface area of TiO_2 NTs is effectively used during electrosorption. Furthermore, it was necessary to explore how the TiO_2 NTs crystalline structure and any possible electrode-ion interactions may have influenced the effective area involved in electrosorption. Electrochemical active surface area (EASA) for each case was estimated based on cyclic voltammetry (CV) and electrochemical impedance

spectroscopy (EIS) measurements.[134-136] In order to obtain EDL capacitance via CV, a series of CV tests at multiple scan rates were carried out. The current in the non-Faradaic potential region measured via CV, which is assumed to be generated due to double-layer charging exclusively, is equal to the product of the scan rate, v, and the double-layer capacitance, C_{DL}, as given in equation 1.[136, 137]

$$i_{DL} = vC_{DL}, \qquad (1)$$

Examples of CVs of the TiO_2 NT-NA and TiO_2-A are depicted in Figure 21a and 21b. The CV tests were carried out in a non-Faradaic potential region at the following scan rates: 6, 12, 25, 50, and 100 mV/s. After acquiring the charging current at -0.3 V vs Ag/AgCl, the cathodic and anodic charging currents were plotted as a function of scan rate v, which yields a straight line with a slope equal to C_{DL}, as depicted in Figures 20c and 20d. The determined electrochemical double-layer capacitance of the system, C_{DL}, is the average of the absolute value of the slope of the straight lines regressed from the experimental data.

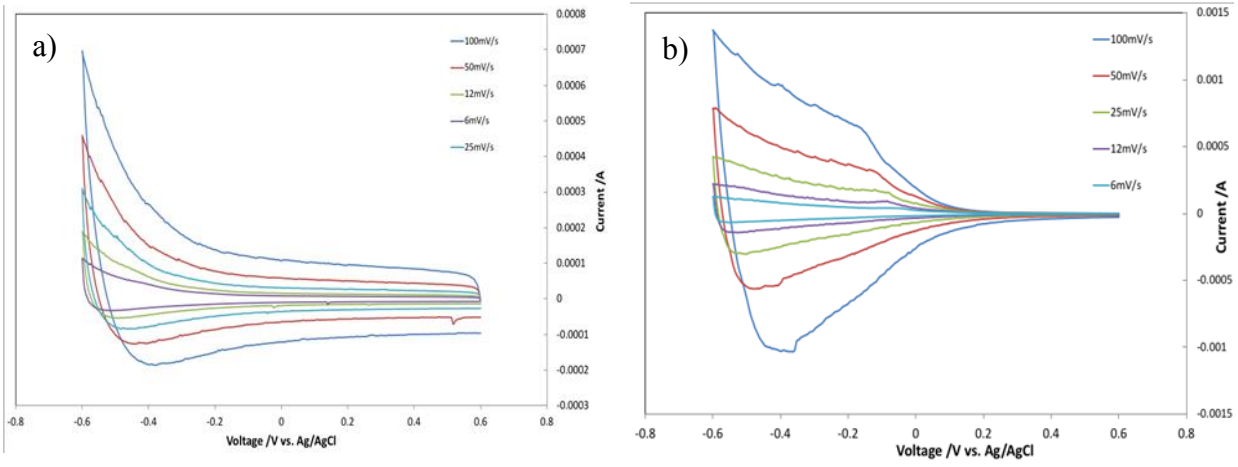

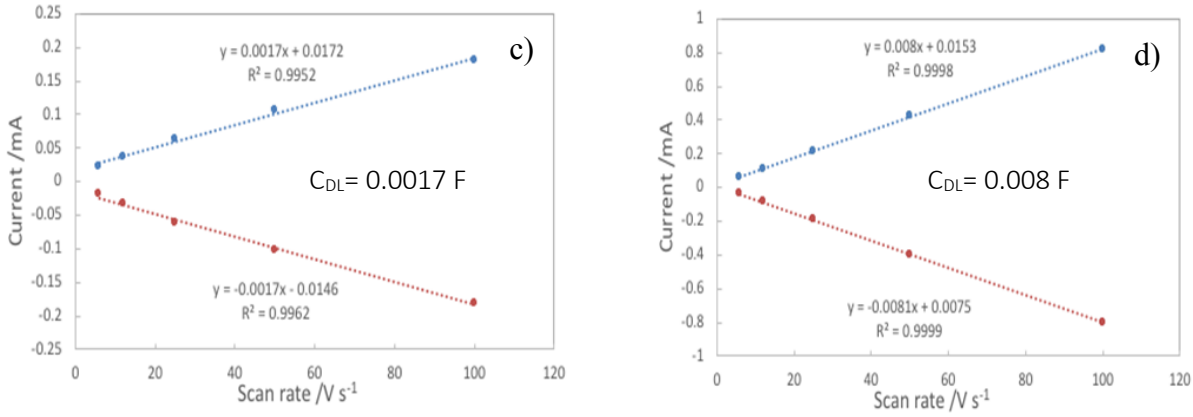

Figure 21 Cyclic voltammograms 1 M NaCl at various scan rates for (a) TiO_2 NT-NA; (b) TiO_2 NT-A; and EDL capacitance calculations for the determination of EASA; (c) TiO_2 NT-NA; (d) TiO_2 NT-A. For the determination of EDL capacitance, charging currents measured at

Upon having the double-layer capacitance, C_{DL}, the EASA of the sample was calculated according to equation 2:

$$EASA = \frac{C_{DL}}{C_s \cdot m}, \qquad (2)$$

Where m is the mass of TiO_2 NT, C_s is the specific capacitance of the sample and was calculated according to equation 3:

$$C_s = \frac{C}{A} = \frac{Q}{E \times A}, where\ Q = \int_0^t idt, \qquad (3)$$

where i is the time-dependent current response in CA test, t is the time of charge/discharge in CA test, E is the applied potential in the CA test, Q is the total transferred charge in CA test, and A is the area of the electrode.

The double-layer capacitance was independently determined via electrochemical impedance spectroscopy (EIS). Figure 22 a and b show the Nyquist plots of different ions for TiO_2 NT amorphous (NA) and anatase (A), respectively. The Nyquist plots are interpreted with the help of an equivalent circuit, shown in the inset of Figure 22, in which

the electrochemical system is approximated by the modified Randles circuit. The intersection of the impedance spectra with the real axis at the high frequency region end is the bulk resistance (R_s) including all contact resistance and resistance attributed to the electrolyte. The high frequency arc corresponds to the charge transfer limiting process and is ascribed to the charge transfer resistance (R_{ct}) at the contact interface between the electrode and electrolyte solution in parallel with a constant phase element (CPE) related to the double-layer capacitance. The frequency-dependent impedance of the CPE is given by equation 4[138, 139]:

$$Z_{CPE} = \frac{1}{Q_0 \cdot (i\omega)^{\alpha}}, \qquad (4)$$

Where Q_0 is a constant with dimensions F $s^{-(1-\alpha)}$, ω is the frequency of the sinusoidal applied potential, $i = (-1)^{1/2}$, and α is a dimensionless parameter, related to the phase angle of the frequency response, which has a value between 0 and 1. Based on the circuit model used here, the double-layer capacitance was calculated according to equation 5[138, 139]:

$$C_{DL} = Q^{\frac{1}{\alpha}} \cdot \left[\left(\frac{1}{R_s} + \frac{1}{R_{ct}}\right)\right]^{\left(1-\frac{1}{\alpha}\right)}, \qquad (5)$$

Note that when α = 1, the CPE behaves as a pure capacitor and C_{DL} = Q, and when α = 0, the CPE behaves as a pure resistor and C_{DL} is not detectable. For example, from the EIS measurement of the Li^+ with annealed TiO_2 NT electrode at applied potential of -0.05 V vs. Ag/AgCl shown in Figure 22, R_s = 24.4 Ω, R_{ct} = 10.3 Ω, Q = 0. 148 mF $s^{-(1-\alpha)}$, and α = 0.605. The calculated C_{DL} from eq. 5 is 0.012 F. The calculated R_{ct} for all experimental conditions are listed in Table 2.

Table 2 Electrochemically-active surface area (EASA) for TiO_2 NT-A and TiO_2 NT-NA determined via CV and EIS

Electrode	Target ion	R_{ct} / Ω	EASA-CV / m^2/g	EASA-EIS / m^2/g	EASA-CV/Specific Area / %	EASA-EIS/Specific Area / %
TiO_2 NT-A	Li^+	10.3	14.1	13.7	44.7	43.6
TiO_2 NT-NA	Li^+	13.9	21.1	20.6	67.1	65.7
TiO_2 NT-A	Na^+	7.6	12.3	11.7	39.3	37.7
TiO_2 NT-NA	Na^+	9.9	17.8	16.8	56.8	57.7
TiO_2 NT-A	Cs^+	3.1	8.9	9.2	27.6	29.7
TiO_2 NT-NA	Cs^+	6.2	16.2	15.9	51.5	50.4

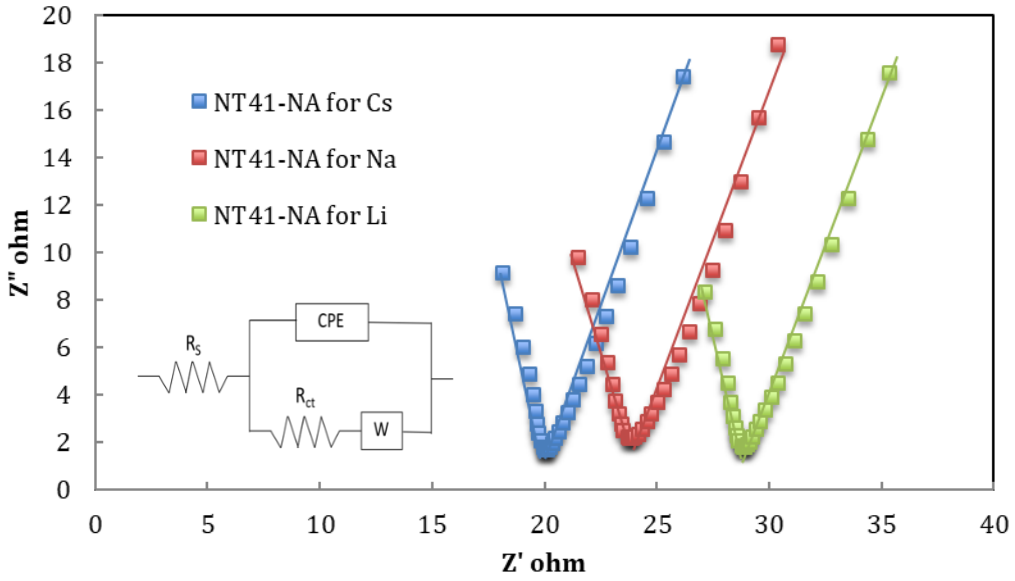

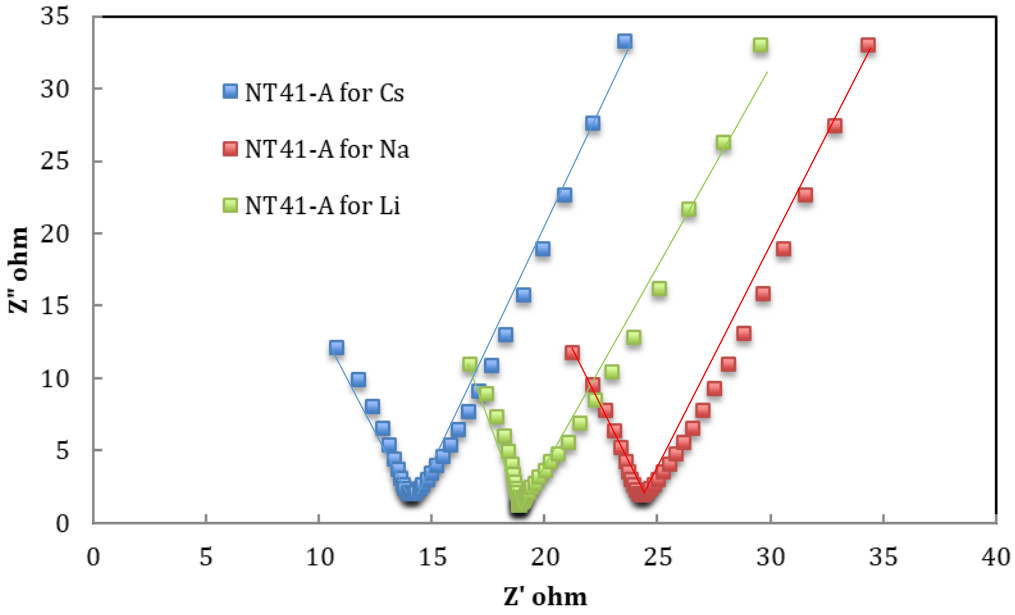

Figure 22 Nyquist plots for (a) TiO_2 NT-NA and (b) TiO_2 NT-A. The solid lines are the modeling fits to the EIS data by using the simplified Randles circuit shown in the inset of Figure 21a.

For a particular ion, the TiO_2 NT-A results in a lower charge transfer resistance (R_{ct}) than that of TiO_2 NT-NA as expected, due to the higher electrical conductivity of the anatase phase. Two components are expected to contribute to the charge transfer resistance in electrosorption. The first one is due to the process of ion diffusion from bulk electrolyte to the electrode surface. The second contributing factor is due to entrapment of ions within the EDL. The experimental conditions chosen for this work ensured that the ion concentration in the bulk electrolyte is much higher than the equilibrium concentration of electrosorption so that the resistance due to diffusion can be in principle neglected. Therefore, the charge transfer resistance can be equated to the resistance that an ion at the surface of electrode has to overcome in order to be immobilized within the EDL. The R_{ct} of different ions for both electrodes, TiO_2 NT-A and TiO_2 NT-NA, followed the trend of $Li^+ > Na^+ > Cs^+$, which is the reversed order of the hydrated ion radius as seen in Table 2. This finding confirmed our previous conclusion that the smaller hydrated-ion radii presented lower steric resistance and possibly stronger electrostatic interactions. In general,

the EDL capacitance measured by EIS is within 10% of that measured by the scan-rate dependent CVs, and the EASA obtained for a given sample by the two methodologies tend to agree within ±10%. Values of EASA were also correlated to hydrated-ion radius, but with reverse trend: the larges ion Li^+ exhibits the largest EASA, followed by Na^+ and then Cs^+. It seems that packing of larger ions within the EDL requires more surface area. The EASA of 21.1 m^2/g, which is found in the Li^+ electrosorption test with TiO_2 NT-NA, is the largest value reaching 67.1% of the total surface area, while the smallest EASA of 8.9 m^2/g, 27.6% of the total surface area, is found in the Cs^+ electrosorption test with TiO_2 NT-A.

Summarizing, anodized TiO_2 NT elctrodes of controlled surface structured proved to be a very effective model-electrode system in order to study experimentally ion-size effects and ion-electrode interaction effects during electrosorption.

The crystalline structure of TiO_2-NT electrode was a determinant factor of electrosorption capacity and charging rate for all ions studied in this work. Due to the high conductivity, the electrosorption capacity of anatase TiO_2-NT electrode outperformed that of amorphous TiO_2-NT electrode for all three targeted ions, Li^+, Na^+, and Cs^+ and tested potentials, -200 mV, -400 mV, and -600 mV. Additionally, the high conductivity of the anatase form of the TiO_2-NTs is favorable for fast EDL formation. As the surface architecture for all electrodes is identical, the only difference between annealed and non-annealed electrodes was in the crystalline structure. This mainly affects the electrical conductivity. However, a tunnel structure in the annealed (anatase) electrodes is not present in the non-annealed electrodes. This tunnel structure could potentially play a role as well.

The electrosorption tests evidenced that the hydrated ion radius plays a critical role during electrosorption. The electrosorption and charging rate of both anatase and

amorphous TiO_2-NT electrodes follows the same trend of $Li^+ < Na^+ < Cs^+$, which agrees with the order of decreasing hydrated ion radius Li^+ (3.82 Å) < Na^+ (3.58 Å) < Cs^+ (3.29 Å). The small ion can take advantage of low steric hindrance and higher relative electrostatic forces in order to be immobilized within the EDL more efficiently. This behavior becomes more marked with increasing applied potential. In fact, the lower charge transfer resistance is achieved by the combination of anatase TiO_2 electrode and ion with smaller hydrated radius.

Higher electrical conductivity translates into higher effective potentials at the solid-liquid interface of the electrodes, i.e., larger driving forces during EDL charging and formation. They also translate into larger surface charge densities to be neutralized via EDL, i.e., higher electrosorption capacities. If EDL charging and structure only responded to ionic strength (ion concentration and ionic charge), as predicted by Classical EDL Theory, no differences should have been detected for ions bearing the same charge at the same concentrations. This work confirms predictions of molecular modelling that EDL structure is determined by competitive energy and steric effects.[120, 121, 124, 140] This fact can also be visualized via the determination of EASE through independent electrochemical techniques.

The EASA based on cyclic voltammetry (CV) and EIS agree each other very well. The amorphous TiO_2-NA electrode exhibited higher EASA than that of anatase TiO_2-NT, which is contrary with the electrosorption capacity for any particular ion at same potential. It is noted that the amorphous TiO_2-NT utilized more surface area but reached lower electrosorption capacity. The EASA of anatase TiO_2-NT decreased with ion hydrated radius indicated that smaller hydrated ions are more easily packed within the EDL,

confirming the observations gained by measuring electrosorption capacity and charging rate. Furthermore, the lower EASA in the case of TiO_2-NT-A confirms the fact that these electrodes present lower surface charge densities due to their lower electrical conductivity. The order of increasing EASA with increasing hydrated-ion size ($Cs^+ > Na^+ > Li^+$) further confirms the occurrence of steric hindrance in the structure of the EDL.

4.4.4 Electrochemical double layer capacitance of TiO_2 NTs

The EDL capacitance for each TiO_2 NT under different test conditions was determined using two approaches: (1) by measuring non-Faradaic capacitive current associated with EDL charging from the scan-rate dependent CV tests; (2) by measuring the time-dependent current from the CA tests. Two processes are expected to contribute to electrosorption capacity. The first one is strictly due to EDL formation (EDL capacitance), which is expected to increase with applied potential and with interfacial surface area. The second contributing factor is known as "pseudocapacitance", and it arises due to Faradaic reactions at the interface. The applied potentials (±200 mV, ±300 mV, ±400 mV and ±500 mV vs. Ag/AgCl) explored in this work were outside of the range in which Faradaic reactions were expected to occur.

In order to obtain EDL capacitance via CV, a series of CV tests at multiple scan rates were carried out. The current response due to EDL charging measured during CV tests is equal to the product of scan rate, ν, and EDL capacitance, $C_{DL\text{-}CV}$, given by equation 6.

$$i = \nu \cdot C_{DL-CV} \qquad (6)$$

An example of a cyclic voltammogram for Li^+ with TiO_2 NT-41 electrode is shown in Figure 23a (the CV curves for other samples are provided in supplementary information).

The CV curves did not contain any Faradic peaks for all electrodes, ions, and potential ranges studied in this work. The CV tests were carried out in a non-Faradaic potential region at the following scan rates: 6, 12, 25, 50, and 100 mV/s. After acquiring the charging current at -200 mV vs Ag/AgCl, the cathodic and anodic charging currents were plotted as a function of scan rates v, which yielded a straight line with a slope equal to $C_{DL\text{-}CV}$ (Figure 23b). The double-layer capacitance of the system, $C_{DL\text{-}CV}$, was determined via averaging the absolute values of the slopes given by the liner regression of experimental data from positive and negative sweeps in the CV. The EDL capacitance measured from the scan-rate dependent CVs for the TiO_2 NT-41 electrode with 0.1 M LiCl at -200 mV is: $C_{DL\text{-}CV}$=3.2 mF.

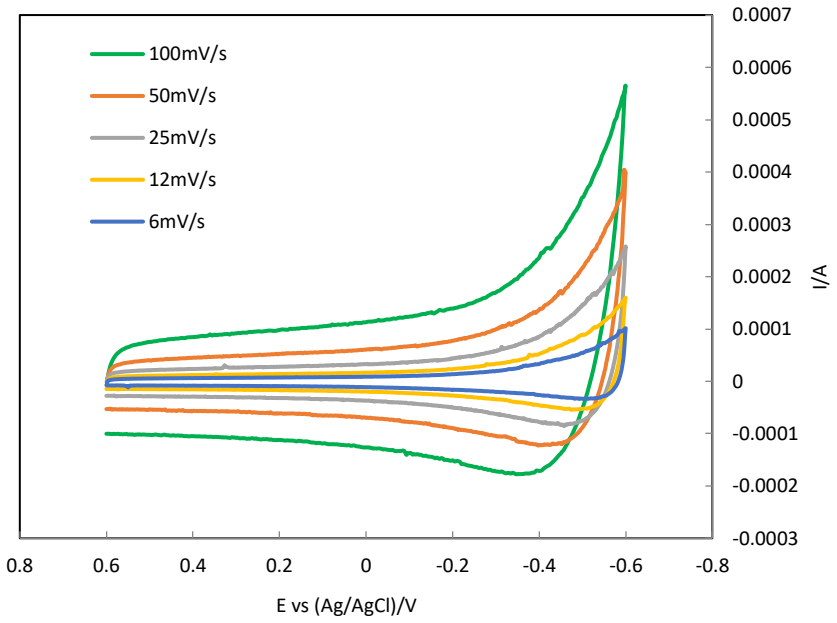

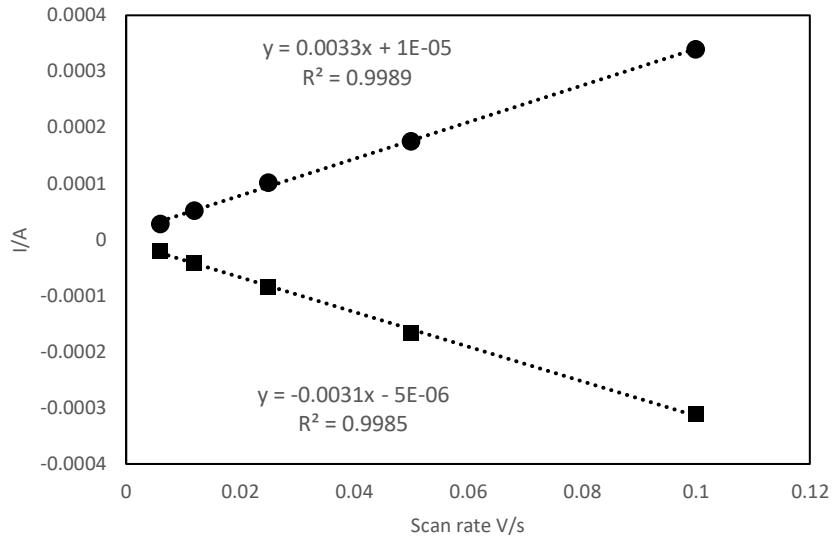

Figure 23 Electrochemical double layer (EDL) capacitance measurement (b) from cyclic voltammetry in 0.1 mol/L LiCl (a).

The EDL capacitance of various TiO_2 NT electrodes was also measured by using CA. A constant potential was applied to the system and the time-dependent current response was measured. An example CA of TiO_2 NT-37 electrode with 0.1 M LiCl at ±200 mV potential is given in Figure 24. The EDL capacitance can be calculated by equation 7

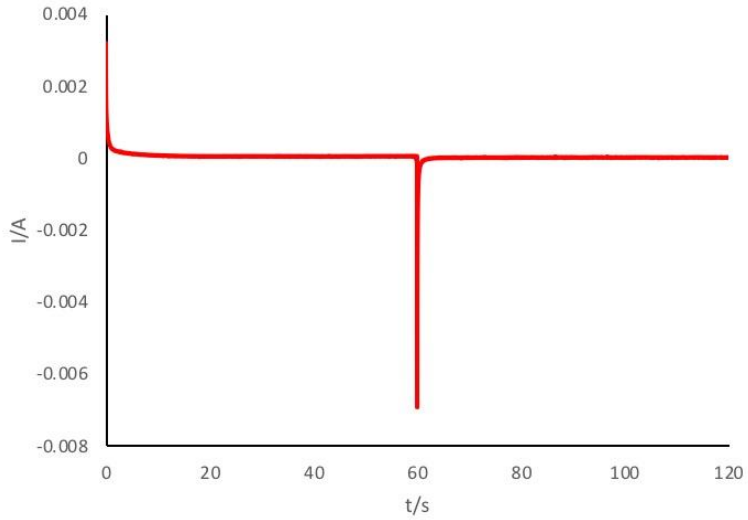

Figure 24 Chronoamperometry of TiO_2 NT-37 electrode with 0.1 mol/L LiCl at -0.3 V potential.

$$C_{DL-CA} = Q/E \qquad (7)$$

Where, $C_{DL\text{-}CA}$ is the EDL capacitance, E is the applied potential in CA test, Q is the total transferred charge in CA test, which can be obtained via numerical integration from equation 8.

$$Q = \int_0^t i\, dt \qquad (8)$$

where i is the time-dependent current response in CA test and t is the test time. Based on equation 7 and 8, the EDL capacitance of TiO_2 NT-37 with 0.1 M LiCl at -0.3 V is $C_{DL\text{-}CA}$= 6.37 mF.

In order to investigate the TiO_2 NT electrode diameter effect on EDL capacitance of alkaline metal ions, the EDL capacitance calculated through CV and CA method respectively is plotted and compared in Figure 25. From Figure 25 a to c, one is able to infer that the EDL capacitance values obtained from both CA and CV agree each other very well and increase with the increasing applied potential. In the case of NT-37 (Figure 25a), when potential increases from -200 mV to -500 mV, the $C_{DL\text{-}CV}$ of Li^+, Na^+, and Cs^+ increases from 3.2 to 6.45 mF, 4.3 to 9.45 mF, and 0.3 to 6.55 mF respectively. The $C_{DL\text{-}CA}$ of Li^+, Na^+, and Cs^+ increases from 2.64 to 9.2 mF, 4.13 to 9.50 mF, and 2.98 to 7.62 mF respectively. Moreover, for NT-37, the EDL capacitance for Li^+ and Na^+ is almost same but higher than that of Cs^+. For NT-41 (Figure 25b), the EDL capacitance follows the order of $Na^+ > Li^+ > Cs^+$; while for NT-45 (Figure 25c), the order turns out $Li^+ > Na^+ > Cs^+$. In disagreement with Classical Theory predictions, EDL capacitance is not the same for the three ions with the same charge at the same conditions of applied potential and level of confinement.

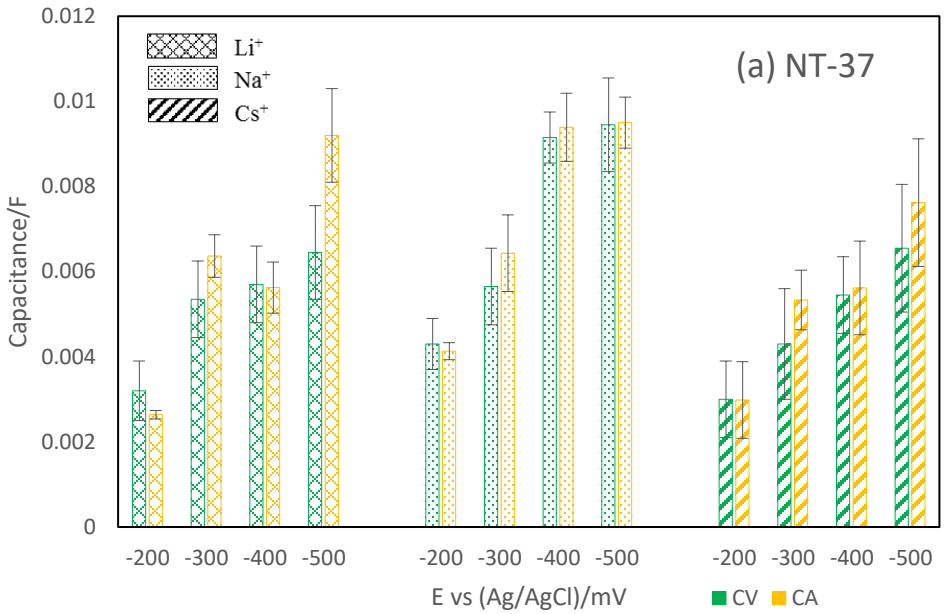
0.012
0.01
0.008
0.006
0.004
0.002
0
Capacitance/F
Li+
Na+
Cs+
(a) NT-37
-200 -300 -400 -500 -200 -300 -400 -500 -200 -300 -400 -500
E vs (Ag/AgCl)/mV
CV
CA

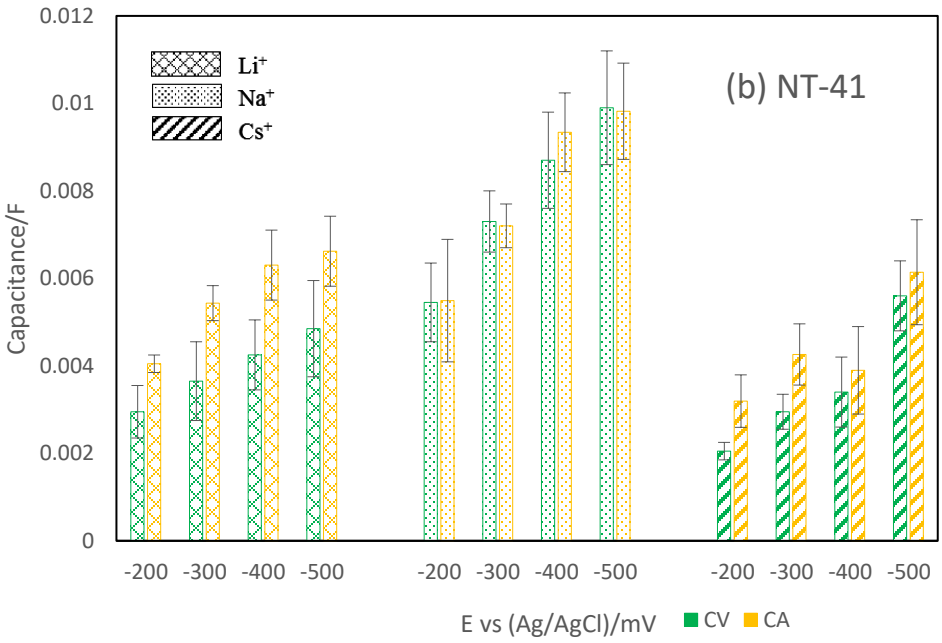
0.012
0.01
0.008
0.006
0.004
0.002
0
Capacitance/F
Li+
Na+
Cs+
(b) NT-41
-200 -300 -400 -500 -200 -300 -400 -500 -200 -300 -400 -500
E vs (Ag/AgCl)/mV
CV
CA

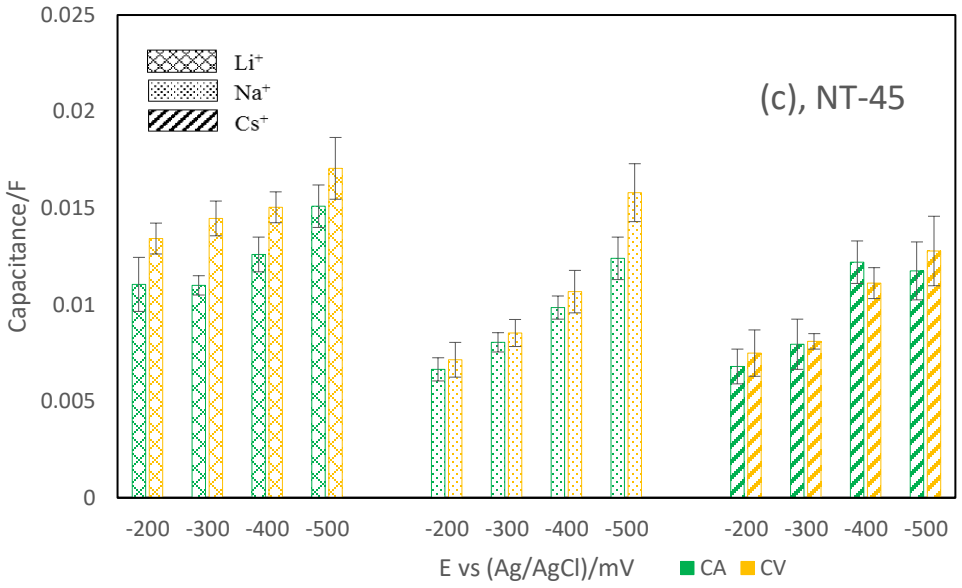

Figure 25 Ion effect on EDL capacitance of TiO_2 NT electrode with different pore sizes

Figure 26 summarizes the pore size effect on the EDL capacitance of TiO_2 NT electrode. For particular ion and applied potential, it was expected that higher EDL capacitance would trend with higher applied potential available for the formation of the EDL. Figures 26 a, b, and c depict the dependence of EDL capacitance on applied potential for NT-37, NT-41, and NT-45 respectively. As expected, the EDL capacitance increases proportionally to applied potential for any particular pore diameter and potential combination. For example, the $C_{DL\text{-}CV}$ for Cs^+ increased from 6.8 mF at -200 mV to 11.75 mF at -500 mV (Figure 26c) and $C_{DL\text{-}CA}$ increased from 7.49 mF at -200 mV to 12.78 mF at -500 mV. A similar rapid increase in both $C_{DL\text{-}CV}$ and $C_{DL\text{-}CA}$ with increased applied potentials was observed for Li^+, Figure 26a, and Na^+, Figure 26b with NT-41 and NT-45. However, the sensitivity of electrical capacitance to applied potential was not as steep as predicted in Classical Theory.

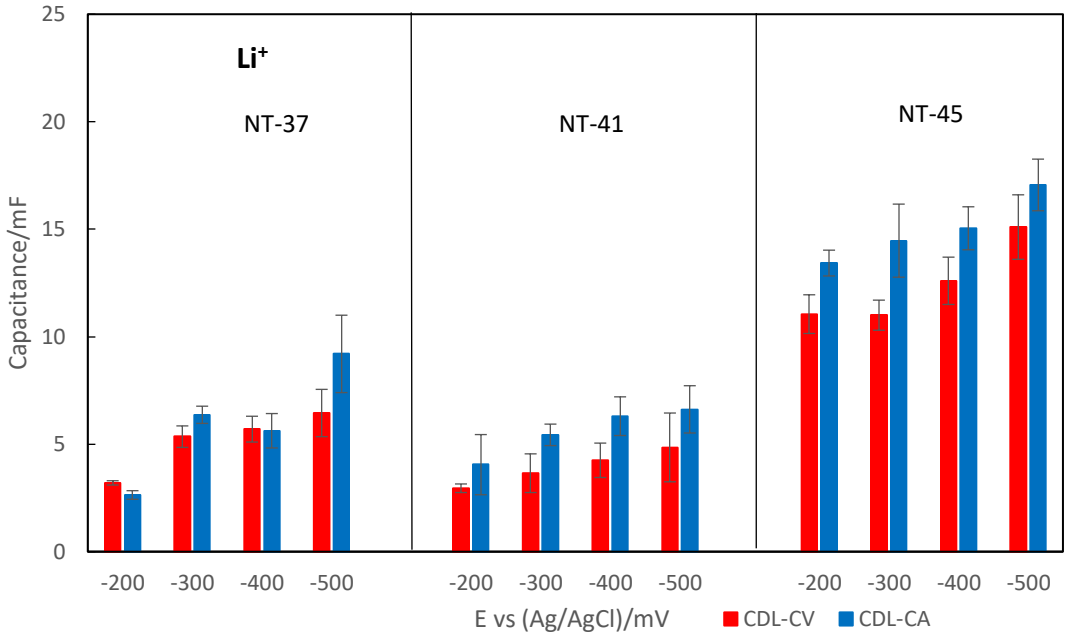
Li+
NT-37
NT-41
NT-45
Capacitance/mF
25
20
15
10
5
0
-200
-300
-400
-500
E vs (Ag/AgCl)/mV
CDL-CV
CDL-CA

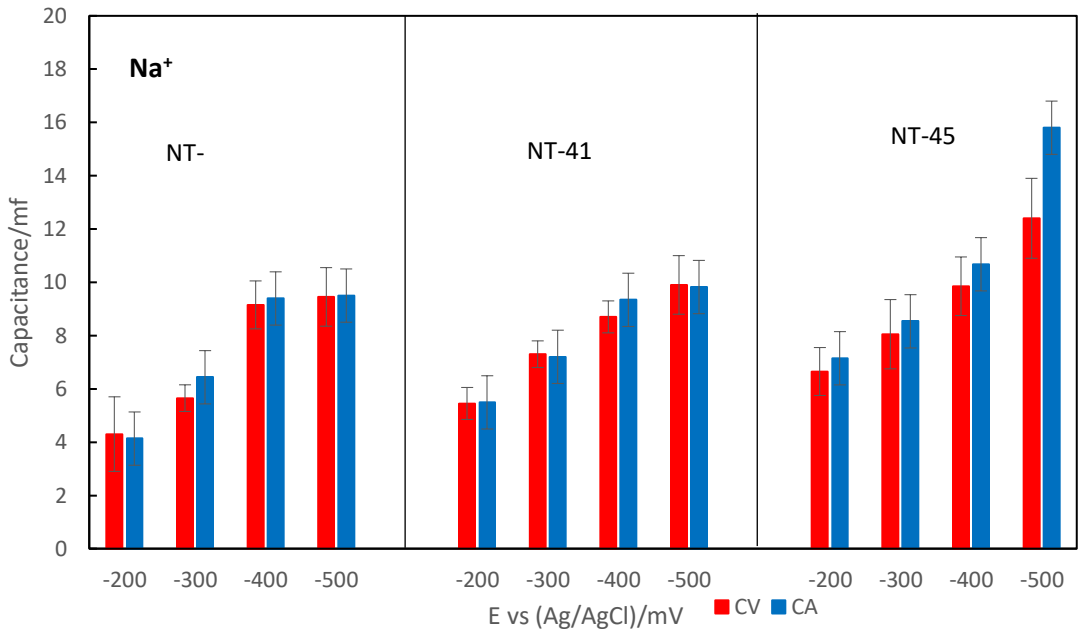
Na+
NT-
NT-41
NT-45
Capacitance/mf
20
18
16
14
12
10
8
6
4
2
0
-200
-300
-400
-500
E vs (Ag/AgCl)/mV
CV
CA

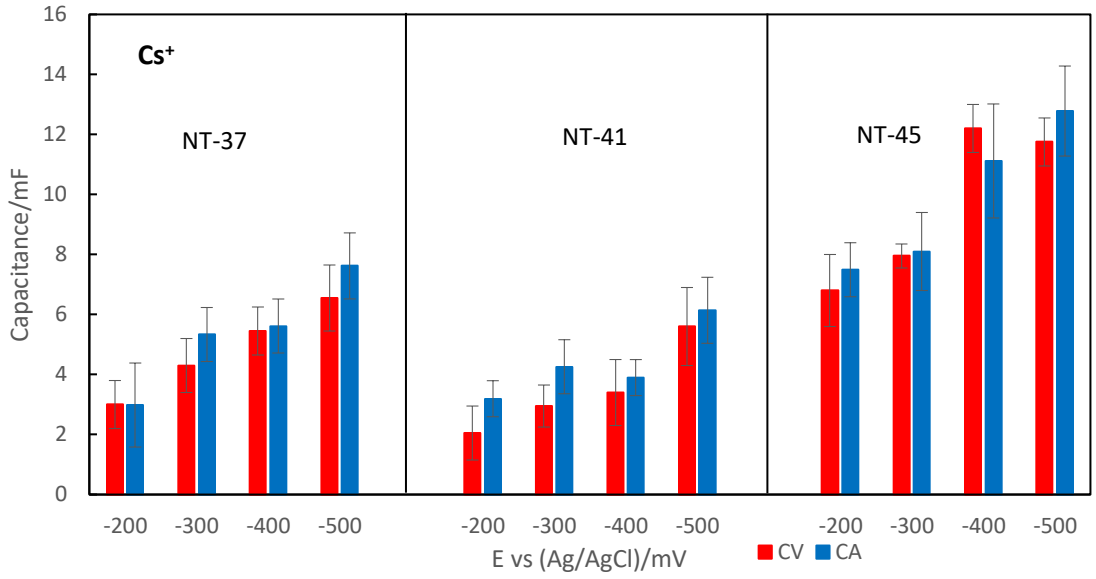

Figure 26 Pore size effect on the EDL capacitance of TiO_2 NT electrode with different ions a) Li, b) Na, c) Cs.

The TiO_2 NT electrode also differed in their EDL capacitance with the pore size, namely, surface area, varied. From Figure 26 a and c, for Li^+ and Cs^+, both $C_{DL\text{-}CV}$ and $C_{DL\text{-}CA}$ follow the trend NT-45 > NT-37 > NT-41. The $C_{DL\text{-}CV}$ of Li^+ at -500 mV is 15.1 mF for NT-45, 6.45 mF for NT-37, and 4.85 mF for NT-41. The $C_{DL\text{-}CA}$ of Li^+ at -500 mV is 17.06 mF, 9.2 mF, and 6.62 mF, for NT-45, NT-41, and NT-37, respectively. As for Na^+, the NT-45 still showed highest EDL capacitance in terms of $C_{DL\text{-}CV}$ and $C_{DL\text{-}CA}$ in the all tested potentials, from -200 mV to -500 mV; while the NT-41 and NT-37 held almost identical EDL capacitances in both $C_{DL\text{-}CV}$ and $C_{DL\text{-}CA}$. These results clearly indicated that the EDL capacitance depends upon the confinement, such as TiO_2 NT pore size, applied potential, and also ion type. The narrowest nanotubes in this work, NT-37, have the largest surface area, 89.6 m^2/g, NT-45 has the lowest, 20.7 m^2/g, and NT-41 stands in the middle, 31.4 m^2/g. One expects EDL capacitance to increase proportionally to surface area, according to Classical Theory predictions. However, EDL capacitance did not significantly correlate

with surface area in this work, which suggests there might be a compromise between surface area and steric resistance in the case of confinement. Increased surface area results from narrower, more densely-packed TiO_2 nanotubes in our case.

Summarizing, the EDL capacitance data just discussed discloses three perspectives: first, the EDL capacitances (both $C_{DL\text{-}CV}$ and $C_{DL\text{-}CA}$) is not the same for ions with the same charge at the same conditions of applied potential and level of confinement. Second, EDL capacitances increased with increasing applied potential but at a lower sensitivity than expected from Classical Theory, which was found to be the case for all ions and TiO_2 NT combinations. Third, contrary to predictions, EDL capacitance did not escalate proportionally with surface area. Degree of confinement plays an important role in EDL capacitance. For example, for same ions, at particular applied potential, the EDL capacitance follow the trend of NT-45 > NT-37 > NT-41. Additionally, for a specific pore size, different TiO_2 NT electrodes exhibit higher EDL electrical capacitances depending on the ionic species in the EDL. For instance, the NT-41 holds the highest Na^+ EDL capacitance, while the highest Li^+ EDL capacitance was obtained by NT-45.

4.4.5 Electrosorption capacity of TiO_2 NTs

Figures 27 a, b, and c depict the electrosorption capacity changes of Li^+ as a function of applied potential and TiO_2 NT pore size. In this case, the electrosorption capacity increased proportionally to applied potential. For example, the electrosorption capacity at -200 mV was 0.776 μmol/m^2, 1.26 μmol/m^2, and 3.85 μmol/m^2 for NT-37, NT-41, and NT-45 respectively. When applied potential was increased to -500 mV, the electrosorption capacity increased to 9.99 μmol/m^2, 4.27 μmol/m^2, and 18.6 μmol/m^2 for NT-37, NT-41, and NT-45 respectively. The associated electrosorption capacities for NT-

41 were a fraction of those obtained with NT-45 and NT-37 electrodes at the medium or high applied potentials. In the case of Li^+, for example, the NT-41 electrode resulted in an electrosorption capacity 4.26 μmol/m^2, which is only 22.8% and 43.0% of that for NT-45 (18.6 μmol/m^2) and NT-37 (9.9 μmol/m^2) for the same applied potential of -500 mV.

Figures 28 a, b, and c show the dependence of the electrosorption capacity of Na^+ on the applied potential for NT-37, NT-41, and NT-45, respectively. As in the case of Na^+, there was still a clear trend of increasing electrosorption capacity with increasing applied potentials but with a lower associated sensitivity. However, as in the case of Na^+, the electrosorption capacities obtained for NT-37 electrodes were comparable with those obtained for NT-41 electrodes and the electrosorption capacity for NT-45 is higher than those for NT-37 and NT-41. For example, at an applied potential of -500 mV, the electrosorption capacity for TiO_2-NT electrode NT-45 was equal to 15.8 μmol/m^2 compared to that of 10.1 μmol/m^2 and 8.8 μmol/m^2 for NT-37 and NT-41, respectively, under the same conditions.

Figures 29 a, b, and c show the dependence of the electrosorption capacity of Cs^+ on the applied potential for NT-37, NT-41, and NT-45, respectively. From the figure, we can also infer that the electrosorption capacities of Cs^+ for NT-45 and NT-37 were higher than that for NT-41, especially at high applied potential, -500 mV. The electrosorption capacities for NT-45 and NT-37 at -500 mV were 18.8 μmol/m^2 and 11.4 μmol/m^2, respectively, comparing with 9.56 μmol/m^2 for NT-41.

In summary, the electrosorption data above suggests two relevant phenomena. First, the proportionality of electrosorption capacity to applied potential and the sensitivity of

changes in electrosorption capacity with changes in applied potential depend on pore size (i.e., the degree of confinement). Secondly, electrosorption capacity does not necessarily increase proportionally with surface area, and this is contrary to Classical Theory predictions.[117] In fact, our data indicates that level of confinement (e.g., pore size) has a greater influence on electrosorption capacity than specific surface area. The wider nanotube, NT-45 (specific surface area of 20.7 m^2/g) exhibited comparable electrosorption capacities as NT-37 (specific surface area equal to 89.6 m^2/g) in spite of the surface-area advantage of the latter. Finally, NT-41 (surface area equal to 31.4 m^2/g) was the less effective electrode in terms of electrosorption, and exhibited a minimum in electrosorption capacity in all cases.

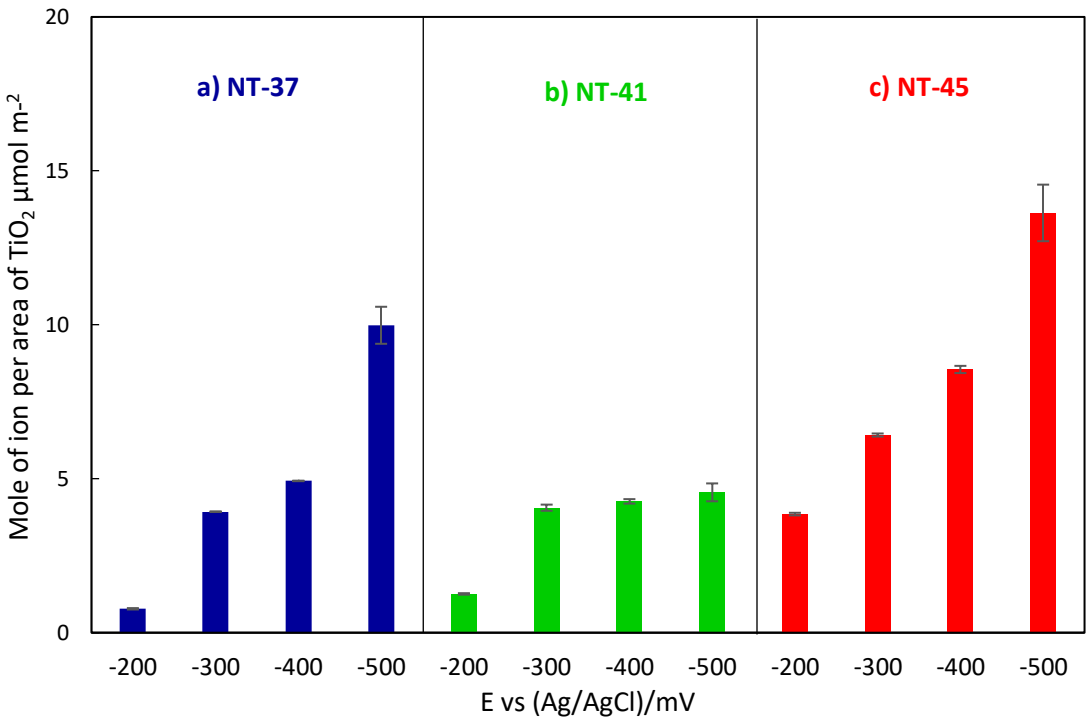

Figure 27 Electrosorption capacities per specific surface area of TiO_2 NT electrodes with various pore sizes for Li^+.

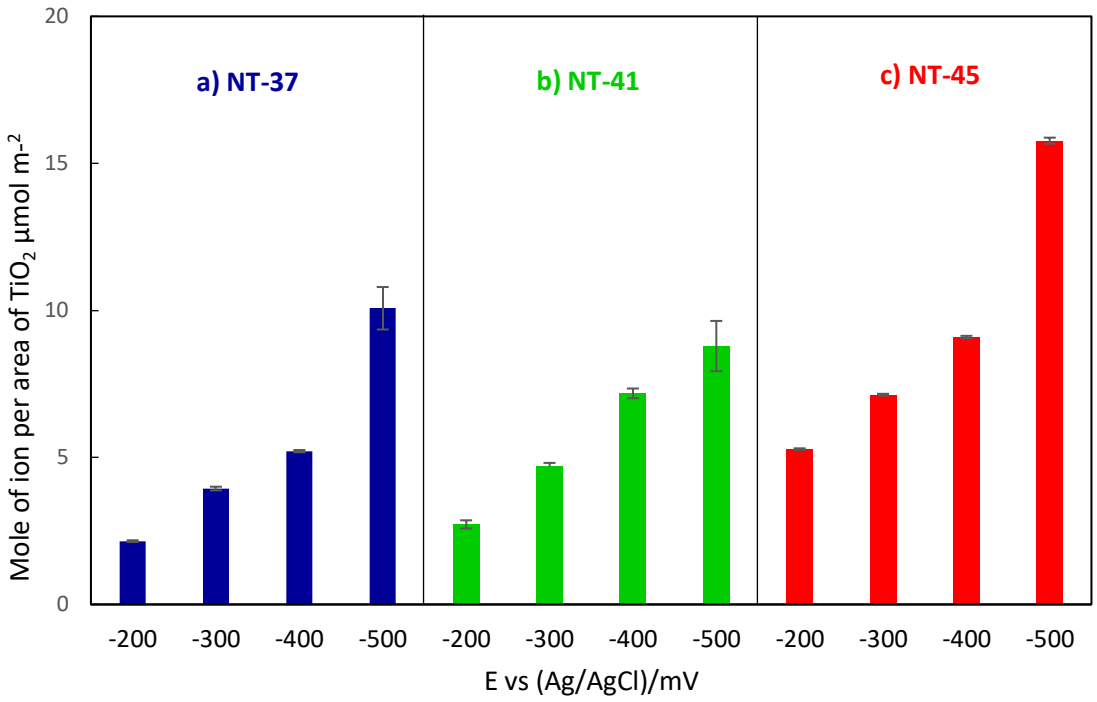

Figure 28 Electrosorption capacities per specific surface area of TiO_2 NT electrodes with various pore sizes for Na^+.

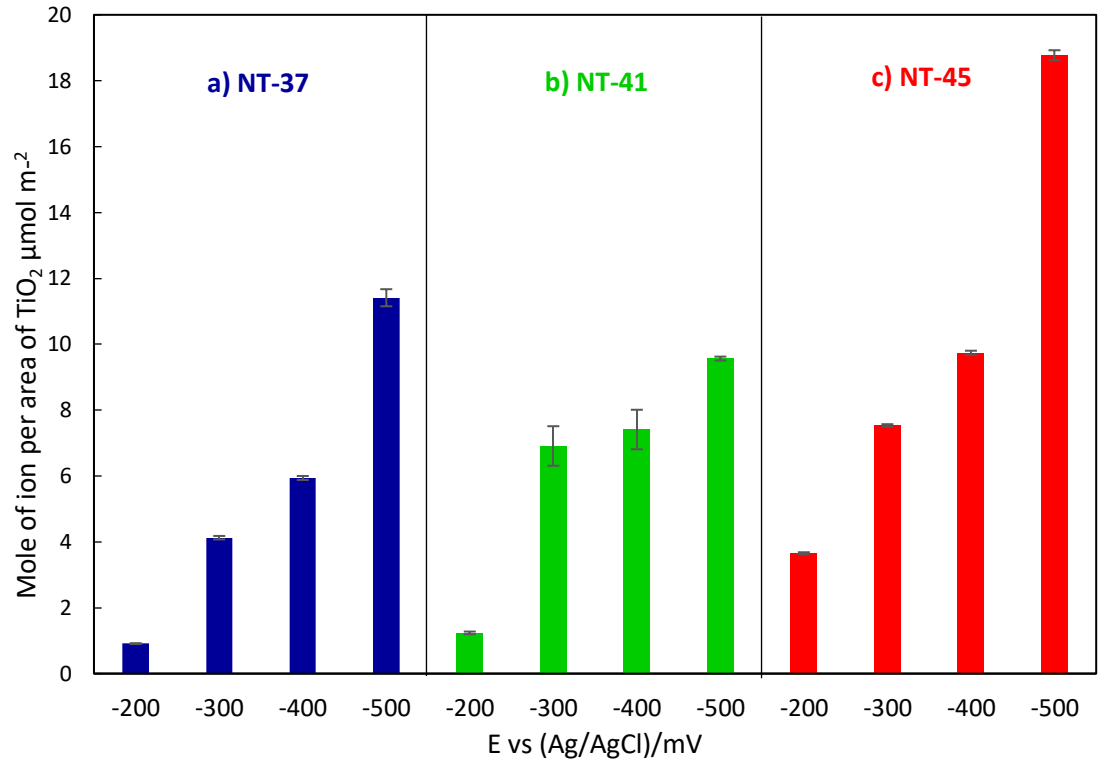

Figure 29 Electrosorption capacities per specific surface area of TiO_2 NT electrodes with various pore sizes for Cs^+.

4.4.6 Effect of ion type on ion electrosorption onto TiO_2 NTs

Figure 30 summarizes the electrosorption capacity of TiO_2 NT electrodes for Li^+, Na^+ and Cs^+ at increasing applied potentials. Results presented in Figures 27, 28 and 29 were rearranged to facilitate the discussion from the perspective of ion type.

At the lowest applied potential (-200 mV), Na^+ exhibited the largest electrosorption capacity for all pore sizes, with Cs^+ and Li^+ ions exhibiting no difference within experimental uncertainty. At the applied potential from -400 mV to -500 mV, the measured electrosorption capacity trend was $Cs^+ > Na^+ > Li^+$. This order is consistent with decreasing size of the hydration radii for Li^+, Na^+ and Cs^+, which are equal to 0.00382 nm, 0.00358 nm, and 0.00329 nm, respectively [133, 141]. For NT-37, at the potential of -300 mV and -400 mV, Li^+, Na^+, and Cs^+ exhibited almost identical electrosorption capacity (4.12 $\mu mol/m^2$ for Cs^+, 3.94 $\mu mol/m^2$ for Na^+ and 3.93 $\mu mol/m^2$ for Li^+, at -300 mV). In the case of NT-41, the electrosorption capacities for Cs^+ and Na^+ were higher than that for Li^+ at -300, -400, and -500 mV. Also, the sensitivity of electrocorption capacity to increases in applied potential was higher at larger pore sizes. For the case of NT-45, the electrosorption capacity for all ions increases more rapidly with increasing applied potential. According to classical EDL theory, ions carrying same charge should display a similar probability to be captured within the EDL during electrosorption, resulting in identical electrosorption capacities.[117] However, our results do not agree with this prediction—the hydrated ion radii played an important role in the electrosorption process. In the present study, all three alkaline metal ions with same charge, Li^+, Na^+, and Cs^+, demonstrated different electrosorption capacities depending on combinations of pore-size and applied potentials. We propose that smaller hydrated radiuses are more effectively captured within compact

EDLs during electrosorption in that they encounter less steric hindrance, especially at higher applied potentials. Furthermore, as pore size increases, the system becomes less determined by steric effects and more responsive to energy effects.

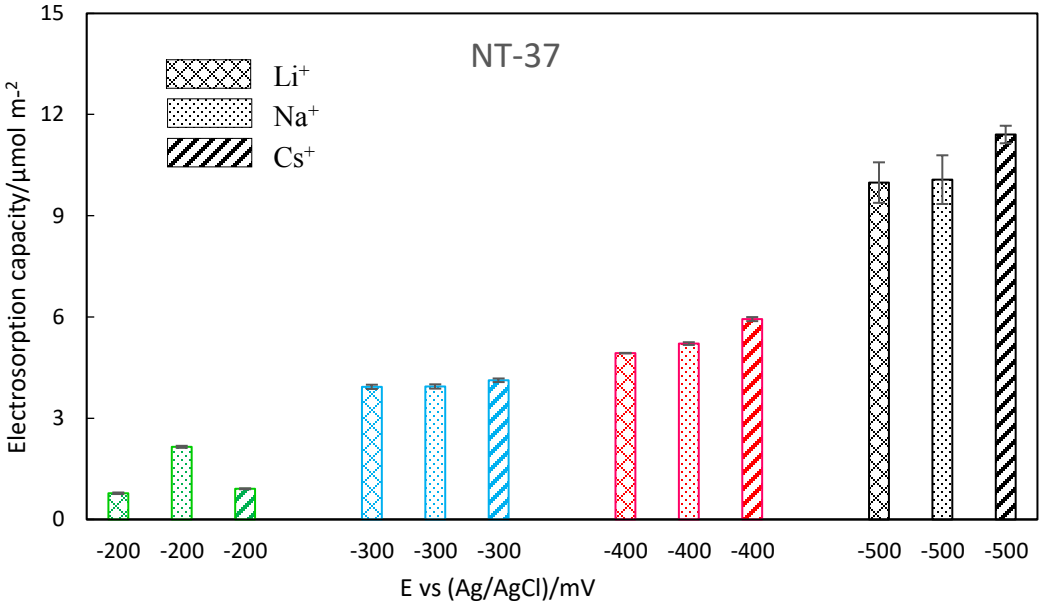

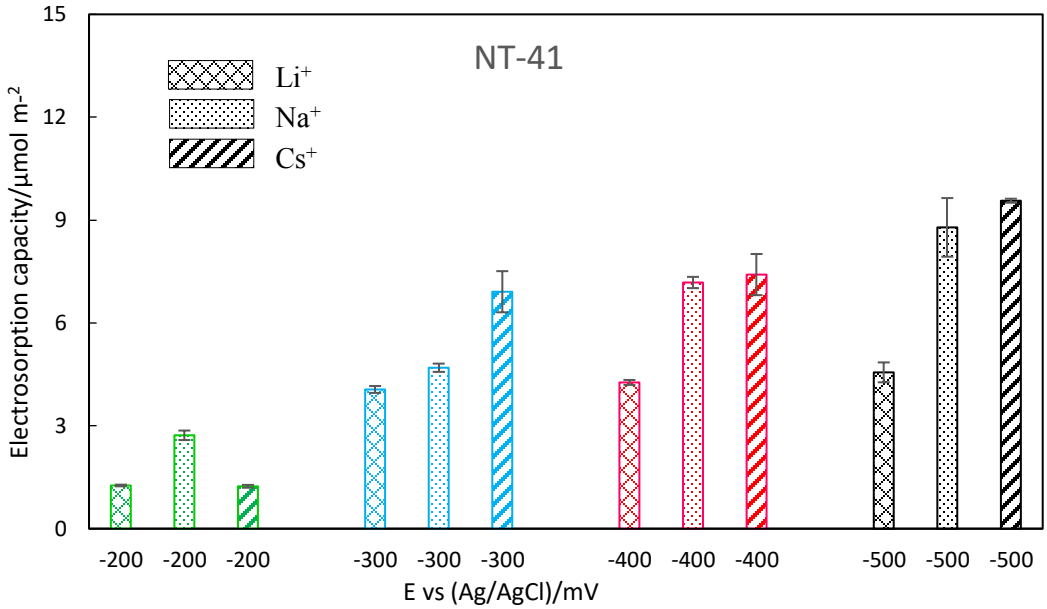

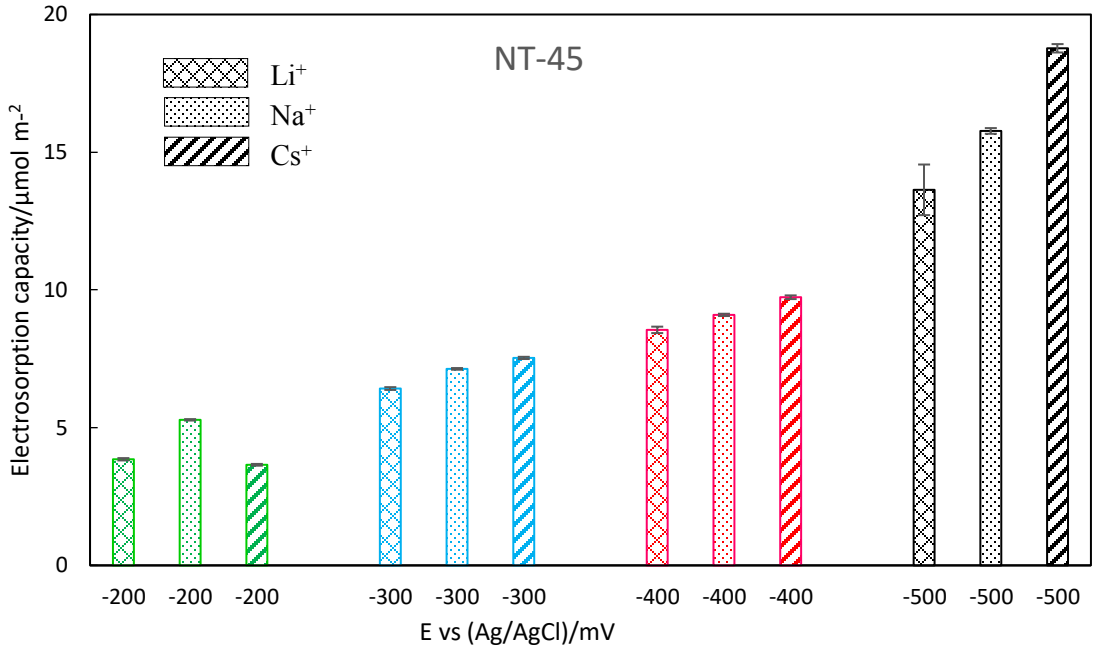

Figure 30 Comparison of the electrosorption capacities of various ions for different TiO_2 NT electrodes (a, for NT-37; b, for NT-41; c, for NT-45).

The possibility that other phenomena besides reversible electrosorption within the EDL might be influencing the results of this study was explored in three different ways. The first one was by charge/discharge cycles and study of the fluctuations in electrosorption capacities with the number of cycles of operation during CA. The purpose of these examinations were two folds: (a) ensure that only reversible EDL charging was contributing to the EDL properties measured in the present work, and (b) capture the variability in the measurements. Secondly, the shapes of CV curves at different scan rates and potential ranges were examined for the presence of Faradaic peaks and possible contribution of Faradaic processes to EDL capacitance. Finally, electrodes were visually inspected to detect changes in color, which did not take place in any of our experiments.

Figure 31 shows the electrosorption capacities of three typical TiO_2 NT electrodes for fifteen cycles. All TiO_2 NT electrodes experienced good regeneration ability of Na^+, Li^+, and Cs^+ ions for all applied potentials investigated in the present work (see Figure 30). Except for an irreversible electrosorption capacity drop between the first two cycles, the TiO_2 NT electrodes exhibited stable electrosorption capacities with little fluctuation confirming the reversible nature of the process studied, i.e. electrosorption.

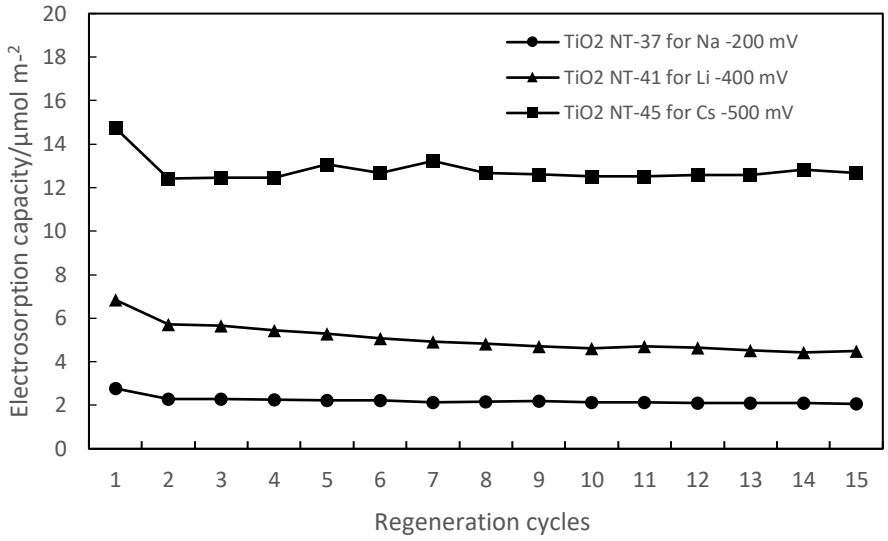

Figure 31 Electrosorption capacity for selected TiO_2 NT electrodes as a function of CA cycles.

4.5 Conclusions

A series of highly-ordered TiO_2 nanotube (TiO_2 NT) with two different crystalline structures, amorphous and anatase, were synthesized by anodization, and were used as model-system electrodes in the study of ion-size and crystalline structure effects during electrosorption of alkaline metal ions. The electrodes of controlled geometry allowed for the systematic investigation of ion-size and crystalline effects on electrosorption capacity, charging dynamics, and electrochemical active surface area (EASA), via well-known

electrochemistry techniques. The simple geometry of the electrodes allowed for the clear identification of steric effects on the behavior of EDL formation and structure that had been predicted via molecular simulations but had not been unequivocally determined via experimentation. The highly tunable, regular nanotube structure of the electrodes proposed in this work, made the elucidation of steric effects during electrosorption and EDL formation possible.

TiO_2-NT electrodes with the narrowest pores (pore diameter equal to 36.8 nm and specific surface area of 89.6 m^2/g) and the widest pore (pore diameter of 44.9 nm and specific surface area equal to 20.7 m^2/g) displayed the highest EDL electrical capacitance and electrosorption capacities for all ions examined in this work. This finding contradicts Classical Theory predictions where electrosorption capacity is strictly proportional to surface area, and highlights the importance of lower level of confinement in promoting ion-electrosorption. Additionally, a minimum in electrosorption capacity was detected for NT-41 electrodes (pore size equal to 41.4 nm and specific surface area of 31.4 m^2/g), the intermediate pore size studied in this work. This observation suggested that electrosorption onto compact EDLs might be favored for ranges of steric confinement in pores (smaller pore sizes) until other factors such as slow transport of ions into the pores due to steric hindrances and EDL overlapping lower the total amount of counterions present inside the pores. The net result is that electrosorption capacity may not necessarily peak at the smallest realizable pore size and that a minimum in electrosorption capacity may be found at intermediate pore sizes, because of a compromise between available surface area and pore diameter, in qualitative agreement with molecular simulation predictions.

TiO_2 NT electrodes with the widest pores explored in this work, NT-45, also exhibited the highest sensitivity of electrosorption capacity to applied potential changes, in agreement with Classical Theory, which points towards lower levels of confinement allowing for "more ideal" conditions for electrosorption. On the other hand, electrosorption capacity in the narrowest pores, NT-37, depicted a lower sensitivity to applied potential, enforcing the idea of the effects of confinement on EDL properties. Finally, TiO_2-NT electrodes with intermediate pore sizes, NT-41, did not show the expected behavior of electrosorption capacity with increasing applied potential. These observations combined with the minimum in electrosorption capacities also observed for the 41-nm pores suggest that there are complex interactions between energy and steric effects at all levels of confinement, particularly at NT-41.

The effects of confinement on the dependence of electrosorption capacity on surface area and applied potential were a function of the ion type in our experiments. Only two combinations of applied potential and pore diameter did not show differences in electrosorption capacity with different hydrated ion radii beyond experimental uncertainty. It is worth noting that ion-size effects were noticeable in spite of the fact that the nanotube diameters were two orders of magnitude the value of the hydrated radii of the ions.

The highly-ordered and uniform structure of the nanotubes used in this work provides a simple geometry comparable to that of molecular modeling systems. Confinement and ion-size effects measured in the present work show qualitative agreement with predicted behavior of EDL that has been reported in molecular modeling.

Finally, the results of this work suggest that nano-confinement effects could be in principle used to improve electrosorption capacity and/or tailor ion selectivity, as has been suggested by molecular modeling studies.

CHAPTER 5 ELECTROCHEMICAL HYDROGEN PRODUCTION WITH 3D TITANIUM/TITANIUM DIOXIDE NTS ELECTRODES

5.1 Motivation

In previous chapters, highly-ordered TiO_2 NT electrodes were successfully synthesized by finely tuning the anodization parameters. Afterward, this TiO_2 NT electrodes were successfully applied for studying the morphological effects on the charging dynamics and electrosorption capacity towards monovalent alkaline ions.

In this chapter, a novel strategy to fabricate hierarchically-structured, flow-through 3D Ti/TiO_2 NT electrodes for hydrogen evolution reaction (HER) will be presented. The 3D Ti/TiO_2 NT electrodes reported in this chapter take advantage of 3D printing and *in-situ* anodization to achieve efficient HER electrocatalysis via control of macro, micro and nano-structure of the electrodes. Most importantly, the preparation of the 3D Ti/TiO_2 NT electrode is facile and readily scalable since the fabrication does not include time- and energy-consuming processes such as complex precursor preparation and high-temperature heat treatments. The large-scale construction of 3D Ti/TiO_2 NT does not require high capital cost and the flow-through feature makes it very appealing for continuous, industrial-scale hydrogen production. This study also would like to provide evidence that the TiO_2 NT on the surface of the 3D Ti templates is the active catalytic surface promoting HER, by a two-step mechanism that contributes to the faster rate of the overall process. The 3D Ti templates contribute to fast HER reaction rates in terms of offering a seamless electron transfer network and large exposed active sites, namely TiO_2 NT.

5.2 Background

One of the most attractive renewable-energy fuel alternatives is hydrogen, since hydrogen is an ideal chemical energy carrier with energy density of 140 MJ kg^{-1} and no secondary contaminants generated during its oxidation.[142] Currently, hydrogen is mainly obtained from natural gas and coal, involving consumption of fossil fuels along with greenhouse gas release.[143] Therefore, securing a clean, safe, and sustainable approach for renewable hydrogen production has become one of the biggest barriers that hinder the leap from fossil-fuel-based energy society to hydrogen energy economy.

Water is naturally the most promising source for hydrogen production due to its abundance, low cost, and easy access on earth. Consequently, a great deal of effort has been devoted to generating hydrogen from water through sustainable, energy-efficient, and cost-effective processes that have the potential to work at industrial scales, such as photocatalytic water splitting and electricity-driven water dissociation.[144-147] The hydrogen evolution reaction (HER), $2H^+ + 2\bar{e} \rightarrow H_2$, is the basis for water splitting-based hydrogen production. In order to reach high energy efficiency, catalysts are widely used to minimize the potential required to initiate the HER.[148] To date, the best-known catalysts for the HER are noble metals, such as platinum. However, the scarcity and high price of noble metals substantially limit their large-scale deployment.[149]

Developing precious-metal-free catalysts for HER is a crucial step in moving towards a hydrogen-based energy economy. Molybdenum sulfide materials are one of the typical non-noble metal catalysts explored as alternative to platinum-group

catalysts due to their high electro-catalytic activity and stability for HER.[150-152] The synthesis of molybdenum-based catalysts, however, usually involves energy-intensive, time-consuming, and toxic processes that might hinder their application at industrial scales. For example, ultra-vacuum processing[151], high-temperature treatment[153], and sulfidization under H_2S gas are some of the steps involved in the molybdenum-based-catalysts synthesis.[151]

In 1972, Honda and Fujishima reported the occurrence of photocatalytic water-splitting by using crystalline titanium dioxide (TiO_2) electrode for hydrogen production, which opened the door for producing hydrogen from solar energy through a clean, low-cost, and environmentally friendly approach.[154] This finding triggered thousands of publications dealing with exploring TiO_2 photocatalytic activity for hydrogen production.[155-160] It is not surprising that TiO_2 has become one of the most common catalysts for photocatalytic hydrogen production owing to its abundance, low cost, and semiconductor properties. However, the wide band gap (3.2 eV) limits TiO_2 photocatalytic activity to UV light only. Therefore, the past decade has witnessed the proliferation of a wide range of studies geared towards improving the visible light absorption of TiO_2 via doping of TiO_2 with metal ions[161], coupling TiO_2 with low band gap semiconductor materials[162, 163], dye sensitization of $TiO_{2[160]}$, surface modification of TiO_2[164], and also use of TiO_2 as support for noble metals[165, 166]. Enormous efforts have been devoted to the enhancement of TiO_2 photocatalytic activity via increasingly-complex chemical functionalization. The resulting synthesis methods of improved TiO_2 materials have some inherent disadvantages including time-consuming and complex fabrication

processes, which may hinder scalability towards industrial use. For example, Ag_2S-coupled TiO_2 nanowire fabrication requires hydrothermal treatment over 72 hours[162], and cobalt-oxide loaded TiO_2/CdS composites synthesis consists of 12 hours reaction under vigorous stirring and drying under vacuum at 333 K for another 12 hours[159].

Another methodology explored for improving the performance of TiO_2-based catalysts for HER is to control catalyst architecture as a means to improve catalyst activity. An efficient strategy in order to control architecture is to employ a core-shell structure.[167-169] Yang et al. reported a core-shell nanostructure of rutile TiO_2 with sulfide surface (TiO_{2-x}:S) and reported a good photocatalytic activity with a hydrogen production rate of 0.258 mmol h^{-1} g^{-1}.[168] Kim and co-workers developed a core/shell structure of magnetic nanoparticles $NiFe_2O_4/TiO_2$ and applied it to photo-driven HER.[170] In spite of good catalytic performance for HER, the preparation of core-/shell catalysts generally requires several well-controlled and complex procedures. Another concern in core/shell designs is the poor contact between the core and shell material, which usually results in a dramatic decrease of catalytic activity with continuous use.

Embracing three-dimensional (3D) geometry for electrodes has become evident as another attractive way of obtaining high-performing HER photo-catalysts. For instance, Xu et al. utilized a multiscale 3D TiO_2 platform decorated with graphene quantum dots for photo-electro-chemical hydrogen production.[171] Li et al. developed a 3D Pt/TiO_2 architecture via a solvo-thermal method.[172] The 3D Pt/TiO_2 electrode exhibited high photocatalytic activity in the hydrogen production

test. However, a noble metal is still required to boost the photocatalytic activity of TiO_2.[172] To our knowledge, TiO_2 has yet to be explored for electro-catalytic HER.

In this work, we report on the performance for hydrogen production of hierarchically-structured Ti-core/TiO_2-coating electro-catalyst. The catalysts were produced via 3D printing and in-situ anodization, in order to superimpose highly-ordered TiO_2 NTs onto hierarchically 3D Ti-metal templates used as current collectors. The reported hierarchically-structured Ti/TiO_2 materials were tested in this study for HER activity and found as good candidates to overcome the hurdles towards renewable, industrial-scale hydrogen production.

5.3 Experiment procedures and materials

5.3.1 Synthesis of the hierarchical flow-through 3D Ti/TiO_2 NT electrode

3D Ti templates were printed with an additive manufacturing method using ARCAM Electron Beam Melting equipment.[173, 174] The templates had dimensions of 2.5 × 2.5 × 0.22 cm. Upon the synthesis of hierarchical flow-through 3D Ti templates, the titanium dioxide nanotube (TiO_2 NT) electrodes were grown on the base surface through anodization following the method described in previous work.[175] [89, 176] A piece of 3D Ti template was cut to the desired electrode size and rinsed with ethanol. A solution of 147 mL Ethylene Glycol, 3mL of distilled water, and 280 mg of Ammonium Fluoride was introduced into a temperature controlled anodization cell under dry air. The sample was anodized at 15 °C for 1 hour in this solution with a platinum counter-electrode at fixed voltages of 60V, depending on the electrolyte for each electrode. After anodization, the electrode was removed from solution, rinsed with methanol, and allowed to air-dry. The 3D Ti template was also anodized with water based electrolyte by employing an electrolyte consisting of 300 mL DI water and 576.2 mg Ammonium Fluoride. The

pH value of the water-based electrolyte was set up to 3.0 by adding sulfuric acid and then the anodization process was carried out at 15 °C for 1 hour with a platinum counter-electrode at fixed voltages of 20V.The morphology of the hierarchical flow-through Ti/TiO_2 electrode was examined by scanning electron microscopy (SEM). The SEM measurement was carried out on the MIRA3 field emission SEM (TESCAN, PA) equipped with Bruker x-flash energy-dispersion microanalysis system (Bruker, MA).

5.3.2 Electrochemical H_2 production

The electrochemical measurements were performed at room temperature using a BASi Cell stand controlled by a BASi C3 potentiostat, in which the working electrodes were the 3D Ti/TiO_2 composites as detailed above, the counter electrode was a BASi MW-1032 platinum electrode, and the reference electrode was BASi Ag/AgCl (BASi MW-2052). All potentials reported in this work were normalized to that of the RHE. The polarization curves were obtained by linear sweep voltammetry (LSV) test, which is carried out by sweeping the potential from -0.35 V to 0.05 V with a sweep rate of 5 mV s^{-1} at room temperature in 0.5 M H_2SO_4, and the potential from -0.55 V to 0.05 V with a sweep rate of 5 mV s^{-1} at room temperature in 1 M KOH. The electrochemical impedance spectroscopy (EIS) tests were performed in the same configuration at overpotential of 500 mV with frequency ranging from 1 MHz to 1 kHz by Gamry Reference 6000 (Gamry, PA).

5.4 Results and discussion

5.4.1 Characterization of 3D Ti/TiO_2 NTs electrode

The morphology of 3D Ti/TiO_2 NT electrode was studied by scanning electron microscopy (SEM) (Figure 32b-f). Figure 1a is the image of 3D Ti/TiO_2 NT electrode after anodization. The 3D Ti/TiO_2 NT electrode has visible hierarchical structure, with macro-porosity and microporosity (nanopores). The macroporosity provides unique flow-through

features, which maximizes the contact area between the electrolyte and catalyst (TiO_2 NT) in the present study and favor HER. From Figure 1b, one can observe that the grid of 3D templates is about 1-mm and the grid-layer distance is about 0.5 mm. These features can be adjusted by modifying the 3D printing parameters. Assisted by the 3D printing technique, the 3D electrode-framework can be easily produced for large-scale operations via a cost-effective approach. In Figure 1d, the TiO_2 NT layer grafted onto the surface of 3D Ti templates via in situ anodization can be clearly visualized. The 3D Ti templates are completely wrapped by the TiO_2 NT layers. Minor charging (bright area) is also observed due to the conductivity difference between the Ti basis and TiO_2 NT.

The TiO_2 NT synthesized with two different formulations of anodization baths on identical 3D Ti templates showed significant variation in morphology. By comparing Figures 33a and 33b, it is apparent that the morphological structures of ethylene-glycol-based TiO_2 NT (TiO_2 NT-EG) and water-based TiO_2 NT (TiO_2 NT-W) have some differences. The uniformity of the nanotube structure in the case of TiO_2 NT-EG is more obvious than that of the TiO_2 NT-W. This difference stems from the fact that the water-based anodization bath exhibits higher chemical etching rate for the oxides (namely, TiO_2 NT), than the organic-based electrolyte (ethylene glycol in the present study). The balance between the rates of oxide-layer formation and re-dissolution might be slightly off-set towards re-dissolution of the oxide layer, resulting in long, thin-walled nanotubes in the aqueous case. Meanwhile, limited charge transfer during the anodization process is observed due to low electrical conductivity of the ethylene-glycol-based anodization bath, a larger resistive current drop. As a result, the mass of TiO_2 NT-EG obtained during the same anodization time on the same 3D Ti template was 38% of that of TiO_2 NT-W.

Additionally, the oxide-layer re-dissolution rate was also lower, resulting in short, thick-walled nanotubes in the organic case. From the SEM images one can also infer that the TiO_2 NT-W is more densely packed on the surface of 3D Ti prints, suggesting a larger amount of nanotubes than that of TiO_2 NT-EG, as shown in Figures 33 a and b.

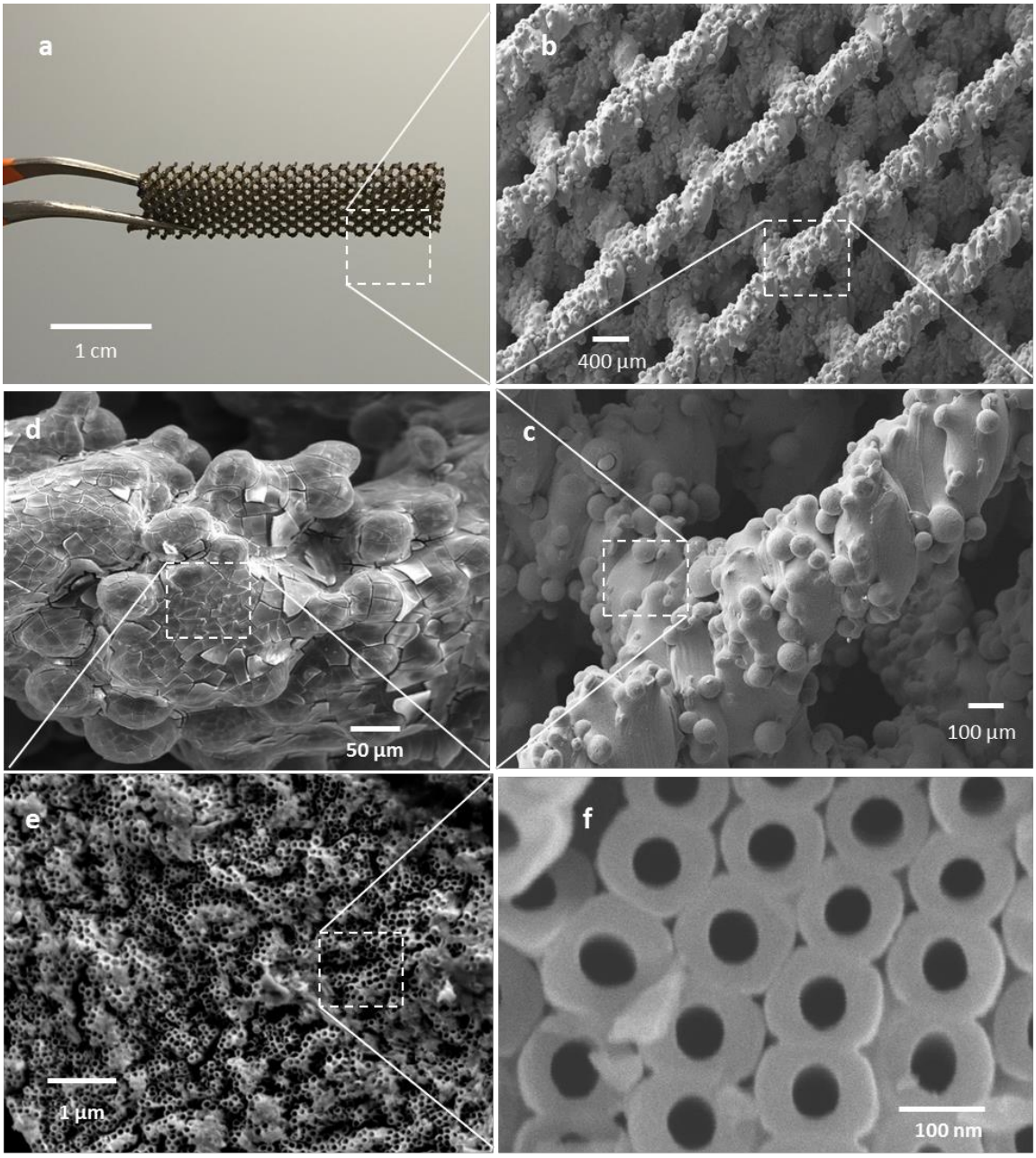

Figure 32 a-f Image and SEM micrographs of 3D Ti/TiO_2-NT-EG under various magnification.

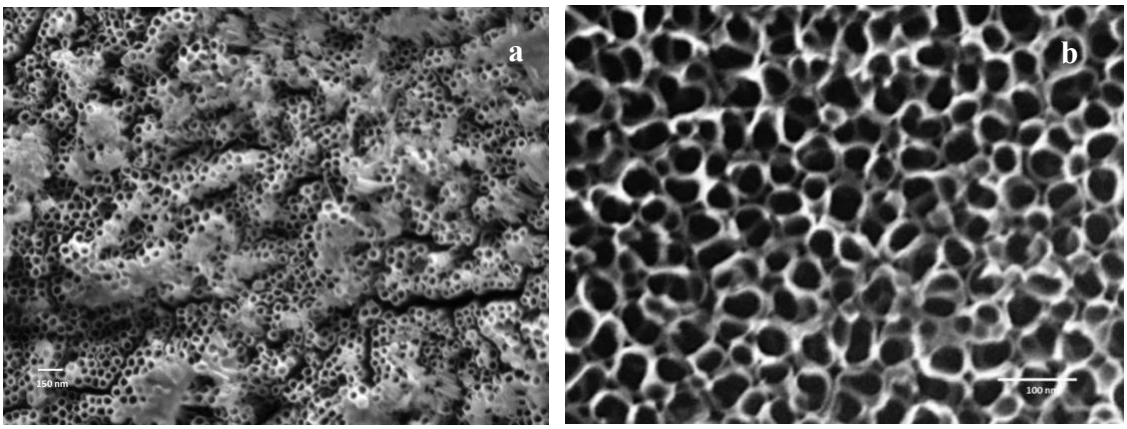

Figure 33 Morphology of 3D Ti/TiO_2-NT-EG, (a), and Ti/TiO_2-NT-W, (b).

Energy dispersive X-ray spectroscopy (EDS) results confirmed the successful anodization of TiO_2 NT on the surface of 3D Ti template (Figure 34) with the two electrolyte-formulations used in this work (i.e., ethylene glycol-based and water-based anodization baths). Figure 34a shows the EDS pattern of the bare 3D Ti templates, in which an oxygen peak cannot be found. Electrodes fabricated via anodization with the two bath formulations, water based and EG based, clearly present oxygen peaks around 0.5 KeV in Figures 34b and 34c, corresponding to the TiO_2 NT-EG and TiO_2 NT-W respectively, confirming that the nanotube structure observed via SEM on the surface of 3D Ti templates is made of TiO_2. It is worth pointing out that the intensity of oxygen peak for TiO_2 NT-EG is lower than that of TiO_2 NT-W, which agrees with our previous conclusions from SEM images that water-based anodization formulations result in thin-walled, densely packed TiO_2 nanotubes, even if those are slightly scarified. The aluminum and carbon elements found in the 3D Ti/TiO_2 NT composites are necessary ingredients for manufacturing the 3D printing ink.

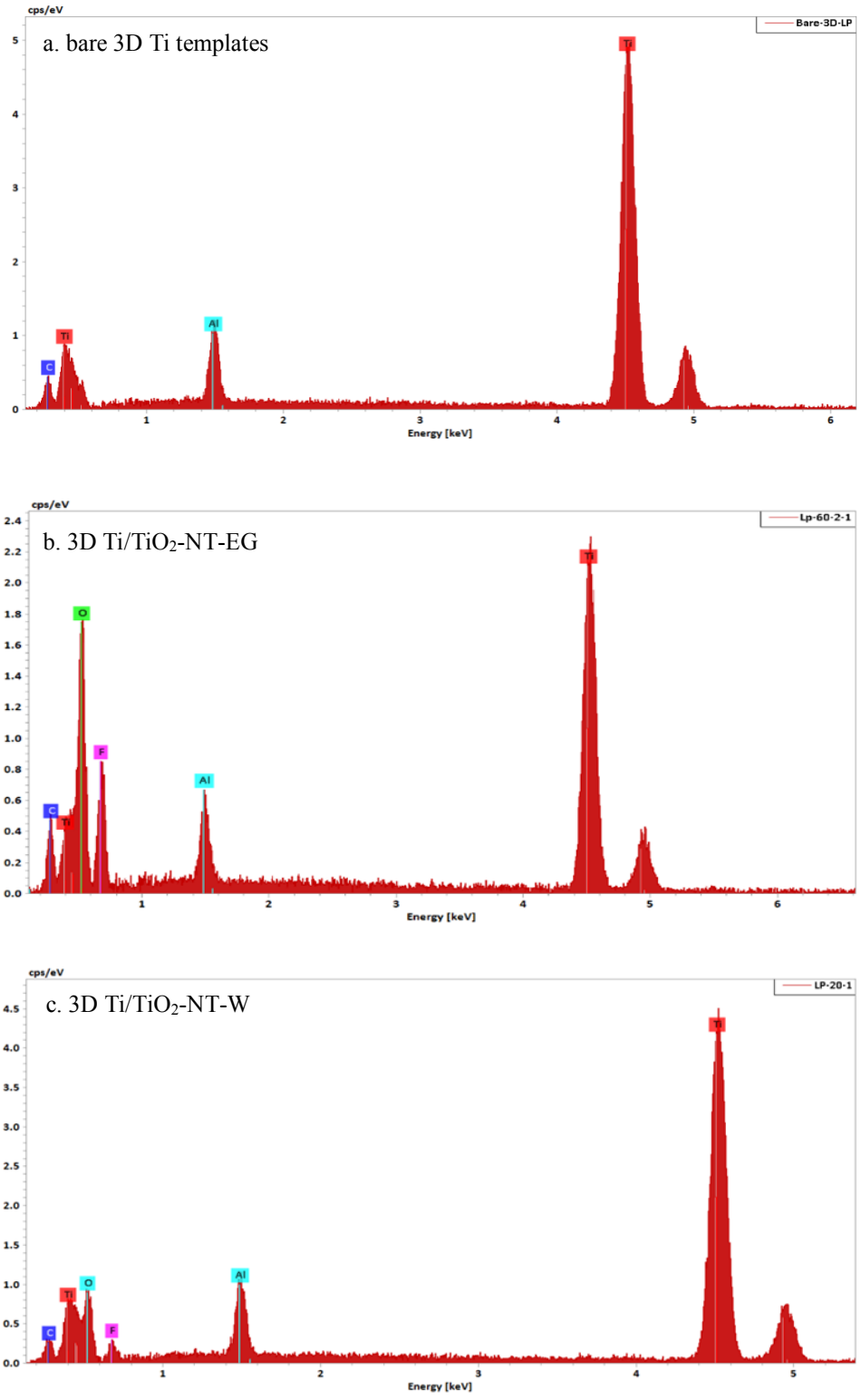

Figure 34 EDS spectra of bare 3D Ti templates (a), 3D Ti/TiO_2-NT-EG (b), and 3D Ti/TiO_2-NT-W (c).

5.4.2 Electrochemical hydrogen production test

Upon successful synthesis of the 3D Ti/TiO_2 NT electrodes, their catalytic activity towards HER was carefully examined in a three-electrode test system with acid media. Figure 35 shows the electrocatalytic performance of bare 3D Ti templates, 3D Ti/TiO_2 NT-EG, and TiO_2 NT-W for H_2 generation in 0.5 M H_2SO_4 electrolyte. Figure 35a compares the polarization curves obtained based on various samples, in which the featureless polarization curve of bare 3D Ti templates demonstrates the 3D Ti templates do not have catalytic activity for HER. In contrast, both 3D Ti/TiO_2 NT-EG and 3D Ti/TiO_2 NT-W show rather high catalytic activity in the test, evidencing a sharp increase in catalytic reduction current density, Figure 34a. The onset potential of the HER is observed at around -45 mV vs. RHE for TiO_2 NT-W and -87 mV vs. RHE for TiO_2 NT-EG, suggesting both TiO_2 NT-W and TiO_2 NT-EG have good catalytic activity for HER. The dependence of overpotential (η) on the logarithmic current density (j) was plotted in Figure 35b. The linear relationships of η and log J observed from Figure 35b, namely the Tafel slope, outlined the HER kinetic metrics of the TiO_2-NT catalysts, in which the Tafel slope values of 40 and 56 mV dec^{-1} were found for TiO_2 NT-W and TiO_2 NT-EG respectively, via linear regression of the above mentioned curves. Compared with the Tafel slope of the state-of-the-art Pt/C catalyst ~ 30 mV dec^{-1}, both 3D Ti/TiO_2 NT electrodes exhibit competitive HER catalytic activity. The observed Tafel slope obtained for the 3D Ti/TiO_2 NT-W electrode is smaller than that of other HER catalysts reported in recent literature (Figure 35), indicating that HER kinetics is effectively promoted by the 3D Ti/ TiO_2 NT-W catalyst.

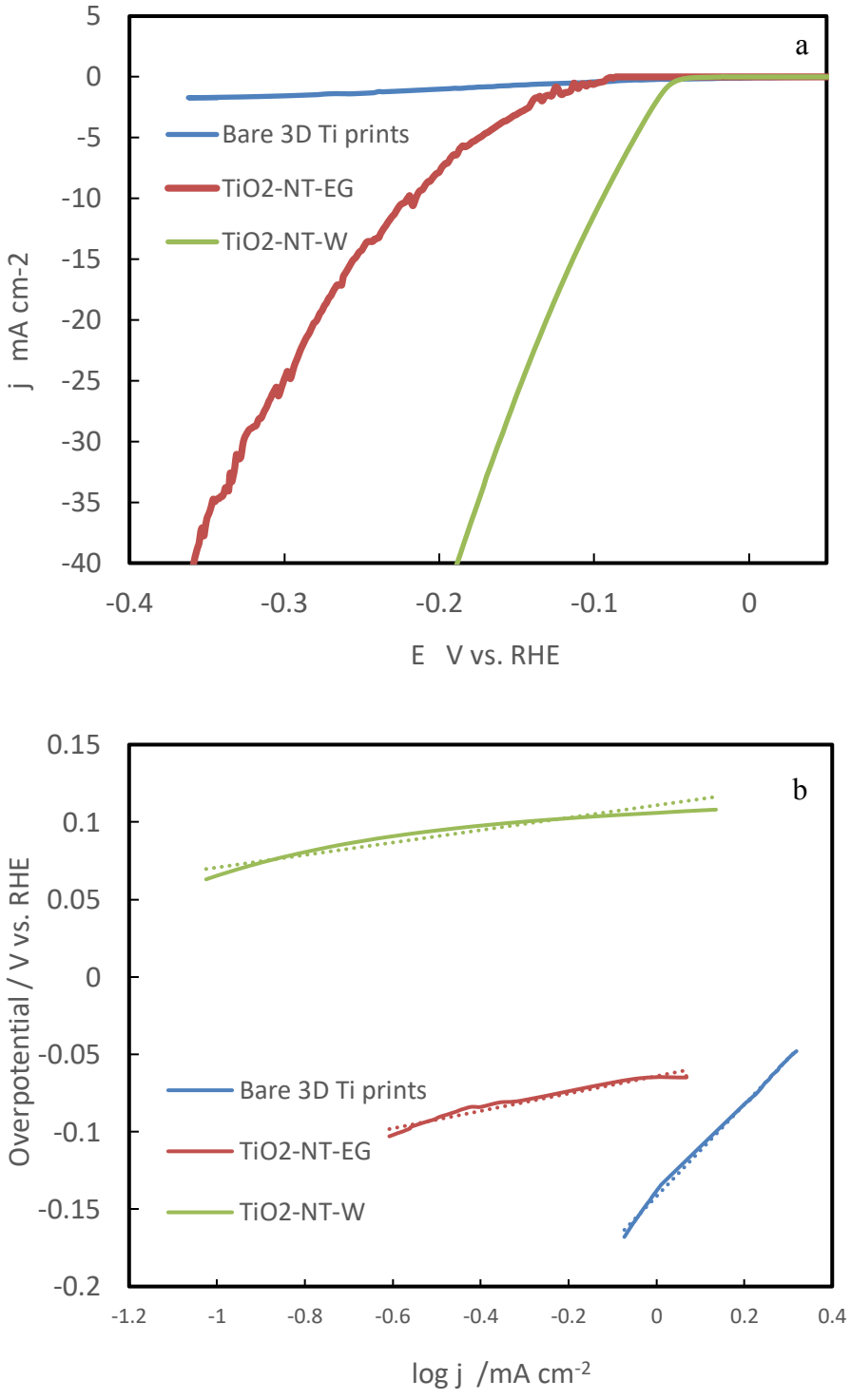

Figure 35 (a) Polarization curves for HER on bare 3D Ti templates, Ti/TiO_2-NT-EG, and Ti/TiO_2-NT-W in 0.5 M H_2SO_4. (b) Tafel plots for the various samples derived from (a) obtained via linear regression shown in dotted lines.

Table 3 Onset potential for HER and overpotential at 10 mA cm^{-2} for various catalysts.

Catalysts	Onset potential (mV)	Overpotential (mV) at 10 mA cm^{-2}
3D Ti/TiO_2-NT-W in this work	-45	92
3D Ti/TiO_2-NT-EG in this work	-87	215
3D nanoporous Co_2P [177]	-24	80
Edge-terminated MoS_2 [178]	-100	149
MoP [152]	-50	500
Amorphous MoS_3 [135]	-150	200
β-Mo_2C nanotubes [179]	-82	172
Ni-S based metal organic framework [180]	N/A	238

In Table 3, the onset potential for H_2 evolution and the overpotential at the current density of 10 mA cm^{-2} measured for our catalysts are compared with other promising catalysts reported in the literature for HER. The onset potential of TiO_2 NT-W is -45 mV, which confirms that the TiO_2 NT-W can launch HER with energy requirements close to the commercial Pt/C catalyst. To reach 10 mA cm^{-2} current density, the operation overpotential for the TiO_2 NT-W and TiO_2 NT-EG electrodes are 92 and 215 mV, respectively. From extrapolation of the Tafel plots, exchange current (j_0) for the TiO_2 NT-EG was determined to be equal to 7.68×10^{-3} mA cm^{-2}; and the value corresponding to TiO_2 NT-W was 2.13×10^{-4} mA cm^{-2}. Based on the electrochemical tests for HER

performed in this work, it can be concluded that the 3D Ti/TiO_2 NT-W outperformed several recently documented HER catalysts, and the catalytic activity of the 3D Ti/TiO_2 NT-EG is not as high as that of the 3D Ti/TiO_2 NT-W. The Tafel slope for the 3D Ti/TiO_2 NT-EG catalyst is 56 mV dec^{-1} (compared to 40 mV dec^{-1} for 3D Ti/TiO_2 NT-W), and this electrode also required a higher operation overpotential at 10 mA cm^{-2}.

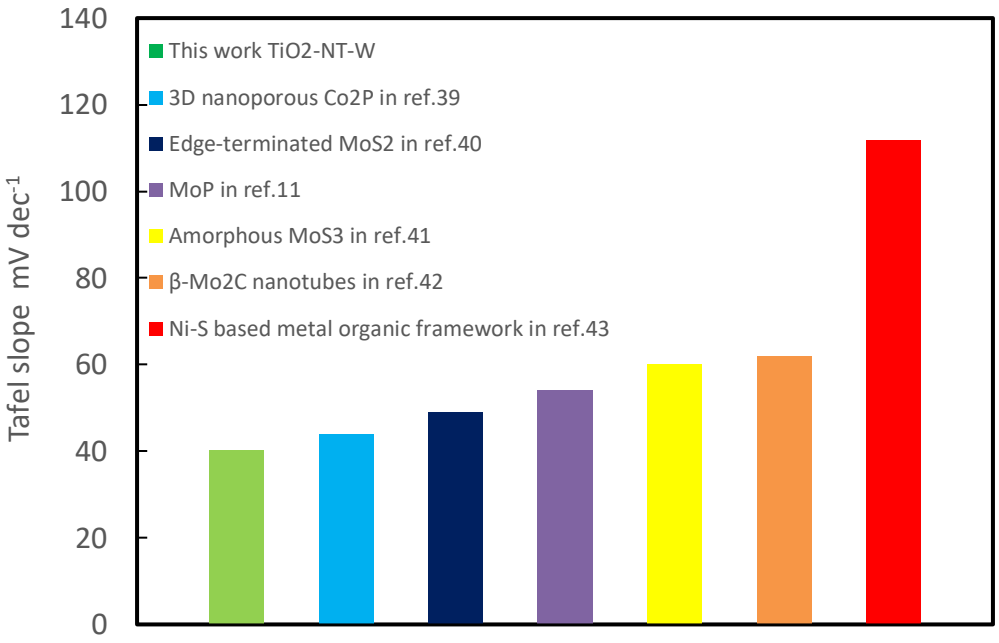

Figure 36 Comparison of Tafel slopes of various HER catalysts in recent published articles.

Figure 37 a and b show the electrocatalytic property of 3D Ti/TiO_2 NT electrode in basic conditions. One can observe that the 3D Ti/TiO_2 NT electrode also shows catalytic activity towards HER at basic conditions, but this activity is lower than that in acidic conditions, i.e., the Tafel slopes are higher. The Tafel slope for 3D Ti/TiO_2 NT-W and 3D Ti/TiO_2 NT-EG is 103.7 and 141.1 mV dec^{-1}, which is still higher than the 3D Ti prints, whose Tafel slope corresponds to 210 mV dec^{-1}. The HER catalytic activity of 3D Ti/TiO_2 NT electrode in basic conditions, which is not as high as that in acidic condition, is probably

depressed by the elevated pH value which translates in lower concentrations of protons necessary to adsorb onto the surface and initiate the set of reactions of HER. Additionally, HER in basic conditions follows a different, less studied reaction mechanism, which may exhibit potentially lower-rate controlling steps. Finally, it must be noted that very few catalysts, mainly platinum, are capable of enabling HER in the full pH range, from acidic to basic.

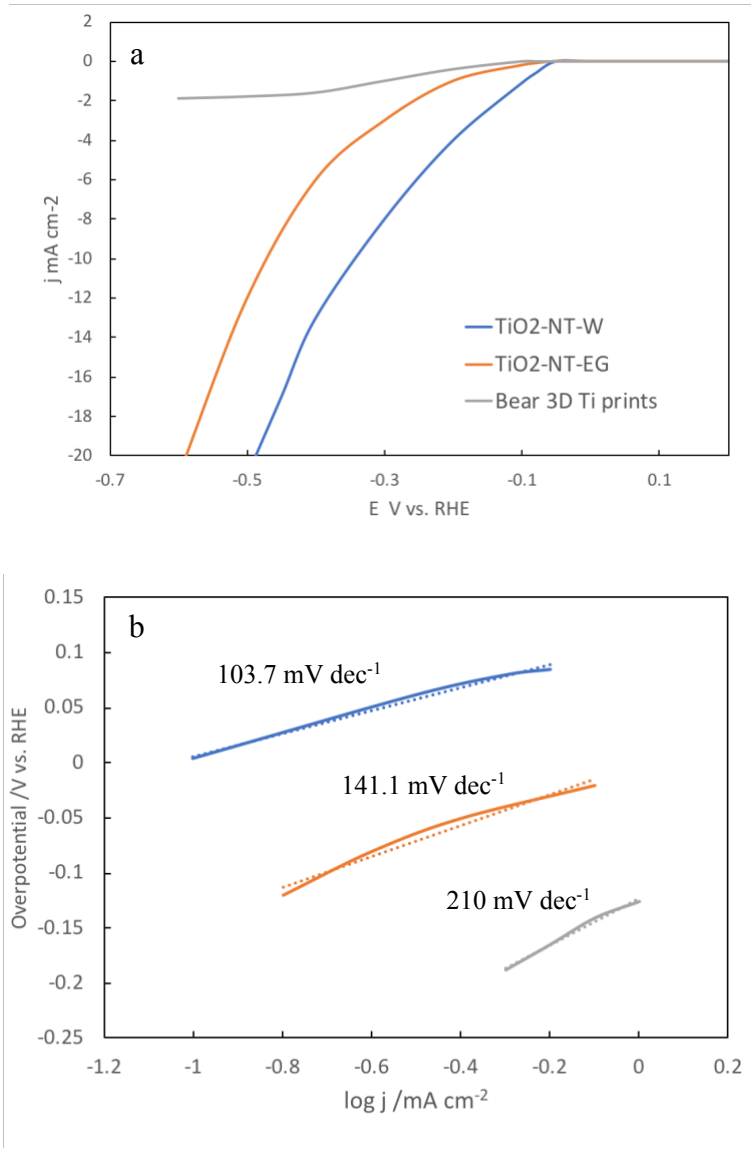

Figure 37 (a) Polarization curves for HER on bare 3D Ti templates, Ti/TiO_2-NT-EG, and Ti/TiO_2-NT-W in 1 M KOH. (b) Tafel plots for the various samples derived from (a) obtained via linear regression shown in dotted lines.

5.4.3 Mechanism of 3D Ti/TiO_2 NT electrode catalytic activity

The classical HER reaction mechanisms proposed for acid media (i.e., Volmer reaction, Heyrovsky reaction, and Tafel reaction) can be used as a framework to interpret the different values of Tafel slope for the 3D Ti/TiO_2 NT electrodes with HER kinetics.[181] Specifically, in acidic and aqueous electrolyte, HER is usually comprised of three steps: hydrogen adsorption, reduction and subsequent desorption in the form of molecular hydrogen. Fast proton uptake, reduction, and desorption of molecular hydrogen are necessary to achieve high catalytic activity. Hydrogen reduction can happen either between two-adsorbed hydrogen atoms (Volmer-Tafel reaction mechanism) or between one adsorbed hydrogen atom and a proton in solution (Volmer-Heyrovsky reaction mechanism). The Tafel slope corresponding to 3D Ti/TiO_2 NT-EG, 56 mV dec^{-1} is larger and suggests a Volmer-Heyrovsky route for this electrode, in which the Volmer reaction between one adsorbed H-atom and a proton in solution is the most-likely the rate-determining step. In this scenario, the amount of adsorbed hydrogen atoms (H_{ads}) plays a key role in the overall reaction, but the overall reaction rate might result from a contribution of both the rates of adsorption and surface reaction. The even smaller Tafel slope corresponding to 3D Ti/TiO_2 NT-W (40 mV dec^{-1}) indicates a relatively fast overall reaction rate, confirming that adsorption of hydrogen may not be the rate-limiting step in our case.

Control of the electrical double layer (EDL) formation inside and outside the nanotubes and maximum utilization of the surface area of 3D Ti/TiO_2 NT electrodes can be used to enhance proton adsorption rates or facilitate reaction between adsorbed hydrogen and hydrogen in solution (Volmer-Heyrovsky reaction mechanism), due to the

high local concentration of protons near the surface. In a previous study, we demonstrated that highly-ordered, cylindrical TiO_2 NT favor EDL formation, and that promotion of electrosorption (i.e., accumulation of ions of opposite charge near the surface) can be controlled and enhanced via tuning NT morphology, i.e. NT diameter, density, and length. [175] Additionally, thinner walls in the case of NT-W compared to those for the NT-EG result in overall lower electrical resistance and better effective utilization of the applied potential for EDL formation and, therefore, higher local concentrations of protons at the electrode surface.

It has been well documented that the Ti metal displays only very limited catalytic activity for HER.[182] Thus, the competitive catalytic activities of the 3D Ti/TiO_2 NT electrodes are mainly contributed by the TiO_2 NT, while the 3D printed Ti template contributed with effectively exposing the active sites of catalyst and also serving as a highly conductive continuous electron transfer network with very good electrical contact with the active surface itself. Notably, the structure and properties of TiO_2 NT can be easily tuned and engineered through simple approaches, for example adjusting anodization parameters and annealing. Given the fact that the TiO_2 NT properties are significantly associated with improved HER reaction rates, the combination of highly tailorable TiO_2 NT active surfaces with easily constructed 3D templates opens a door for a straight-forward method to engineer novel HER catalysts. More importantly, the catalyst-fabrication approach described in this work avoids time- and energy-consuming fabrication processes and highly resistive organic binder for catalyst doping onto electrodes or current collectors.

Electrochemical impedance spectroscopy (EIS) was employed to provide further insight into the electrode/electrolyte interface and the electrochemistry at the electrode

surface. Figure 38 presents the Nyquist plots for the EIS spectra obtained for both, TiO_2 NT-EG and TiO_2-NT-W electrodes, at 500 mV. The inset in Figure 38 depicts the electrical equivalent circuit (EEC) used to analyze the EIS spectra. The EEC consists of ohmic resistance in series with a module, in which the charge transfer resistance (R_{ct}) is in parallel with a constant phase element (CPE). The TiO_2 NT-W exhibits R_{ct} with the value of 9.8 Ω, which is smaller than that of TiO_2 NT-EG with the value of 31.4 Ω. The high electron transfer rate on the 3D Ti/TiO_2 NT-W electrode is particularly noteworthy. It is also obvious from the Nyquist plots that the overall HER rate is related to the R_{ct}, which is further evidence that HER is taking place via the two-step Volmer- Heyrovsky mechanism. The smaller R_{ct} associated with the TiO_2 NT-W electrode further confirms the presence of a low energy barrier during the adsorption and desorption steps.

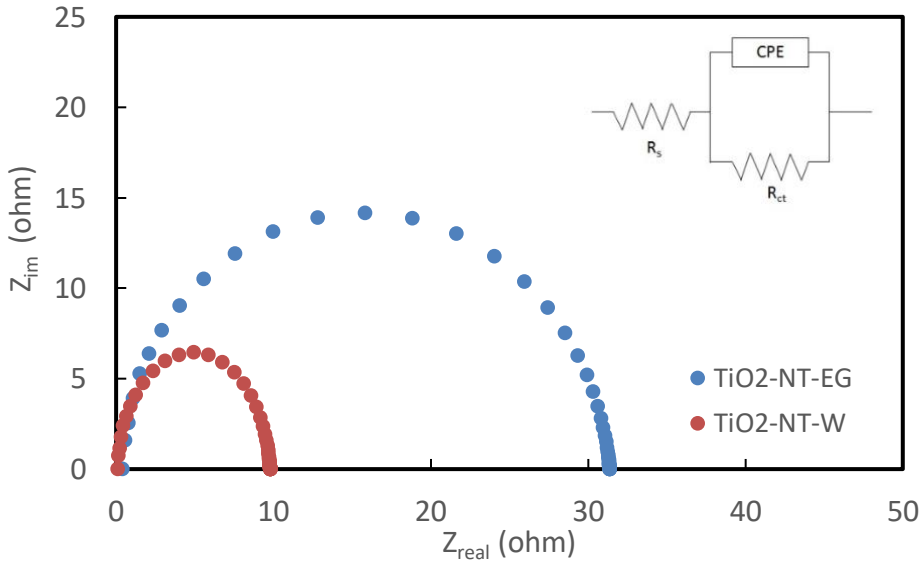

Figure 38 EIS Nyquist plots of 3D Ti/TiO_2-NT-EG and 3D Ti/TiO_2-NT-W. Inset shows the electrical equivalent circuit used to explain the EIS spectra.

The stability and durability of the 3D Ti/TiO_2-NT electrodes was evaluated by a prolonged electrocatalysis test at constant potential in different electrolytes. As shown in Figure 39, the current density of 3D Ti/TiO_2 NT electrode remains almost stable in 1 mol/L

KOH for 10 hours, whereas small degradation is observed in 0.5 mol/L H_2SO_4 during long term operation. For 3D Ti/TiO_2 NT-W, after 10 hours test, the current density increased about 18%, indicating loss of activity of the materials. The disintegration of the TiO_2 NTs and loss of active materials, which may be caused by corrosion in acidic environment, is expected to account for the small but continuous degradation of the catalytic activity of 3D Ti/TiO_2 NT electrode over the operation period.

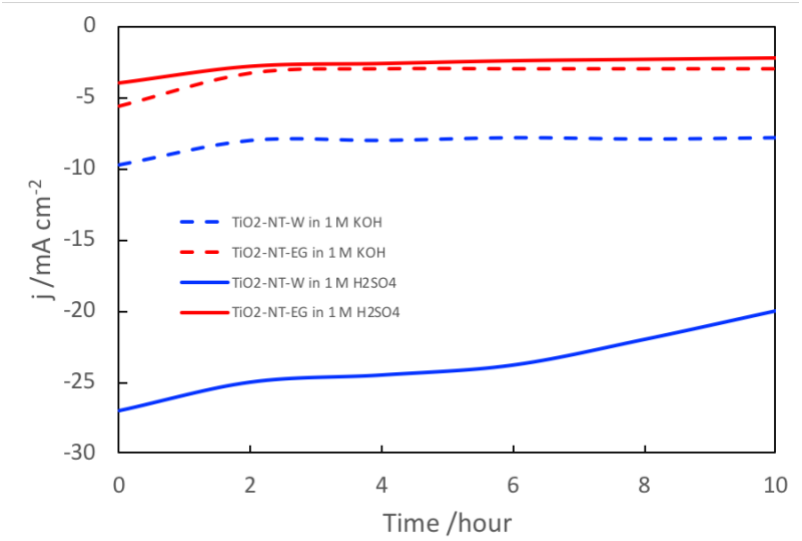

Figure 39 Time-dependent current density curve under applied potential of 150 mV in 0.5 mol/L H_2SO_4 (solid line) and 300 mV in 1 mol/L KOH (dash line).

In closing, the competitive catalytic activity for HER of our 3D Ti/TiO_2 NT electrodes can be ascribed to the following reasons: 1) the hierarchically flow-through 3D structure enables more efficient interaction between the electrode and hydrogen atoms that results in faster two-step reaction mechanism, faster mass transport to reactive sites and effective utilization of catalyst surface; 2) the ohmic-free contact between catalyst (TiO_2 NT) and the current collector (3D Ti substrate) provides a continuous and efficient conducting network of charge and electron transfer while avoiding high-resistance binder

usage and catalyst loss during operation. Finally, a clear advantage of the electrodes introduced in this work is that they are readily scalable for industrial applications, due to their straight-forward fabrication method.

5.5 Conclusions

Summarizing, we developed a novel strategy to fabricate hierarchically flow-through 3D Ti/TiO_2 NT electrodes for HER. The 3D Ti/TiO_2 NT electrodes reported in the present work take advantage of 3D printing and in-situ anodization to achieve a hierarchical and efficient HER electrocatalysis. Most importantly, the preparation of the 3D Ti/TiO_2 NT electrode is facile and readily scalable since the fabrication does not include time- and energy-consuming processes such as complex precursor preparation and high-temperature heat treatments. The large-scale construction of 3D Ti/TiO_2 NT does not require high capital cost and the flow-through feature makes it very appealing for continuous, industrial-scale hydrogen production. This study also provides evidence that the TiO_2 NT on the surface of the 3D Ti templates is the active catalytic surface promoting HER, by a two-step mechanism that contributes to the faster rate of the overall process. The 3D Ti templates contribute to fast HER reaction rates in terms of offering a seamless electron transfer network and large exposed active sites, namely TiO_2 NT. Further improvements in catalytic HER activity and performance of the present electrodes can easily be pursued via simple engineering of the highly ordered and tailorable structure and morphology of TiO_2 NT.

CHAPTER 6 SUMMARY AND CONCLUSIONS

TiO_2 is one of the most investigated materials nowadays. Particularly, TiO_2 NTs have received constant attention due to their high degree of ordering and tailorable morphological structure. The relationship between anodization parameters and TiO_2 NTs morphology and structure was successfully unraveled in the present study. Highly-uniform TiO_2 NTs with three pore sizes (36.8, 41.4, and 44.9 nm) were synthesized by carefully engineering anodization conditions while the TiO_2 NTs' crystalline structure can be altered by annealing as-anodized NTs in air.

The study of the interactive effects of pore diameter, applied potential and ion type on the electrosorption of three alkaline-metal cations (Li^+, Na^+, Cs^+) was carried out by using the highly-ordered TiO_2-NT electrodes as model systems. The proportionality of electrosorption capacity to surface area and applied potential did not hold for all combinations of pore sizes and applied potentials examined in this work, and the behavior of electrosorption capacity was highly dependent on ion type. The highest electrosorption capacities were obtained for a combination of TiO_2-NT electrodes with a pore diameter of 36.8 nm (specific surface area equal to 28.2 m^2/g) and the highest applied potential (-600 mV vs Ag/AgCl). The measured electrosorption capacity trend was $Cs^+ > Na^+ > Li^+$; although this is opposite to the order of ion size, the trend follows the hydrated radius size. This observation supports the hypothesis that electrosorption of fully hydrated ions takes place more effectively in electrical double layers (EDLs) within narrower pores at higher applied potentials. Nanotube electrodes having intermediate and large pore sizes of 41.4 nm and 44.9 nm, respectively, typically have reduced electrosorption capacities that contradict expectations of proportionality to applied potential. This work suggests that tailoring nanoscale electrode properties and voltage conditions to ion type may enable

selective electrosorption. On the other hand, in contrast with classical theory predictions, electrosorption of ions was achieved not solely in response to electrostatic interactions between ions and electrode surface. Selective separation of ionic species bearing the same charge was achieved most likely via desolvation and specific ion-surface interactions triggered by the difference in crystalline structure of the titanium dioxide nanotubes electrodes used in this work. This work experimentally validated predictions on electrosorption behavior that had only been predicted by molecular modeling simulations thus far.

Other important achievement of the present study is the 3D TiO_2 NTs electrode development and application to hydrogen production. In present study, we developed a novel strategy to fabricate hierarchically flow-through 3D Ti/TiO_2 NT electrodes for HER. The 3D Ti/TiO_2 NT electrodes reported here take advantage of 3D printing and *in-situ* anodization to achieve efficient HER electrocatalysis. Most importantly, the preparation of the 3D Ti/TiO_2 NT electrode is facile and readily scalable since the fabrication does not include time- and energy-consuming processes such as complex precursor preparation and high-temperature heat treatments. The large-scale construction of 3D Ti/TiO_2 NT electrode does not require high capital cost and the flow-through feature makes it very appealing for continuous, industrial-scale hydrogen production. This study also provides evidence that the TiO_2 NT on the surface of the 3D Ti templates is the active catalytic surface promoting HER, by a two-step mechanism that contributes to the faster rate of the overall process. The 3D Ti templates contribute to fast HER reaction rates in terms of offering a seamless electron transfer network and large exposed active sites, namely TiO_2 NTs.

The hypothesis guiding the present work was thus proven: control of TiO2 NTs' structure can lead to successful tailoring of these electrodes to electrochemical applications that had not been explored before. All the objectives put forth for this work were met.

CHAPTER 7 FUTURE WORK RECOMMENDATION

As final remarks, while much work has been done and much has been achieved, the potential of TiO_2-NT electrodes is far from being completely explored, especially the 3D Ti/TiO_2 NT electrodes. We would like to recommend some very attractive future work focusing on the following.

Firstly, TiO_2 NTs morphology and crystalline structure effect on the catalytic activity towards hydrogen production is well-worth of a comprehensive study. The TiO_2 NTs anodized at 60 V has been investigated in present study and demonstrated good catalytic activity for HER. However, based on our results, tuning morphological and crystalline structure will significantly influence the electrochemical properties, in terms of conductivity and EDL formation and capacitance. In fact, this investigation will generate avenues to pursue towards electrode optimization for future scale-up.

Secondly, the low-cost and facile fabrication of large scale 3D Ti/TiO_2-NT electrodes represents good motivation for engineers to utilize these materials to real world commercial application. For this purpose, a pilot scale continuous hydrogen production reactor is suggested to be built up, by which the onset potential, long term durability and some other operation parameters can be studied.

Additionally, from a practical point of view, the 3D Ti/TiO_2 NTs electrode has great potential to be used for various electrochemical processes. One is more than happy to predict that ample sustainable technologies, such as bio-electrolysis, photo-electrochemical cells, and super capacitors, can embrace the 3D Ti/TiO_2-NT electrodes in near future.

REFERENCES

[1] X. Wang, Z. Li, J. Shi, Y. Yu, One-dimensional titanium dioxide nanomaterials: nanowires, nanorods, and nanobelts, Chemical reviews, 114 (2014) 9346-9384.
[2] G. Liu, H.G. Yang, J. Pan, Y.Q. Yang, G.Q. Lu, H.-M. Cheng, Titanium dioxide crystals with tailored facets, Chemical reviews, 114 (2014) 9559-9612.
[3] M. Kapilashrami, Y. Zhang, Y.-S. Liu, A. Hagfeldt, J. Guo, Probing the optical property and electronic structure of TiO2 nanomaterials for renewable energy applications, Chemical reviews, 114 (2014) 9662-9707.
[4] F. De Angelis, C. Di Valentin, S. Fantacci, A. Vittadini, A. Selloni, Theoretical studies on anatase and less common TiO2 phases: bulk, surfaces, and nanomaterials, Chemical reviews, 114 (2014) 9708-9753.
[5] M. Dahl, Y. Liu, Y. Yin, Composite titanium dioxide nanomaterials, Chemical reviews, 114 (2014) 9853-9889.
[6] K. Liu, M. Cao, A. Fujishima, L. Jiang, Bio-inspired titanium dioxide materials with special wettability and their applications, Chemical reviews, 114 (2014) 10044-10094.
[7] T. Rajh, N.M. Dimitrijevic, M. Bissonnette, T. Koritarov, V. Konda, Titanium dioxide in the service of the biomedical revolution, Chemical reviews, 114 (2014) 10177-10216.
[8] J. Bai, B. Zhou, Titanium dioxide nanomaterials for sensor applications, Chemical reviews, 114 (2014) 10131-10176.
[9] L. Liu, X. Chen, Titanium dioxide nanomaterials: self-structural modifications, Chemical reviews, 114 (2014) 9890-9918.
[10] U. Diebold, The surface science of titanium dioxide, Surface science reports, 48 (2003) 53-229.
[11] S. Iijima, Helical microtubules of graphitic carbon, nature, 354 (1991) 56.
[12] F. Krumeich, H.-J. Muhr, M. Niederberger, F. Bieri, B. Schnyder, R. Nesper, Morphology and topochemical reactions of novel vanadium oxide nanotubes, Journal of the American Chemical Society, 121 (1999) 8324-8331.
[13] B. Yao, Y.F. Chan, X. Zhang, W. Zhang, Z. Yang, N. Wang, Formation mechanism of TiO 2 nanotubes, Applied physics letters, 82 (2003) 281-283.
[14] M.E. Spahr, P. Stoschitzki‐Bitterli, R. Nesper, O. Haas, P. Novák, Vanadium Oxide Nanotubes. A New Nanostructured Redox‐Active Material for the Electrochemical Insertion of Lithium, Journal of The Electrochemical Society, 146 (1999) 2780-2783.
[15] D.V. Bavykin, J.M. Friedrich, F.C. Walsh, Protonated titanates and TiO2 nanostructured materials: synthesis, properties, and applications, Advanced Materials, 18 (2006) 2807-2824.
[16] X. Chen, S.S. Mao, Titanium dioxide nanomaterials: synthesis, properties, modifications, and applications, Chem. Rev, 107 (2007) 2891-2959.
[17] G.-W. She, X.-H. Zhang, W.-S. Shi, X. Fan, J.C. Chang, C.-S. Lee, S.-T. Lee, C.-H. Liu, Controlled synthesis of oriented single-crystal ZnO nanotube arrays on transparent conductive substrates, Applied physics letters, 92 (2008) 053111.
[18] K. Lee, A. Mazare, P. Schmuki, One-dimensional titanium dioxide nanomaterials: nanotubes, Chemical reviews, 114 (2014) 9385-9454.

[19] S. Kobayashi, N. Hamasaki, M. Suzuki, M. Kimura, H. Shirai, K. Hanabusa, Preparation of helical transition-metal oxide tubes using organogelators as structure-directing agents, Journal of the american chemical society, 124 (2002) 6550-6551.
[20] G. Gundiah, S. Mukhopadhyay, U.G. Tumkurkar, A. Govindaraj, U. Maitra, C. Rao, Hydrogel route to nanotubes of metal oxides and sulfates, Journal of Materials Chemistry, 13 (2003) 2118-2122.
[21] T. Kasuga, M. Hiramatsu, A. Hoson, T. Sekino, K. Niihara, Formation of titanium oxide nanotube, Langmuir, 14 (1998) 3160-3163.
[22] K. Nakane, N. Shimada, T. Ogihara, N. Ogata, S. Yamaguchi, Formation of TiO2 nanotubes by thermal decomposition of poly (vinyl alcohol)-titanium alkoxide hybrid nanofibers, Journal of materials science, 42 (2007) 4031-4035.
[23] V. Zwilling, E. Darque‐Ceretti, A. Boutry‐Forveille, D. David, M.-Y. Perrin, M. Aucouturier, Structure and physicochemistry of anodic oxide films on titanium and TA6V alloy, Surface and Interface Analysis, 27 (1999) 629-637.
[24] V. Zwilling, M. Aucouturier, E. Darque-Ceretti, Anodic oxidation of titanium and TA6V alloy in chromic media. An electrochemical approach, Electrochimica Acta, 45 (1999) 921-929.
[25] P. Hoyer, Formation of a titanium dioxide nanotube array, Langmuir, 12 (1996) 1411-1413.
[26] S.J. Ku, G.C. Jo, C.H. Bak, S.M. Kim, Y.R. Shin, K.H. Kim, S.H. Kwon, J.-B. Kim, Highly ordered freestanding titanium oxide nanotube arrays using Si-containing block copolymer lithography and atomic layer deposition, Nanotechnology, 24 (2013) 085301.
[27] O. Jessensky, F. Müller, U. Gösele, Self-organized formation of hexagonal pore arrays in anodic alumina, Applied physics letters, 72 (1998) 1173-1175.
[28] E. Moyen, L. Santinacci, L. Masson, W. Wulfhekel, M. Hanbücken, A Novel Self‐Ordered Sub‐10 nm Nanopore Template for Nanotechnology, Advanced Materials, 24 (2012) 5094-5098.
[29] O. Nishinaga, T. Kikuchi, S. Natsui, R.O. Suzuki, Rapid fabrication of self-ordered porous alumina with 10-/sub-10-nm-scale nanostructures by selenic acid anodizing, Scientific reports, 3 (2013) 2748.
[30] M. Steinhart, R.B. Wehrspohn, U. Gösele, J.H. Wendorff, Nanotubes by template wetting: a modular assembly system, Angewandte Chemie International Edition, 43 (2004) 1334-1344.
[31] T. Kasuga, M. Hiramatsu, A. Hoson, T. Sekino, K. Niihara, Titania nanotubes prepared by chemical processing, Advanced Materials, 11 (1999) 1307-1311.
[32] X. Sun, Y. Li, Synthesis and characterization of ion‐exchangeable titanate nanotubes, Chemistry-A European Journal, 9 (2003) 2229-2238.
[33] G. Du, Q. Chen, R. Che, Z. Yuan, L.-M. Peng, Preparation and structure analysis of titanium oxide nanotubes, Applied Physics Letters, 79 (2001) 3702-3704.
[34] E. Morgado Jr, M.A. de Abreu, O.R. Pravia, B.A. Marinkovic, P.M. Jardim, F.C. Rizzo, A.S. Araújo, A study on the structure and thermal stability of titanate nanotubes as a function of sodium content, Solid State Sciences, 8 (2006) 888-900.
[35] A. Nakahira, W. Kato, M. Tamai, T. Isshiki, K. Nishio, H. Aritani, Synthesis of nanotube from a layered H2Ti4O9· H2O in a hydrothermal treatment using various titania sources, Journal of Materials Science, 39 (2004) 4239-4245.

[36] J. Yang, Z. Jin, X. Wang, W. Li, J. Zhang, S. Zhang, X. Guo, Z. Zhang, Study on composition, structure and formation process of nanotube Na 2 Ti 2 O 4 (OH) 2, Dalton Transactions, (2003) 3898-3901.
[37] W. Wang, O.K. Varghese, M. Paulose, C.A. Grimes, Q. Wang, E.C. Dickey, A study on the growth and structure of titania nanotubes, Journal of materials research, 19 (2004) 417-422.
[38] K. Nakane, N. Ogata, Photocatalyst Nanofibers Obtained by Calcination of Organic-Inorganic Hybrids, INTECH Open Access Publisher2010.
[39] L.F. Mendes, A.S. Moraes, J.S. Santos, F.L. Leite, F. Trivinho-Strixino, Investigation of roughness and specular quality of commercial aluminum (6061 alloy) for fabrication of nanoporous anodic alumina films, Surface and Coatings Technology, 310 (2017) 199-206.
[40] H.-Y. Hsiao, H.-C. Tsung, W.-T. Tsai, Anodization of AZ91D magnesium alloy in silicate-containing electrolytes, Surface and Coatings Technology, 199 (2005) 127-134.
[41] X. Wu, G. Lu, C. Li, G. Shi, Room-temperature fabrication of highly oriented ZnO nanoneedle arrays by anodization of zinc foil, Nanotechnology, 17 (2006) 4936.
[42] A. Pawlik, M. Jarosz, K. Syrek, G.D. Sulka, Co-delivery of ibuprofen and gentamicin from nanoporous anodic titanium dioxide layers, Colloids and Surfaces B: Biointerfaces, (2017).
[43] J.M. Macak, H. Tsuchiya, L. Taveira, S. Aldabergerova, P. Schmuki, Smooth anodic TiO2 nanotubes, Angewandte Chemie International Edition, 44 (2005) 7463-7465.
[44] J. Park, S. Bauer, K. von der Mark, P. Schmuki, Nanosize and vitality: TiO2 nanotube diameter directs cell fate, Nano letters, 7 (2007) 1686-1691.
[45] M.-Y. Hsu, H.-L. Hsu, J. Leu, TiO2 Nanowires on Anodic TiO2 Nanotube Arrays (TNWs/TNAs): Formation Mechanism and Photocatalytic Performance, Journal of The Electrochemical Society, 159 (2012) H722-H727.
[46] S. Bauer, S. Kleber, P. Schmuki, TiO 2 nanotubes: tailoring the geometry in H 3 PO 4/HF electrolytes, Electrochemistry Communications, 8 (2006) 1321-1325.
[47] K. Yasuda, J.M. Macak, S. Berger, A. Ghicov, P. Schmuki, Mechanistic aspects of the self-organization process for oxide nanotube formation on valve metals, Journal of the electrochemical society, 154 (2007) C472-C478.
[48] K. Yasuda, P. Schmuki, Control of morphology and composition of self-organized zirconium titanate nanotubes formed in (NH 4) 2 SO 4/NH 4 F electrolytes, Electrochimica Acta, 52 (2007) 4053-4061.
[49] J. Macak, H. Hildebrand, U. Marten-Jahns, P. Schmuki, Mechanistic aspects and growth of large diameter self-organized TiO 2 nanotubes, Journal of Electroanalytical Chemistry, 621 (2008) 254-266.
[50] S.P. Albu, A. Ghicov, P. Schmuki, High aspect ratio, self‐ordered iron oxide nanopores formed by anodization of Fe in ethylene glycol/NH4F electrolytes, physica status solidi (RRL)-Rapid Research Letters, 3 (2009) 64-66.
[51] R. Beranek, H. Hildebrand, P. Schmuki, Self-organized porous titanium oxide prepared in H 2 SO 4/HF electrolytes, Electrochemical and solid-state letters, 6 (2003) B12-B14.
[52] K. Zhu, T.B. Vinzant, N.R. Neale, A.J. Frank, Removing structural disorder from oriented TiO2 nanotube arrays: reducing the dimensionality of transport and recombination in dye-sensitized solar cells, Nano Letters, 7 (2007) 3739-3746.

[53] Y.-Y. Song, R. Lynch, D. Kim, P. Roy, P. Schmuki, TiO2 nanotubes: efficient suppression of top etching during anodic growth key to improved high aspect ratio geometries, Electrochemical and Solid-State Letters, 12 (2009) C17-C20.
[54] J.H. Lim, J. Choi, Titanium Oxide Nanowires Originating from Anodically Grown Nanotubes: The Bamboo‐Splitting Model, Small, 3 (2007) 1504-1507.
[55] D. Regonini, C. Bowen, A. Jaroenworaluck, R. Stevens, A review of growth mechanism, structure and crystallinity of anodized TiO 2 nanotubes, Materials Science and Engineering: R: Reports, 74 (2013) 377-406.
[56] R.P. Lynch, A. Ghicov, P. Schmuki, A photo-electrochemical investigation of self-organized TiO2 nanotubes, Journal of The Electrochemical Society, 157 (2010) G76-G84.
[57] J.M. Macák, H. Tsuchiya, A. Ghicov, P. Schmuki, Dye-sensitized anodic TiO 2 nanotubes, Electrochemistry Communications, 7 (2005) 1133-1137.
[58] J.M. Macak, K. Sirotna, P. Schmuki, Self-organized porous titanium oxide prepared in Na 2 SO 4/NaF electrolytes, Electrochimica Acta, 50 (2005) 3679-3684.
[59] P. Roy, D. Kim, K. Lee, E. Spiecker, P. Schmuki, TiO2 nanotubes and their application in dye-sensitized solar cells, Nanoscale, 2 (2010) 45-59.
[60] F. Mohammadpour, M. Moradi, K. Lee, G. Cha, S. So, A. Kahnt, D. Guldi, M. Altomare, P. Schmuki, Enhanced performance of dye-sensitized solar cells based on TiO 2 nanotube membranes using an optimized annealing profile, Chemical Communications, 51 (2015) 1631-1634.
[61] F. Mohammadpour, M. Moradi, G. Cha, S. So, K. Lee, M. Altomare, P. Schmuki, Comparison of Anodic TiO2‐Nanotube Membranes used for Frontside‐Illuminated Dye‐Sensitized Solar Cells, ChemElectroChem, 2 (2015) 204-207.
[62] P. Agarwal, I. Paramasivam, N.K. Shrestha, P. Schmuki, MoO3 in Self‐Organized TiO2 Nanotubes for Enhanced Photocatalytic Activity, Chemistry–An Asian Journal, 5 (2010) 66-69.
[63] Y. Lai, L. Sun, Y. Chen, H. Zhuang, C. Lin, J.W. Chin, Effects of the structure of TiO2 nanotube array on Ti substrate on its photocatalytic activity, Journal of the Electrochemical Society, 153 (2006) D123-D127.
[64] Y.R. Smith, A. Kar, V. Subramanian, Investigation of physicochemical parameters that influence photocatalytic degradation of methyl orange over TiO2 nanotubes, Industrial & Engineering Chemistry Research, 48 (2009) 10268-10276.
[65] H.-F. Zhuang, C.-J. Lin, Y.-K. Lai, L. Sun, J. Li, Some critical structure factors of titanium oxide nanotube array in its photocatalytic activity, Environmental science & technology, 41 (2007) 4735-4740.
[66] Z. Liu, X. Zhang, S. Nishimoto, T. Murakami, A. Fujishima, Efficient photocatalytic degradation of gaseous acetaldehyde by highly ordered TiO2 nanotube arrays, Environmental science & technology, 42 (2008) 8547-8551.
[67] Y. Liu, X. Gan, B. Zhou, B. Xiong, J. Li, C. Dong, J. Bai, W. Cai, Photoelectrocatalytic degradation of tetracycline by highly effective TiO 2 nanopore arrays electrode, Journal of hazardous materials, 171 (2009) 678-683.
[68] P. Roy, T. Dey, K. Lee, D. Kim, B. Fabry, P. Schmuki, Size-selective separation of macromolecules by nanochannel titania membrane with self-cleaning (declogging) ability, Journal of the American Chemical Society, 132 (2010) 7893-7895.

[69] H.-c. Liang, X.-z. Li, Effects of structure of anodic TiO 2 nanotube arrays on photocatalytic activity for the degradation of 2, 3-dichlorophenol in aqueous solution, Journal of Hazardous Materials, 162 (2009) 1415-1422.
[70] A. Tighineanu, T. Ruff, S. Albu, R. Hahn, P. Schmuki, Conductivity of TiO 2 nanotubes: influence of annealing time and temperature, Chemical Physics Letters, 494 (2010) 260-263.
[71] R. Beranek, H. Tsuchiya, T. Sugishima, J. Macak, L. Taveira, S. Fujimoto, H. Kisch, P. Schmuki, Enhancement and limits of the photoelectrochemical response from anodic Ti O 2 nanotubes, Applied Physics Letters, 87 (2005) 243114.
[72] J. Yu, G. Dai, B. Cheng, Effect of crystallization methods on morphology and photocatalytic activity of anodized TiO2 nanotube array films, The Journal of Physical Chemistry C, 114 (2010) 19378-19385.
[73] J. Zhao, X. Wang, T. Sun, L. Li, Crystal phase transition and properties of titanium oxide nanotube arrays prepared by anodization, Journal of Alloys and Compounds, 434 (2007) 792-795.
[74] H.-J. Oh, J.-H. Lee, Y.-J. Kim, S.-J. Suh, J.-H. Lee, C.-S. Chi, Synthesis of effective titania nanotubes for wastewater purification, Applied Catalysis B: Environmental, 84 (2008) 142-147.
[75] R. Mohammadpour, M. Ahadian, N. Taghavinia, A. Dolati, Comparison of various anodization and annealing conditions of titanium dioxide nanotubular film on MB degradation, The European Physical Journal Applied Physics, 47 (2009) 10601.
[76] Y. Xie, Photoelectrochemical application of nanotubular titania photoanode, Electrochimica Acta, 51 (2006) 3399-3406.
[77] E. Logothetis, W. Kaiser, TiO2 film oxygen sensors made by chemical vapour deposition from organometallics, Sensors and Actuators, 4 (1983) 333-340.
[78] S. Navale, Z. Yang, C. Liu, P. Cao, V. Patil, N. Ramgir, R. Mane, F. Stadler, Enhanced acetone sensing properties of titanium dioxide nanoparticles with a sub-ppm detection limit, Sensors and Actuators B: Chemical, 255 (2018) 1701-1710.
[79] N. Muthuchamy, A. Gopalan, K.-P. Lee, Highly selective non-enzymatic electrochemical sensor based on a titanium dioxide nanowire–poly (3-aminophenyl boronic acid)–gold nanoparticle ternary nanocomposite, RSC Advances, 8 (2018) 2138-2147.
[80] T. Sampreeth, M. Al-Maghrabi, B. Bahuleyan, M. Ramesan, Synthesis, characterization, thermal properties, conductivity and sensor application study of polyaniline/cerium-doped titanium dioxide nanocomposites, Journal of Materials Science, 53 (2018) 591-603.
[81] P. Roy, S. Berger, P. Schmuki, TiO2 nanotubes: synthesis and applications, Angewandte Chemie International Edition, 50 (2011) 2904-2939.
[82] S. Berger, J. Kunze, P. Schmuki, D. LeClere, A.T. Valota, P. Skeldon, G.E. Thompson, A lithographic approach to determine volume expansion factors during anodization: Using the example of initiation and growth of TiO2-nanotubes, Electrochimica Acta, 54 (2009) 5942-5948.
[83] H. Masuda, M. Ohya, K. Nishio, H. Asoh, M. Nakao, M. Nohtomi, A. Yokoo, T. Tamamura, Photonic band gap in anodic porous alumina with extremely high aspect ratio formed in phosphoric acid solution, Japanese Journal of Applied Physics, 39 (2000) L1039.

[84] K. Nielsch, R. Wehrspohn, J. Barthel, J. Kirschner, U. Gösele, S. Fischer, H. Kronmüller, Hexagonally ordered 100 nm period nickel nanowire arrays, Applied Physics Letters, 79 (2001) 1360-1362.
[85] O. Khantamat, C.-H. Li, S.-P. Liu, T. Liu, H.J. Lee, O. Zenasni, T.-C. Lee, C. Cai, T.R. Lee, Broadening the photoresponsive activity of anatase titanium dioxide particles via decoration with partial gold shells, Journal of colloid and interface science, 513 (2018) 715-725.
[86] X. Jiang, M. Manawan, T. Feng, R. Qian, T. Zhao, G. Zhou, F. Kong, Q. Wang, S. Dai, J.H. Pan, Anatase and rutile in evonik aeroxide P25: Heterojunctioned or individual nanoparticles?, Catalysis Today, 300 (2018) 12-17.
[87] C.-C. Nguyen, D.T. Nguyen, T.-O. Do, A novel route to synthesize C/Pt/TiO2 phase tunable anatase–Rutile TiO2 for efficient sunlight-driven photocatalytic applications, Applied Catalysis B: Environmental, 226 (2018) 46-52.
[88] A. Mazare, I. Paramasivam, F. Schmidt-Stein, K. Lee, I. Demetrescu, P. Schmuki, Flame annealing effects on self-organized TiO2 nanotubes, Electrochimica Acta, 66 (2012) 12-21.
[89] C. Richter, C.A. Schmuttenmaer, Exciton-like trap states limit electron mobility in TiO2 nanotubes, Nature Nanotechnology, 5 (2010) 769-772.
[90] X. Li, T. Close, S. Pustulka, S. Pedu, Y. Xue, C. Richter, P. Taboada-Serrano, Electrosorption of monovalent alkaline metal ions onto highly ordered mesoporous titanium dioxide nanotube electrodes, Electrochimica Acta, 231 (2017) 632-640.
[91] C. Zhang, D. He, J. Ma, W. Tang, T.D. Waite, Faradaic reactions in capacitive deionization (CDI)-problems and possibilities: A review, Water research, 128 (2018) 314-330.
[92] Z.U. Khan, T. Yan, L. Shi, D. Zhang, Improved Capacitive Deionization by Using 3D Intercalated Graphene Sheet-Sphere Nanocomposite Architectures, Environmental Science: Nano, (2018).
[93] X. Yu, H. Ma, W. Du, L. Qu, C. Li, G. Shi, Robust graphene composite films for multifunctional electrochemical capacitors with an ultrawide range of areal mass loading toward high-rate frequency response and ultrahigh specific capacitance, Energy & Environmental Science, (2018).
[94] Z. Wang, Y. Tan, Y. Yang, X. Zhao, Y. Liu, L. Niu, B. Tichnell, L. Kong, L. Kang, Z. Liu, Pomelo peels-derived porous activated carbon microsheets dual-doped with nitrogen and phosphorus for high performance electrochemical capacitors, Journal of Power Sources, 378 (2018) 499-510.
[95] K. Foo, B. Hameed, A short review of activated carbon assisted electrosorption process: an overview, current stage and future prospects, Journal of hazardous materials, 170 (2009) 552-559.
[96] B. Beden, M.-C. Morin, F. Hahn, C. Lamy, "In situ" analysis by infrared reflectance spectroscopy of the adsorbed species resulting from the electrosorption of ethanol on platinum in acid medium, Journal of electroanalytical chemistry and interfacial electrochemistry, 229 (1987) 353-366.
[97] Y. Sun, W. Zeng, H. Sun, S. Luo, D. Chen, V. Chan, K. Liao, Inorganic/polymer-graphene hybrid gel as versatile electrochemical platform for electrochemical capacitor and biosensor, Carbon, (2018).

[98] P. Liu, T. Yan, L. Shi, H.S. Park, X. Chen, Z. Zhao, D. Zhang, Graphene-based materials for capacitive deionization, Journal of Materials Chemistry A, 5 (2017) 13907-13943.
[99] M. Suss, S. Porada, X. Sun, P. Biesheuvel, J. Yoon, V. Presser, Water desalination via capacitive deionization: what is it and what can we expect from it?, Energy & Environmental Science, (2015).
[100] Y. Liu, C. Nie, X. Liu, X. Xu, Z. Sun, L. Pan, Review on carbon-based composite materials for capacitive deionization, RSC Advances, 5 (2015) 15205-15225.
[101] K. Fic, M. He, E.J. Berg, P. Novák, E. Frackowiak, Comparative operando study of degradation mechanisms in carbon-based electrochemical capacitors with Li2SO4 and LiNO3 electrolytes, Carbon, 120 (2017) 281-293.
[102] P. Przygocki, Q. Abbas, F. Béguin, Capacitance enhancement of hybrid electrochemical capacitor with asymmetric carbon electrodes configuration in neutral aqueous electrolyte, Electrochimica Acta, (2018).
[103] G. Rasines, P. Lavela, C. Macías, M.C. Zafra, J.L. Tirado, J.B. Parra, C.O. Ania, N-doped monolithic carbon aerogel electrodes with optimized features for the electrosorption of ions, Carbon, 83 (2015) 262-274.
[104] G. Rasines, P. Lavela, C. Macías, M. Zafra, J. Tirado, C. Ania, On the use of carbon black loaded nitrogen-doped carbon aerogel for the electrosorption of sodium chloride from saline water, Electrochimica Acta, 170 (2015) 154-163.
[105] K. Li, D. Guo, F. Lin, Y. Wei, W. Liu, Y. Kong, Electrosorption of copper ions by poly (m-phenylenediamine)/reduced graphene oxide synthesized via a one-step in situ redox strategy, Electrochimica Acta, 166 (2015) 47-53.
[106] R. Kalluri, M. Biener, M. Suss, M. Merrill, M. Stadermann, J. Santiago, T. Baumann, J. Biener, A. Striolo, Unraveling the potential and pore-size dependent capacitance of slit-shaped graphitic carbon pores in aqueous electrolytes, Physical Chemistry Chemical Physics, 15 (2013) 2309-2320.
[107] C. Tsouris, R. Mayes, J. Kiggans, K. Sharma, S. Yiacoumi, D. DePaoli, S. Dai, Mesoporous carbon for capacitive deionization of saline water, Environmental science & technology, 45 (2011) 10243-10249.
[108] Z. Chen, H. Zhang, C. Wu, Y. Wang, W. Li, A study of electrosorption selectivity of anions by activated carbon electrodes in capacitive deionization, Desalination, 369 (2015) 46-50.
[109] J.H. Bae, J.-H. Han, T.D. Chung, Electrochemistry at nanoporous interfaces: new opportunity for electrocatalysis, Physical Chemistry Chemical Physics, 14 (2012) 448-463.
[110] A. Walcarius, Mesoporous materials and electrochemistry, Chemical Society Reviews, 42 (2013) 4098-4140.
[111] H. Daiguji, Ion transport in nanofluidic channels, Chemical Society Reviews, 39 (2010) 901-911.
[112] G. Feng, R. Qiao, J. Huang, B.G. Sumpter, V. Meunier, Ion distribution in electrified micropores and its role in the anomalous enhancement of capacitance, ACS nano, 4 (2010) 2382-2390.
[113] S. Porada, R. Zhao, A. Van Der Wal, V. Presser, P. Biesheuvel, Review on the science and technology of water desalination by capacitive deionization, Progress in Materials Science, 58 (2013) 1388-1442.

[114] N. Ghaffour, T.M. Missimer, G.L. Amy, Technical review and evaluation of the economics of water desalination: current and future challenges for better water supply sustainability, Desalination, 309 (2013) 197-207.
[115] R. Zhao, M. Van Soestbergen, H. Rijnaarts, A. Van der Wal, M. Bazant, P. Biesheuvel, Time-dependent ion selectivity in capacitive charging of porous electrodes, Journal of colloid and interface science, 384 (2012) 38-44.
[116] C.J. Gabelich, T.D. Tran, I.M. Suffet, Electrosorption of inorganic salts from aqueous solution using carbon aerogels, Environmental science & technology, 36 (2002) 3010-3019.
[117] T.-Y. Ying, K.-L. Yang, S. Yiacoumi, C. Tsouris, Electrosorption of ions from aqueous solutions by nanostructured carbon aerogel, Journal of colloid and interface science, 250 (2002) 18-27.
[118] B. Kastening, M. Heins, Properties of electrolytes in the micropores of activated carbon, Electrochimica Acta, 50 (2005) 2487-2498.
[119] K.C. Leonard, J.R. Genthe, J.L. Sanfilippo, W.A. Zeltner, M.A. Anderson, Synthesis and characterization of asymmetric electrochemical capacitive deionization materials using nanoporous silicon dioxide and magnesium doped aluminum oxide, Electrochimica Acta, 54 (2009) 5286-5291.
[120] C.-H. Hou, P. Taboada-Serrano, S. Yiacoumi, C. Tsouris, Electrosorption selectivity of ions from mixtures of electrolytes inside nanopores, The Journal of chemical physics, 129 (2008) 224703.
[121] C.-H. Hou, P. Taboada-Serrano, S. Yiacoumi, C. Tsouris, Monte Carlo simulation of electrical double-layer formation from mixtures of electrolytes inside nanopores, The Journal of chemical physics, 128 (2008) 044705.
[122] F. Fornasiero, H.G. Park, J.K. Holt, M. Stadermann, C.P. Grigoropoulos, A. Noy, O. Bakajin, Ion exclusion by sub-2-nm carbon nanotube pores, Proceedings of the National Academy of Sciences, 105 (2008) 17250-17255.
[123] R. Zhao, P. Biesheuvel, A. Van der Wal, Energy consumption and constant current operation in membrane capacitive deionization, Energy & Environmental Science, 5 (2012) 9520-9527.
[124] P. Taboada-Serrano, S. Yiacoumi, C. Tsouris, Behavior of mixtures of symmetric and asymmetric electrolytes near discretely charged planar surfaces: A Monte Carlo study, The Journal of chemical physics, 123 (2005) 054703.
[125] P. Taboada-Serrano, S. Yiacoumi, C. Tsouris, Electrostatic surface interactions in mixtures of symmetric and asymmetric electrolytes: A Monte Carlo study, The Journal of chemical physics, 125 (2006) 054716.
[126] D. Henderson, D. Boda, Insights from theory and simulation on the electrical double layer, Physical Chemistry Chemical Physics, 11 (2009) 3822-3830.
[127] D. Boda, W.R. Fawcett, D. Henderson, S. Sokołowski, Monte Carlo, density functional theory, and Poisson–Boltzmann theory study of the structure of an electrolyte near an electrode, The Journal of chemical physics, 116 (2002) 7170-7176.
[128] G.K. Mor, O.K. Varghese, M. Paulose, K. Shankar, C.A. Grimes, A review on highly ordered, vertically oriented TiO 2 nanotube arrays: fabrication, material properties, and solar energy applications, Solar Energy Materials and Solar Cells, 90 (2006) 2011-2075.
[129] S. Rani, S.C. Roy, M. Paulose, O.K. Varghese, G.K. Mor, S. Kim, S. Yoriya, T.J. LaTempa, C. Grimes, Synthesis and applications of electrochemically self-assembled titania nanotube arrays, Physical Chemistry Chemical Physics, 12 (2010) 2780-2800.

[130] H.E. Prakasam, K. Shankar, M. Paulose, O.K. Varghese, C.A. Grimes, A new benchmark for TiO2 nanotube array growth by anodization, The Journal of Physical Chemistry C, 111 (2007) 7235-7241.
[131] A. Haring, A. Morris, M. Hu, Controlling morphological parameters of anodized titania nanotubes for optimized solar energy applications, Materials, 5 (2012) 1890-1909.
[132] A. Tighineanu, T. Ruff, S. Albu, R. Hahn, P. Schmuki, Conductivity of TiO< sub> 2</sub> nanotubes: Influence of annealing time and temperature, Chemical Physics Letters, 494 (2010) 260-263.
[133] E. Nightingale Jr, Phenomenological theory of ion solvation. Effective radii of hydrated ions, The Journal of Physical Chemistry, 63 (1959) 1381-1387.
[134] C.C. McCrory, S. Jung, J.C. Peters, T.F. Jaramillo, Benchmarking heterogeneous electrocatalysts for the oxygen evolution reaction, Journal of the American Chemical Society, 135 (2013) 16977-16987.
[135] J.D. Benck, Z. Chen, L.Y. Kuritzky, A.J. Forman, T.F. Jaramillo, Amorphous molybdenum sulfide catalysts for electrochemical hydrogen production: insights into the origin of their catalytic activity, Acs Catalysis, 2 (2012) 1916-1923.
[136] J.M. Bockris, S. Srinivasan, Electrode kinetic aspects of electrochemical energy conversion, Journal of Electroanalytical Chemistry (1959), 11 (1966) 350-389.
[137] R. Boggio, A. Carugati, S. Trasatti, Electrochemical surface properties of Co3O4 electrodes, Journal of applied electrochemistry, 17 (1987) 828-840.
[138] M.E. Orazem, B. Tribollet, Electrochemical Impedance Spectroscopy, John Wiley & Sons, Inc., Hoboken, NJ, 2008.
[139] G. Brug, A. Van Den Eeden, M. Sluyters-Rehbach, J. Sluyters, The analysis of electrode impedances complicated by the presence of a constant phase element, Journal of electroanalytical chemistry and interfacial electrochemistry, 176 (1984) 275-295.
[140] E.M. Ney, C.-H. Hou, P. Taboada-Serrano, Calculation of Electrical Double Layer Potential Profiles in Nanopores from Grand Canonical Monte Carlo Simulations, Journal of Chemical & Engineering Data, (2018).
[141] G. Blanchard, M. Maunaye, G. Martin, Removal of heavy metals from waters by means of natural zeolites, Water Research, 18 (1984) 1501-1507.
[142] M. Wang, L. Chen, L. Sun, Recent progress in electrochemical hydrogen production with earth-abundant metal complexes as catalysts, Energy & Environmental Science, 5 (2012) 6763-6778.
[143] J.A. Turner, Sustainable hydrogen production, Science, 305 (2004) 972-974.
[144] S. Akhmal Saadon, P. Sathishkumar, A.R. Mohd Yusoff, M.D. Hakim Wirzal, M.T. Rahmalan, H. Nur, Photocatalytic Activity and Reusability of ZnO Layer Synthesised by Electrolysis, Hydrogen Peroxide and Heat Treatment, Environmental technology, (2015) 1-21.
[145] X. Yu, M.S. Prévot, N. Guijarro, K. Sivula, Self-assembled 2D WSe2 thin films for photoelectrochemical hydrogen production, Nature communications, 6 (2015).
[146] L.-C. Pop, L. Sygellou, V. Dracopoulos, K.S. Andrikopoulos, S. Sfaelou, P. Lianos, One-step electrodeposition of CdSe on nanoparticulate titania films and their use as sensitized photoanodes for photoelectrochemical hydrogen production, Catalysis Today, 252 (2015) 157-161.

[147] M.Y. Lin, L.W. Hourng, Effects of magnetic field and pulse potential on hydrogen production via water electrolysis, International Journal of Energy Research, 38 (2014) 106-116.
[148] M.G. Walter, E.L. Warren, J.R. McKone, S.W. Boettcher, Q. Mi, E.A. Santori, N.S. Lewis, Solar water splitting cells, Chemical reviews, 110 (2010) 6446-6473.
[149] R. Subbaraman, D. Tripkovic, D. Strmcnik, K.-C. Chang, M. Uchimura, A.P. Paulikas, V. Stamenkovic, N.M. Markovic, Enhancing hydrogen evolution activity in water splitting by tailoring Li+-Ni (OH) 2-Pt interfaces, Science, 334 (2011) 1256-1260.
[150] B. Hinnemann, P.G. Moses, J. Bonde, K.P. Jørgensen, J.H. Nielsen, S. Horch, I. Chorkendorff, J.K. Nørskov, Biomimetic hydrogen evolution: MoS2 nanoparticles as catalyst for hydrogen evolution, Journal of the American Chemical Society, 127 (2005) 5308-5309.
[151] T.F. Jaramillo, K.P. Jørgensen, J. Bonde, J.H. Nielsen, S. Horch, I. Chorkendorff, Identification of active edge sites for electrochemical H2 evolution from MoS2 nanocatalysts, science, 317 (2007) 100-102.
[152] P. Xiao, M.A. Sk, L. Thia, X. Ge, R.J. Lim, J.-Y. Wang, K.H. Lim, X. Wang, Molybdenum phosphide as an efficient electrocatalyst for the hydrogen evolution reaction, Energy & Environmental Science, 7 (2014) 2624-2629.
[153] Z. Chen, D. Cummins, B.N. Reinecke, E. Clark, M.K. Sunkara, T.F. Jaramillo, Core–shell MoO3–MoS2 nanowires for hydrogen evolution: A functional design for electrocatalytic materials, Nano letters, 11 (2011) 4168-4175.
[154] A. Fujishima, Electrochemical photolysis of water at a semiconductor electrode, nature, 238 (1972) 37-38.
[155] L. Li, J. Yan, T. Wang, Z.-J. Zhao, J. Zhang, J. Gong, N. Guan, Sub-10 nm rutile titanium dioxide nanoparticles for efficient visible-light-driven photocatalytic hydrogen production, Nature communications, 6 (2015).
[156] F. Cai, Y. Tang, H. Shen, C. Wang, A. Ren, L. Xiao, W. Gu, W. Shi, Graphene oxide-assisted synthesis and photocatalytic hydrogen production of mix-phase titanium dioxide (TiO 2) nanosheets, CrystEngComm, 17 (2015) 1086-1091.
[157] M. Karnahl, E. Mejía, N. Rockstroh, S. Tschierlei, S.P. Luo, K. Grabow, A. Kruth, V. Brüser, H. Junge, S. Lochbrunner, Photocatalytic Hydrogen Production with Copper Photosensitizer–Titanium Dioxide Composites, ChemCatChem, 6 (2014) 82-86.
[158] X. Liu, Z. Liu, J. Lu, X. Wu, W. Chu, Silver sulfide nanoparticles sensitized titanium dioxide nanotube arrays synthesized by in situ sulfurization for photocatalytic hydrogen production, Journal of colloid and interface science, 413 (2014) 17-23.
[159] Z. Yan, H. Wu, A. Han, X. Yu, P. Du, Noble metal-free cobalt oxide (CoO x) nanoparticles loaded on titanium dioxide/cadmium sulfide composite for enhanced photocatalytic hydrogen production from water, International Journal of Hydrogen Energy, 39 (2014) 13353-13360.
[160] Z. Yan, X. Yu, Y. Zhang, H. Jia, Z. Sun, P. Du, Enhanced visible light-driven hydrogen production from water by a noble-metal-free system containing organic dye-sensitized titanium dioxide loaded with nickel hydroxide as the cocatalyst, Applied Catalysis B: Environmental, 160 (2014) 173-178.
[161] L. Sun, J. Li, C. Wang, S. Li, H. Chen, C. Lin, An electrochemical strategy of doping Fe 3+ into TiO 2 nanotube array films for enhancement in photocatalytic activity, Solar Energy Materials and Solar Cells, 93 (2009) 1875-1880.

[162] Y. Xie, S.H. Heo, Y.N. Kim, S.H. Yoo, S.O. Cho, Synthesis and visible-light-induced catalytic activity of Ag2S-coupled TiO2 nanoparticles and nanowires, Nanotechnology, 21 (2009) 015703.
[163] K. Nagasuna, T. Akita, M. Fujishima, H. Tada, Photodeposition of Ag2S quantum dots and application to photoelectrochemical cells for hydrogen production under simulated sunlight, Langmuir, 27 (2011) 7294-7300.
[164] R.-A. Doong, T.-C. Hsieh, C.-P. Huang, Photoassisted reduction of metal ions and organic dye by titanium dioxide nanoparticles in aqueous solution under anoxic conditions, Science of the total environment, 408 (2010) 3334-3341.
[165] K. Xie, L. Sun, C. Wang, Y. Lai, M. Wang, H. Chen, C. Lin, Photoelectrocatalytic properties of Ag nanoparticles loaded TiO 2 nanotube arrays prepared by pulse current deposition, Electrochimica Acta, 55 (2010) 7211-7218.
[166] X. Feng, J.D. Sloppy, T.J. LaTempa, M. Paulose, S. Komarneni, N. Bao, C.A. Grimes, Synthesis and deposition of ultrafine Pt nanoparticles within high aspect ratio TiO 2 nanotube arrays: application to the photocatalytic reduction of carbon dioxide, Journal of Materials Chemistry, 21 (2011) 13429-13433.
[167] Y. Yin, Z. Jin, F. Hou, Enhanced solar water-splitting efficiency using core/sheath heterostructure CdS/TiO2 nanotube arrays, Nanotechnology, 18 (2007) 495608.
[168] C. Yang, Z. Wang, T. Lin, H. Yin, X. Lü, D. Wan, T. Xu, C. Zheng, J. Lin, F. Huang, Core-shell nanostructured “black” rutile titania as excellent catalyst for hydrogen production enhanced by sulfur doping, Journal of the American Chemical Society, 135 (2013) 17831-17838.
[169] L. Huang, X. Wang, J. Yang, G. Liu, J. Han, C. Li, Dual cocatalysts loaded type I CdS/ZnS core/shell nanocrystals as effective and stable photocatalysts for H2 evolution, The Journal of Physical Chemistry C, 117 (2013) 11584-11591.
[170] H.S. Kim, D. Kim, B.S. Kwak, G.B. Han, M.-H. Um, M. Kang, Synthesis of magnetically separable core@ shell structured NiFe 2 O 4@ TiO 2 nanomaterial and its use for photocatalytic hydrogen production by methanol/water splitting, Chemical Engineering Journal, 243 (2014) 272-279.
[171] Z. Xu, M. Yin, J. Sun, G. Ding, L. Lu, P. Chang, X. Chen, D. Li, 3D periodic multiscale TiO2 architecture: a platform decorated with graphene quantum dots for enhanced photoelectrochemical water splitting, Nanotechnology, 27 (2016) 115401.
[172] H. Li, H. Yu, L. Sun, J. Zhai, X. Han, A self-assembled 3D Pt/TiO 2 architecture for high-performance photocatalytic hydrogen production, Nanoscale, 7 (2015) 1610-1615.
[173] Z. Bi, M.P. Paranthaman, P.A. Menchhofer, R.R. Dehoff, C.A. Bridges, M. Chi, B. Guo, X.-G. Sun, S. Dai, Self-organized amorphous TiO 2 nanotube arrays on porous Ti foam for rechargeable lithium and sodium ion batteries, Journal of Power Sources, 222 (2013) 461-466.
[174] P. Heinl, C. Körner, R.F. Singer, Selective electron beam melting of cellular titanium: mechanical properties, Advanced Engineering Materials, 10 (2008) 882-888.
[175] X. Li, T. Close, S. Pustulka, S. Pedu, Y. Xue, C. Richter, P. Taboada-Serrano, Electrosorption of monovalent alkaline metal ions onto highly ordered mesoporous titanium dioxide nanotube electrodes, Electrochimica Acta, (2017).
[176] C. Richter, E. Panaitescu, R. Willey, L. Menon, Titania nanotubes prepared by anodization in fluorine-free acids, Journal of materials research, 22 (2007) 1624-1631.

[177] Y. Tan, H. Wang, P. Liu, C. Cheng, F. Zhu, A. Hirata, M. Chen, 3D Nanoporous Metal Phosphides toward High‐Efficiency Electrochemical Hydrogen Production, Advanced Materials, (2016).
[178] M.-R. Gao, M.K. Chan, Y. Sun, Edge-terminated molybdenum disulfide with a 9.4-A interlayer spacing for electrochemical hydrogen production, Nature communications, 6 (2015).
[179] F.X. Ma, H.B. Wu, B.Y. Xia, C.Y. Xu, X.W.D. Lou, Hierarchical β‐Mo2C Nanotubes Organized by Ultrathin Nanosheets as a Highly Efficient Electrocatalyst for Hydrogen Production, Angewandte Chemie International Edition, 54 (2015) 15395-15399.
[180] I. Hod, P. Deria, W. Bury, J.E. Mondloch, C.-W. Kung, M. So, M.D. Sampson, A.W. Peters, C.P. Kubiak, O.K. Farha, A porous proton-relaying metal-organic framework material that accelerates electrochemical hydrogen evolution, Nature communications, 6 (2015).
[181] J. Thomas, Kinetics of electrolytic hydrogen evolution and the adsorption of hydrogen by metals, Transactions of the Faraday Society, 57 (1961) 1603-1611.
[182] N. Thomas, K. Nobe, Kinetics of the hydrogen evolution reaction on titanium, Journal of the Electrochemical Society, 117 (1970) 622-626.